THESIS FOR DEGREE OF DOCTOR OF PHYSICS

Complex Phase Behavior in Thermoelectric $Mg_2Si_{1-x}Sn_x$ Alloys and Development of Transient Plane Source Method for Structural Characterization

Advanced structural characterization of complex materials

ANDREY SIZOV

Department of Chemistry and Chemical Engineering

Chalmers University of Technology

Gothenburg, Sweden 2023

Complex Phase Behavior in Thermoelectric $Mg_2Si_{1-x}Sn_x$ Alloys and Development of Transient Plane Source Method for Structural Characterization

Complex Phase Behavior in Thermoelectric $Mg_2Si_{1-x}Sn_x$ Alloys and Development of Transient Plane Source Method for Structural Characterization
Advanced structural characterization of complex materials
ANDREY SIZOV

ISBN 978-91-7905-921-7

Doktorsavhandlingar vid Chalmers tekniska högskola
Ny serie nr 5387
ISSN 0346-718X

Department of Chemistry and Chemical Engineering
Chalmers University of Technology
SE-412 96 Gothenburg
Sweden
Telephone +46 (0)31-772 1000

Cover:
[A visual representation of the anti-fluorite crystal structure of magnesium silicide-stannide alloys (yellow atoms – Mg, purple atoms – Si or Sn), of Rietveld refinement fit to the XRD data obtained for $Mg_2[(Si_{0.6}Sn_{0.4})_{0.975}]Bi_{0.025}$ treated for 640 min at 720 °C (reflection (111)), showing its multiphase nature, and of a hot disc probe together with the Hot Disk thermal constants analyser.]

Printed by:
Chalmers digitaltryck
Gothenburg, Sweden 2023

Complex Phase Behavior in Thermoelectric $Mg_2Si_{1-x}Sn_x$ Alloys and Development of Transient Plane Source Method for Structural Characterization

ANDREY SIZOV
Department of Chemistry and Chemical Engineering
Chalmers University of Technology, Gothenburg, 2023

Abstract

The thermoelectric effect was discovered nearly 200 years ago, but it started to be utilized for waste heat recovery only fairly recently. From an economical point of view, such applications requires a cheap and efficient material, which is able to convert heat energy into electricity. Magnesium silicide-stannide alloys, also being environmentally friendly and stable at medium temperatures, have a further potential in increasing thermoelectric efficiency by utilizing microstructuring, which has not been much applied to this system. The approach is aimed on reducing the lattice thermal conductivity, while keeping electron transport almost unaffected. In the current work it is suggested to manipulate the microstructure of $Mg_2Si_{1-x}Sn_x$ alloys via formation of endotaxial phases utilizing phase separation. Compositions as well as arrangements of the endotaxial phases are controlled via the heat treatment protocols, which vary mostly depending on the position of the binodal curve, the ratio of Si and Sn in $Mg_2Si_{1-x}Sn_x$ and cooling rate.

Due to the discrepancy in the available quasi-binary phase diagrams Mg_2Si-Mg_2Sn below the solidus, one focus of the current study was held on the estimation of the binodal curve position. For this, Si-rich $Mg_2Si_{1-x}Sn_x$ alloys of different compositions were treated at different temperatures and their structure was investigated utilizing X-ray diffraction. The study showed an agreement of the results with one of the theoretically calculated binodal curves in the Si-rich region. However, the compositions of the Sn-rich phases did not fit with this or any other known models. Moreover, Sn-rich phases treated at higher temperatures contained less Si, whereas the solubility limit of Si in the Sn-rich phase was expected to grow with temperature, which can be a result of pinning effect provided by particle/grain boundaries.

The acquired approximate position of the binodal curve in the Si-rich region allows one to control the phase separation process, and hence the microstructure. Thus, another focus of the thesis was put on creating the finest and most promising microstructure for thermoelectric materials, *i.e.* alternating lamellae-type endotaxial phases, which can, in principle, be achieved during spinodal decomposition. Such a microstructure was found during the experiments of the current work. It is shown that when a compound enters the miscibility gap at temperatures that are too low for migration of the atoms over long distances, it rapidly decomposes forming lamellae with similar compositions. Alternatively, if a compound enters the miscibility gap at higher temperatures, higher cooling rates affect the phase separation similarly.

In addition, it is suggested to utilize the Transient plane source technique in quality control and advanced thermal conductivity characterization of complex isotropic and anisotropic materials. Hence, the thesis also includes the recent development of the so-called Structural probe technique, which makes it possible to convert the temperature vs. time function to the unique thermal conductivity vs. probing depth. Since the thermal conductivity is sensitive to the structural constitution of a material, such a function allows one to assess the microstructure variations with depth. The technique was successfully tested on homogeneous and inhomogeneous materials, as well as on materials with macroscopic defects.

Keywords: magnesium silicide-stannide alloys, structural characterization, complex behavior, multiphase structure, X-ray diffraction, Rietveld refinement, thermoelectric properties, spark plasma sintering, advance measurements of thermal properties, Transient Plane Source method, thermal conductivity vs. probing depth, isotropic and anisotropic materials, quality control, inhomogeneity tests, defects detection.

List of Publications

I. Thermal Conductivity Versus Depth Profiling of Inhomogeneous Materials Using the Hot Disc Technique
A. Sizov, D. Cederkrantz, L. Salmi, A. Rosen, L. Jacobson, S. E. Gustafsson, and M. Gustavsson, Rev. Sci. Instrum. 87, 074901 (2016), https://doi.org/10.1063/1.4954972

II. Influence of phase separation and spinodal decomposition on microstructure of $Mg_2Si_{1-x}Sn_x$ alloys
A. Sizov, H. Reardon, B.B. Iversen, P. Erhart, A.E.C. Palmqvist
Cryst. Growth Des. 2019, 19 (9), 4927, https://doi.org/10.1021/acs.cgd.9b00013

III. Effect of thermal treatment on the composition, microstructure and thermoelectric properties of magnesium silicide-stannide
A. Sizov, A.E.C. Palmqvist
Manuscript

IV. Thermal conductivity vs depth profiling using the hot disk technique–Analysis of anisotropic, inhomogeneous structures
A. Sizov, B. Mihiretie, Y. Ma, S.E. Gustafsson, and M. Gustavsson
Rev. Sci. instrum. 94, 074902 (2023), https://doi.org/10.1063/5.0145902

Contribution Report to the Listed Publications

I. Planning and performing the experimental work, creating mathematical model and analyzing the data, writing the manuscript together with M. Gustavsson.

II. Planning and performing the experimental work, characterization and analysis of the acquired data with help of H. Reardon, writing the first manuscript.

III. Planning and performing the experimental work, characterization and analysis of the acquired data, writing the first manuscript.

IV. Planning and performing the experimental work, creating mathematical model and analyzing the data, writing the manuscript together with M. Gustavsson.

Table of content

Chapter 1

Introduction

This Ph.D. project was started when the green agenda had become stronger than ever. In 1987 the United Nations World Commission on Environment and Development released the report Our Common Future, where the most widely recognized definitions of sustainable development were formulated [1]. The most recent work of the United Nations General Assembly towards a sustainable future resulted in 17 sustainable development goals, one of which concerned energy. A green unipolar world was the most promoted and wished-for scenario.

However, as time went by, we became witnesses of drastic and most likely irreversible changes of our world. The broken global chains of raw materials, devices, fuels, and technologies now force us to seek for alternative and independent self-sufficient solutions to the current challenges. The background report 10 to the Commission on the Future of Sweden in 2013 [2] distinguished possible scenarios of the world's future and Sweden's strategies until 2050. "…a multi-polar world order with growing tensions and securitization of commodities…" [3] is one of the expected scenarios, which Sweden is preparing for. This scenario implies continued global heavy usage of fossil fuels, which could lead to excessively polluting production systems and to uncontrolled global warming. Nevertheless, the topic of the thesis is still relevant, *i.e.* the thermoelectric technology could still help to save precious energy and reduce harmful impact on the

environment. Thermoelectric conversion of waste heat to electricity is of interest as long as combustion of fuels constitutes a part of our energy system.

In addition, thermoelectric devices are highly valuable for the aerospace industry as a reliable source of electricity in deep space, far from the Sun. The NASA research spaceships "Voyager" 1 and 2 were able to leave the Solar System, collect data and transfer it to the Earth purely due to power provided by thermoelectric materials – one of them still transmitting data, almost half a century after launch. In this application, the temperature gradient, which the energy conversion device requires for operation, is built between heating decaying plutonium and a nearly absolute zero temperature of space (cosmic background radiation) [4].

The conversion of fuels into useful energy mainly occurs via combustion, which, in turn, is accompanied by generation of heat. Heat energy, barely utilized as a resource, mainly tends to dissipate into its surroundings, and irreversibly. So, for instance, this occurs in an engine of an ordinary car or of a modern aircraft, and in our kitchen oven or metallurgical furnaces or kilns. To make some use of the derived heat, which is not utilized for other purposes, we may employ the thermoelectric effect, discovered in the beginning of 19th century. This effect makes it possible to produce electricity by connecting a series of alternating N- and P-type semiconducting materials placed in a temperature gradient. This occurs since N-type semiconductors harbor an excess of negative charges (electrons), which are forced by heat gradient to the cold side, while P-type semiconductors have excess of positive charges (holes), which are also forced towards the cold side so that the electrons move in the opposite direction. To improve the efficiency of thermoelectric conversion, new materials are needed. Ideally, a thermoelectric material should conduct electricity like a crystal, but conduct heat like a glass. It is challenging to realize the combination of these properties in one single material, and a combination of strategies have accordingly been developed. Microstructuring has been found to give thermoelectric materials lower thermal conductivity without losing thermoelectric power. Microstructuring can be achieved using metallurgical processing including guidance from materials phase diagrams and by manipulating the microstructure by temperature protocols, or via other relevant tools in order to obtain a composition and morphology of a novel material that enhances thermoelectric properties. Continuing the work done by scientists all over the world, the current thesis elucidates ways to controllably microstructure the promising thermoelectric material magnesium silicide-stannide, via judiciously designed heat treatment protocols.

The later part of the thesis deals with the need for measuring thermal conductivity to characterize materials properties. A rising demand for the heat management as well as quality control of complex modern materials/devices drive scientists to invent new measurement approaches. For instance, a proper anisotropic characterization of batteries utilized for smartphones, computers, cars, etc., in recent years, allowed for reduction of the risk of degradation and self-ignition [5, 6]. Moreover, waste heat recuperation is one of the hottest topics in our days, where thermal conductivity plays an important role. Last, but not least, thermal conductivity, indeed, is also used to evaluate the performance of thermoelectric materials. The main focus here has, however, been to utilize thermal conductivity as a probe for detecting structural inhomogeneities and defects in isotropic and anisotropic materials.

1.1 Goals and motivation

Good material candidates for large scale use in thermoelectric devices should ideally be cheap, non-toxic, stable, and effectively convert heat gradients into electricity. Magnesium silicide-stannide alloys fulfill several of these aspects. Moreover, they have a potential in further improving the thermoelectric efficiency. The highest reported thermoelectric performance in the magnesium silicide-stannide group was achieved in $Mg_2Si_{0.55}Sn_{0.4}Ge_{0.05}$ doped with Bi and Sb [7]. This is due to the optimized charge carrier concentration via doping and decreased thermal conductivity, which is inherent in a highly distorted crystal lattice of solid solutions. However, this is not the complete list of actions, which could be done to the system. For instance, further enhancement of the thermoelectric performance can be realized with nanostructured morphology, as demonstrated in tellurides [8-10]. Since the quasi-binary system Mg_2Si-Mg_2Sn possesses a miscibility gap in the phase diagram [11-15], it allows for employment of phase separation to form a microstructure of interest. The phase separation can be controlled via heat treatment protocols, a design of which requires a reliable phase diagram, which would in turn predict thermodynamically stable phases [16].

The quasi-binary phase diagram of Mg_2Si-Mg_2Sn has been studied well in the vicinity of solidus and liquidus regions, although a lack of experimental data in the solid-state region has created much speculation regarding the shape of a miscibility gap. For example, Kozlov et al. [11] calculated the phase diagram using a CALPHAD model, the parameters for which were obtained in a few experiments by Differential Scanning Calorimetry (DSC). This model contradicted the phase diagram earlier drawn by Jung et al. [12] showing much lower solubility limit of Si in the Mg_2Sn lattice, which totally

changed the shape of the miscibility gap. Later, Viennois et al. [14] presented modified parameters of the Kozlov's model, which resulted in a much higher solubility of Si in the Sn-rich phase, but still not as high as predicted by Jung et al. [12]. Due to such a high discrepancy in the available research data, the first step in this thesis was to figure out what the correct phase diagram looks like.

The next step was to gain control of the microstructure of magnesium silicide-stannide using the phase diagram. The desired morphology for the thermoelectric material would be alternating endotaxial phases or inclusions, which create a large density of interphases, in which the low frequency phonons can be scattered more preferentially than high frequency electrons. Thus, the lattice thermal conductivity would be significantly reduced, while the thermoelectric power should stay almost unaffected. Such fine microstructure can be formed, e.g. through spinodal decomposition or phase separation via nucleation and growth in solid state, which in turn could be controlled via certain heat treatment protocols [17-19]. The influence of these protocols on the composition and morphology of $Mg_2Si_{1-x}Sn_x$ should be investigated in order to learn how to achieve the best performing microstructure.

When manufacturing a material, including thermoelectrics, via compaction of powders at high temperatures, the presence of a miscibility gap (which also concerns spinodal structures) in the system under sintering increases the risk of inhomogeneity in the final compact. One reason for this is the temperature distribution in the pellet during the heat treatment, as previously observed by our group [20]. Due to a lack of techniques to assess structural inhomogeneity in a non-destructive manner, a new method was needed and therefore developed in the context of this thesis. This novel method, which is based on the Transient Plane Source technique [21, 22], provides a function of thermal conductivity versus probing depth, which is used to evaluate a change of the material microstructure. For a material, which is homogeneous, the recorded thermal conductivity vs. depth results in a constant thermal conductivity function with a zero slope. In case the material displays an inhomogeneous thermal conductivity vs. depth, an approximate variation can be recorded with this technique. Since the connection between thermal conductivity and microstructure/constitution is typically quite strong, although seldom known à priori, it is here believed that this technique may be used to assist in detecting microstructural variations with depth, utilizing the thermal conductivity variation with depth as an indirect quality indicator – or indicator of structural inhomogeneity – of the material in question. In addition, the new method

offers an ability to detect defects (local inhomogeneities) of isotropic and anisotropic structures.

Chapter 2

Theoretical background

2.1 Thermoelectricity

The thermoelectric effect consists in reversible direct conversion of heat into electricity and wise versa. Thermoelectricity includes three effects, which were independently identified by T. J. Seebeck [23-25], J. C. Peltier [26] and W. Thomson [27] and were named after them. Thomson was able to connect these effects, concluding that they all constitute different manifestations of one and the same property characterized by the Seebeck coefficient [28]. The thermoelectric effect is commonly used in waste heat recovery for additional energy utilization or as a main source of electricity in deep space, or as a heat pump with an ability to switch between cooling/heating modes. The primary advantages of this effect, when implemented in a device, are an absence of moving parts, long operational life-time, no circulation of fluid or gas required, flexibility, and small size. A crucial disadvantage however is a comparatively poor efficiency. A principal of thermoelectricity can be demonstrated with an example of a simple thermoelectric device (Figure 1).

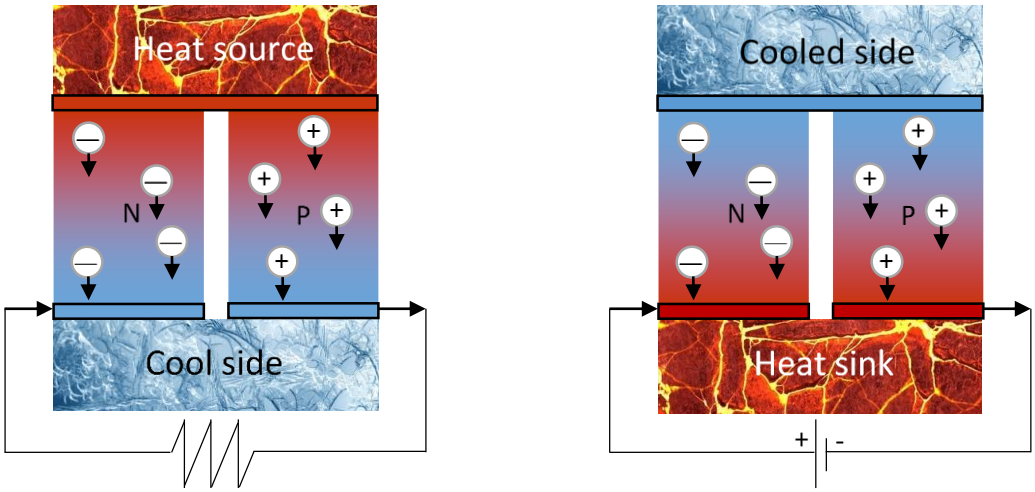

a) b)

Figure 1. Schematic illustration of a thermoelectric device: a) power generator b) heat pump.

An electric current flows when placing two materials, one with a negative Seebeck coefficient, another with a positive one, thermally in parallel and electrically in series (Figure 1a). The current occurs due to the temperature gradient, which forces charge carriers of both materials to move from the hot side to the cool one. The charge carriers can be electrons, as in N-type semiconductors, or holes, *i.e.* empty energetic levels present due to a lack of electrons, as in P-type semiconductors. Since positive charge carriers in a P-type semiconductor move towards the cold side, electrons travel in the opposite direction, thus, closing the electrical circuit.

An opposite phenomenon occurs, when an external potential is applied (Figure 1b). In this case, the charge carriers transfer heat from one side to another. Depending on the current direction, the device is thus able to cool or to heat.

2.2 Thermoelectric properties and ways to measure them

The conversion efficiency of a thermoelectric device can be obtained from the Carnot efficiency and dimensionless figure of merit zT, which, in turn, represents a thermoelectric performance [29]:

$$\eta = \frac{T_h - T_c}{T_h} \cdot \frac{\sqrt{1 + zT_M} - 1}{\sqrt{1 + zT_M} + {T_c}/{T_h}} \qquad \text{(Eq.1)}$$

where T_h is the hottest and T_c is the coldest point of a device, T_M is an average temperature between these two points, and zT is calculated from three thermoelectric properties:

$$zT = \frac{S^2\sigma}{\lambda}T \qquad \text{(Eq.2)}$$

where S is the Seebeck coefficient, σ is the electrical conductivity, and λ is the thermal conductivity. According to Equations 1 and 2, the Carnot factor can be influenced only by creating a greater temperature difference between material sides, whereas the zT factor can be increased by enhancing the thermoelectric power ($S^2\sigma$) and by reducing the thermal conductivity.

2.2.1 Seebeck coefficient

The Seebeck effect, present in all conductive materials, is described in terms of the relative Seebeck coefficient (Seebeck coefficient further), which is an increment of the relative Seebeck emf over a small temperature difference [30]. Utilizing parabolic band and energy-independent scattering approximations, the Seebeck coefficient depends on the current effective mass (m^*), charge carriers concentration (n) and temperature [31]:

$$S = \frac{8\pi^2 k_B^2}{3eh^2} m^* T \left(\frac{\pi}{3n}\right)^{2/3} \qquad \text{(Eq.3)}$$

where k_B is the Boltzmann constant, e is the elemental charge and h is the Planck's constant. There are a couple of techniques, which can measure the Seebeck coefficient, *e.g.* differential light-pipe system [32] or small ΔT differential method [33]. The main principal of Seebeck coefficient measurements will be demonstrated with an example of the last method, the schematic setup of which is illustrated in Figure 2.

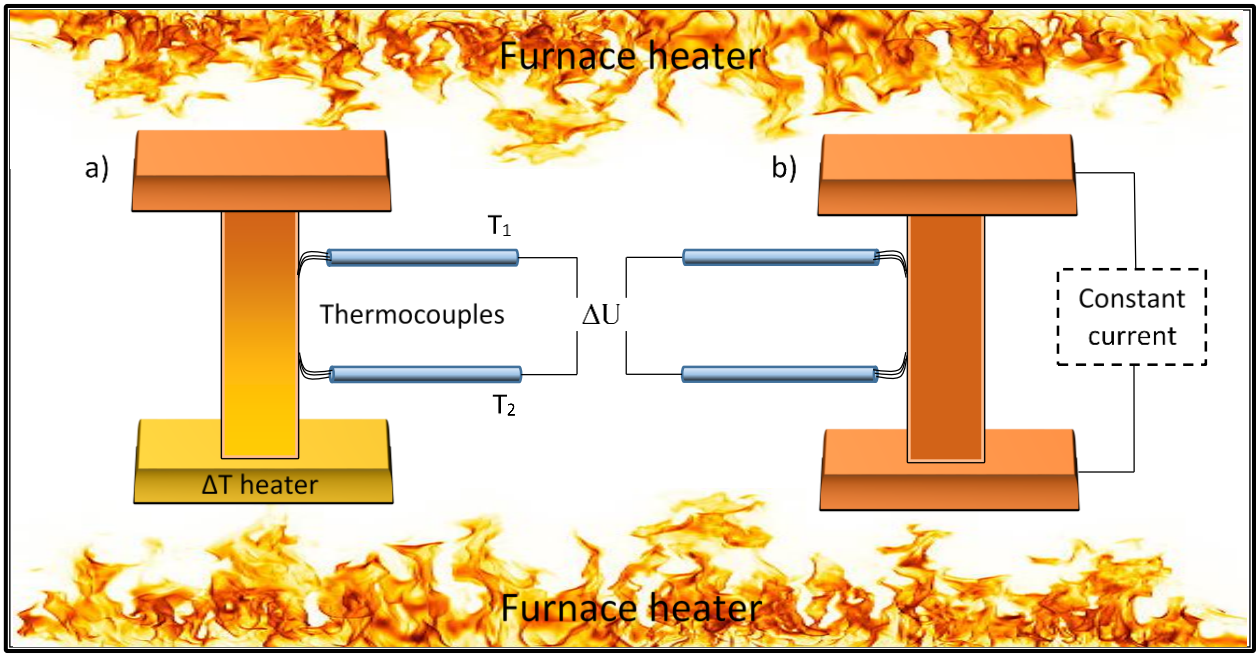

Figure 2. Setup for measuring Seebeck coefficient (a) and electrical conductivity (b).

The measurement is based on the definition of the Seebeck coefficient. The heater located under a base of a cuboidal sample creates a temperature difference ΔT (Figure 2a). Two thermocouples are utilized for simultaneous readings of temperature and voltage at two different points of the sample along the temperature gradient. A train of measurements of ΔU (voltage difference) and ΔT is required in order to calculate Seebeck coefficient, which will be a slope of the following line:

$$\Delta U(T) = \Delta U_0 + S\Delta T \qquad \text{(Eq.4)}$$

Ideally, this curve should pass through the origin, however the measuring equipment creates noise in terms of ΔU_0. ΔU_0 as well as S can be found utilizing the least square fit.

2.2.2 Electrical conductivity

The electrical conductivity is a measure of the ability of a material to conduct charge carriers with charge (e) and depends on the mobility of charge carriers (μ) and their concentration (n):

$$\sigma = n\mu e \qquad \text{(Eq.5)}$$

The electrical conductivity can be measured via a similar setup to that utilized for obtaining the Seebeck coefficient (Figure 2b). Instead of applying a temperature

gradient, now the sample is held at a uniform temperature. Running a constant and well defined current (I) through the sample, the thermocouples read the voltage (U) along the current direction (four-point probe). The electrical conductivity can then be determined taking into account a cross section area of the sample (A) and a distance between the thermocouples (l):

$$\sigma = \frac{I}{U} \cdot \frac{l}{A} \qquad \text{(Eq.6)}$$

2.2.3 Thermal conductivity

The thermal conductivity is a property describing a material's ability to conduct heat. In solid materials, heat is mainly transferred via phonons and electrons, which define lattice and electrical components of the thermal conductivity, respectively. The lattice contribution is difficult to estimate analytically, since it strongly depends on how atoms composing the system interact. The electrical contribution however can be fairly precisely obtained through the electrical conductivity, absolute temperature and Lorenz number (L) according to the Wiedemann–Franz law [34]:

$$\lambda_e = L\sigma T \qquad \text{(Eq.7)}$$

Since lattice thermal conductivity cannot be precisely calculated due to complexity of the material structure, one must conduct measurements to obtain it.

The total thermal conductivity can be experimentally estimated by either steady-state or transient methods. The most common steady-state method is the divided bar [35]. Here, the thermal conductivity is estimated utilizing a heat flow meter and temperature sensors. The main disadvantages of this technique are that it is time consuming and requires large samples. Among the transient methods, the Laser flash technique [36] is the conventional one. Here a laser is utilized to supply well-defined power, and the transient temperature response is then recorded in order to calculate the thermal diffusivity. Thermal conductivity can be estimated knowing the volumetric heat capacity of the sample. While the Laser Flash technique is powerful, it requires a certain geometry of the sample and does not measure the thermal conductivity directly.

2.2.4 Transient plane source technique

2.2.4.1 Basic principles

The Transient Plane Source (TPS) technique [21] is favorable for testing thermoelectric materials, since it estimates the thermal conductivity directly and no calibration is required, In other words, it is an absolute method. The technique is also flexible for various sample geometries and sample sizes via a set of different exchangeable sensors. The method was developed and presented in 1991 [22]. The TPS technique is able to estimate both the thermal conductivity (λ) and the thermal diffusivity (a) in a single experiment [37]. Due to the commonly-used circular double-spiraled-shaped probes used, so-called "hot discs", the technique is also commonly referred to as the hot disc technique. If a material under study is isotropic, the volumetric heat capacity can be also obtained:

$$\rho c_p = \frac{\lambda}{a} \qquad \text{(Eq.8)}$$

The measurement principal is based on placing a thin probe between two sample pieces of the same material, or in contact with one sample piece and arranging a highly-insulating backing material on the other side of the probe (Figure 3a). Alternatively, instead of a highly-insulating material, an adhesive can be used to bind the probe on the sample surface and arranging a vacuum on the other side of the probe. The TPS probe consists of an electrically conducting pattern, most commonly in the shape of a double spiral made of nickel, which is sandwiched between two thin electrically insulating materials, such as Kapton™, mica, etc. The hot disc probe serves as both a heat source and a temperature sensor; an electrical current passing through the double spiral induces Joule heating. Simultaneously, the monitoring of the probe's electrical resistance, and its variation over time, can be recomputed as a temperature response signal over time.

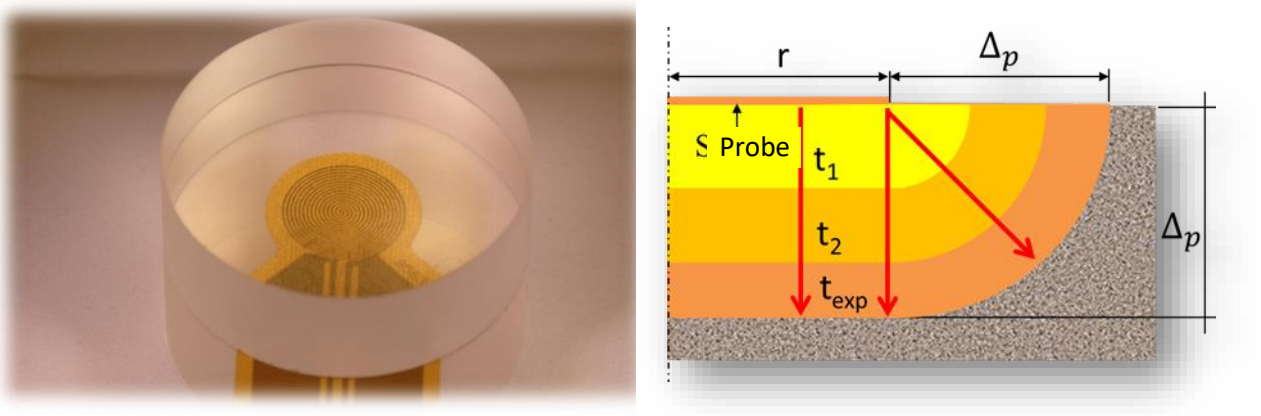

a) b)

Figure 3. A typical hot disc setup (a) and a cut of a cross section of a bulk sample under measurement showing propagation of heat (b).

Heat generated in the probe propagates through the sensor insulation, interface between the sensor and sample, and continues dissipating into the sample in a 3D, 2D or 1D manner depending on the sample geometry. The increase in the thermal depth of probing with time is illustrated in Figure 3b. The thermal depth of probing depends on the thermal diffusivity (a) of the sample and the time (t) of the heating according to:

$$\Delta_p = 2\sqrt{at} \qquad \text{(Eq.9)}$$

The constant 2 in Equation 9 is an empirical finding and depends on the sensitivity of the electronics utilized in the hot disc apparatus.

2.2.4.2 Isotropic standard (3D) measurements

Based on the sensitivity coefficients study [38], which determines a suitable time window to be used in the curve-fitting procedure, the estimation of thermal conductivity and thermal diffusivity proves most accurate, when the probing depth ranges from r to $2r$, where r is the sensor radius. This can also be expressed in terms of a relation between the total measurement time (t) and the characteristic time (θ) as $0.3\theta < t < \theta$ ($\theta = \frac{r^2}{a}$). This inequality can be fulfilled by choice of appropriate measurement time, which typically varies from 1 to 640 sec.

During the measurement, a precise source meter supplies a single-step current pulse with constant voltage, while a sensitive voltmeter (10^{-5} V) allows one to track the sensor spiral temperature variation to better than 10^{-3} K, due to the well-defined temperature

coefficient of resistance (α) of nickel. A Wheatstone bridge is used, with the hot disc probe representing one arm of this bridge, and a reference electrical resistance (R_S) is employed in the other arm. The temperature increase, ΔT(t), from the off-balance voltage reading, ΔU(t), recorded across the Wheatstone bridge, is calculated according to [21]:

$$\Delta T(t) = \frac{(R_S + R_L + R_0)\Delta U(t)}{[I_0 R_S - \Delta U(t)](\alpha R_0)} \qquad \text{(Eq.10)}$$

where R_L is the total resistance of the leads, R_0 is the initial resistance of the sensor double spiral, t is the duration of the experiment, I_0 is the current through the sensor at $t = 0$. Measurement power is chosen before the experiment to create a maximum temperature increase of around 2 – 5 K in the double spiral. During the experiment 200 data points of the temperature increase of the probe versus measurement time are recorded, as illustrated in Figure 4a.

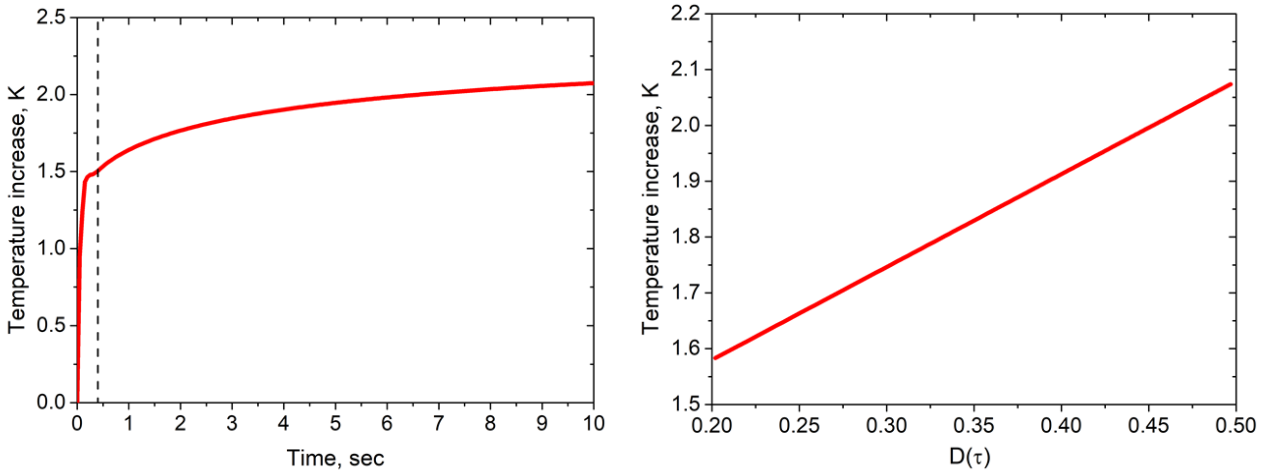

a) b)

Figure 4. A typical hot disc transient curve (a) and analyzed temperature increase vs. shape function (b).

A significant temperature jump in the beginning of the transient curve (to the left of the dashed line in Figure 4a), is caused by the thermal resistance of the probe insulation as well as by the thermal resistance in the interface between the probe and sample (a so-called thermal contact resistance). These initial points are hence omitted from the data analysis. The initial "disturbance" does therefore not influence results, since the heat flow becomes steady-state across this initial layer quickly, and the fitting model filters out these initial effects. The analysis of the transient curve involves iterations of

unknown parameters until the linear correlation coefficient of temperature increases versus shape function, $D(\tau)$ [22], takes its maximum value (Figure 4b). The slope of the model-fitted line is inversely proportional to the thermal conductivity, and the thermal diffusivity is contained in the iterated characteristic time:

$$\Delta T(\tau) = C + \frac{P_0}{\pi^{3/2} \cdot \lambda \cdot r} \cdot D(\tau) \quad \text{(Eq.11)}$$

where P_0 is the heat output in the probe, C represents the total thermal contact resistance and $\tau = \sqrt{\frac{t - t_{corr}}{\theta}}$, where t_{corr} is a time correction, which compensates initial variation in supplied power.

2.2.4.3 Anisotropic (3D) measurements

The thermal conductivity (λ) in Equation 11 is a geometric average of thermal conductivity in-plane and through-plane, *i.e.* $\sqrt{\lambda_{\text{in-plane}}\lambda_{\text{through-plane}}}$ [39]. However, the thermal diffusivity (a, which is included into characteristic time, θ) is in-plane, as follows from the TPS theory. Thus, with the knowledge of volumetric heat capacity, it is possible to split the thermal transport properties into in-plane and through-plane components utilizing Equation 8:

$$\lambda_{\text{in-plane}} = a_{\text{in-plane}} \cdot \rho c_p \quad \text{(Eq.12)}$$

$$\lambda_{\text{through-plane}} = \frac{\lambda^2}{\lambda_{\text{in-plane}}} \quad \text{(Eq.13)}$$

$$a_{\text{through-plane}} = \frac{\lambda_{\text{through-plane}}}{\rho c_p} \quad \text{(Eq.14)}$$

2.2.4.4 Thermal effusivity (1D) measurements

Thermal effusivity is a second-rank tensor property (Eff), which is possible to express as $Eff = \sqrt{\lambda \cdot \rho c_p}$ as stated by its definition [40]. Thermal effusivity of rod-shaped samples is obtained using the same computational procedure as described in Section 2.2.4.2, however, the $D(\tau)$ function in Equation 11 is replaced by τ (also assuming the change of geometry). Thus, the scalar property (Eff_n) can be computed as:

$$\Delta T = C + \frac{P_0\sqrt{t - t_{corr}}}{\pi^{1/2} \cdot A_{cross} \cdot Eff_n} \quad \text{(Eq.15)}$$

, where A_{cross} is the cross-section area of a rod sample.

With the knowledge of volumetric heat capacity, thermal conductivity as well as thermal diffusivity can readily be computed as:

$$\lambda_n = \frac{{Eff_n}^2}{\rho c_p} \quad \text{(Eq.16)}$$

$$\alpha_n = \left(\frac{Eff_n}{\rho c_p}\right)^2 \quad \text{(Eq.17)}$$

2.2.4.5 Heat capacity measurements

The heat capacity (c_p) of a material sample using a high conductive cell is measured in two steps [41]. First, an experiment is conducted utilizing a Hot Disk sensor and high thermally conductive cell (holder) wrapped in an insulation background material. This experiment is utilized to determine heat losses into the background material (Q). The power output from the sensing element (P), its average temperature increase ($d\bar{T}$) and corresponding dependance on measurement time (t) is given as:

$$P_1(t) = \left(mc_p\right)_{holder} \frac{d\overline{T_1}}{dt}(t) + |Q_1(t)| \quad \text{(Eq.18)}$$

, where m is mass. If a sample is added into the holder, then:

$$P_2(t) = \left\{\left(mc_p\right)_{holder} + \left(mc_p\right)_{sample}\right\}\frac{d\overline{T_2}}{dt}(t) + |Q_2(t)| \quad \text{(Eq.19)}$$

After rearrangement of Equations 18 and 19, the heat capacity of the sample is:

$$\left(mc_p\right)_{sample} = \frac{\overline{P_2}}{\delta_2} - \frac{\overline{P_1}}{\delta_1} \quad \text{(Eq.20)}$$

, where $\delta = \overline{\left(\frac{dT}{dt}\right)}$

2.3 Enhancing properties of thermoelectric materials

2.3.1 Phase diagram

Microstructuring of thermoelectric materials can be achieved utilizing phase diagrams, which form a graphical representation of thermodynamically distinct phases. These occur and coexist at equilibrium at different temperature, pressure, chemical composition conditions, etc. An existence of thermodynamically distinct phases is described by the change in Gibbs free energy. A new phase appears at a certain temperature and ratio of the system components, if this leads to a reduction of the Gibbs free energy. In the context of the current thesis, it is relevant to talk about binary isobaric phase diagrams of the type temperature vs. atom fraction, an example of which is presented in Figure 5.

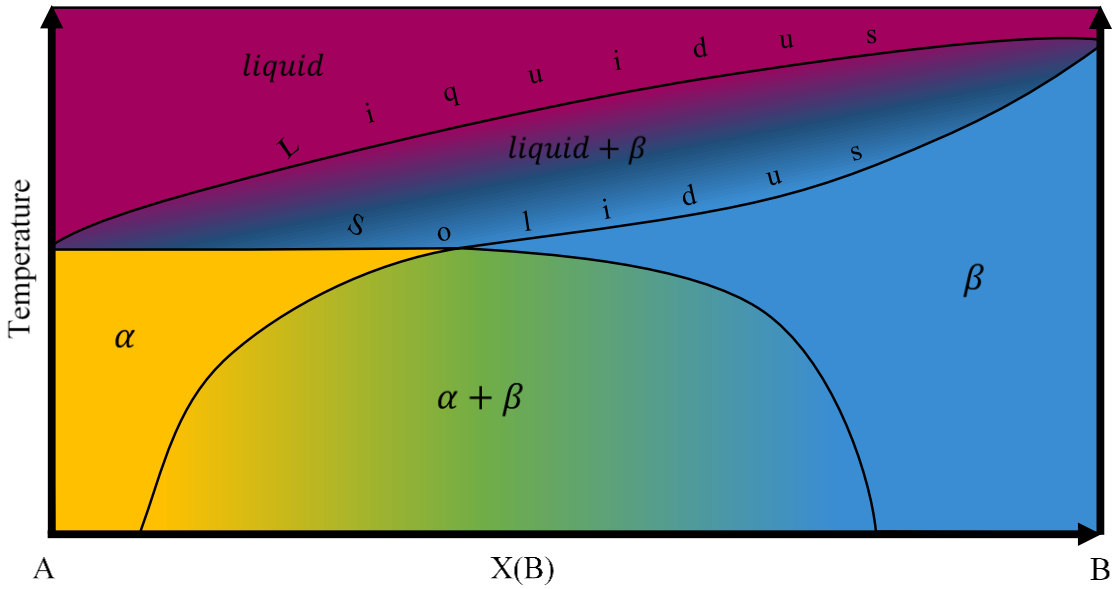

Figure 5. Example of a binary isobaric phase diagram with a miscibility gap.

There are three thermodynamically distinct phases in the phase diagram in Figure 5: liquid phase, solid phase α and solid phase β. When temperature of the system increases, both solid phases start to melt at the temperature known as solidus and stop melting at the temperature called liquidus, above which only the liquid phase exists. Enclosed by the liquidus and solidus curves is the freezing range, where both solid and liquid phases are present. The solid region, which is below the solidus curve, consists of two phases, *i.e.* α and β, which differ only by the crystal lattice parameter. The α-phase is able to dissolve a certain amount of component B in its matrix, and β-phase a certain

amount of component A. The solubility limit of each phase increases with temperature rise and draws a bell-like binodal (also called coexistence temperature or critical demixing temperature) curve, where a transformation occurs from miscibility (stable single phase) to a metastable or unstable solid solution [42].

Metastable or unstable solid solutions normally decompose into a physical mixture of phases α and β, which occurs inside a miscibility gap. The miscibility gap is a region constrained by the binodal lines. The phase separation will not occur if the single solid solution is quenched. Thus, a quick change in temperature brings the solid solution into a state, when its atoms are frozen in their current positions, *i.e.* atoms are not mobile enough to diffuse over long distances. If one gently cools the single solid solution, nuclei of a new phase start appearing and its composition will be defined by the binodal lines. The rate of formation of new nuclei decreases with decreasing temperature, while their growth rate increases. Continuing reducing the temperature, the kinetics of the system becomes low, so that the atoms cannot diffuse long distances, and eventually the phase separation ends. By varying the composition, treatment temperature and cooling rate, it is possible to affect different stages of the transformations and acquire a microstructure of interest. For example, treating a solid solution at a temperature close to the binodal curve and avoiding the stage of nuclei growth, multiple dispersed precipitations will be formed. Such precipitations influence the host material properties, such as increased hardness and strength, reduced thermal conductivity and plasticity, etc. Another example is if the stage of new-phase nuclei formation is skipped. Then the system undergoes a special transformation, called spinodal decomposition.

2.3.2 Spinodal decomposition

Spinodal decomposition is a mechanism by which a solution of two or more components decomposes into thermodynamically distinct phases with different chemical compositions, crystal lattices and properties. Opposite to the mechanism of nucleation and growth described above, spinodal decomposition occurs uniformly throughout the relevant material and is determined solely by diffusion. The microstructure formed due to such transformation is characterized by the fine lamellae-like microstructure (Figure 6), which, in turn, influences material properties even more than what could be achieved by nucleation and growth [19].

Figure 6. Schematic illustration of the progress of spinodal transformation over time.

Spinodal decomposition can take place when a solution enters the unstable region of the phase diagram. This unstable region lies within the miscibility gap and can be found by determining a common tangent of the free-energy curve ($\frac{d^2G}{dX^2}$) at all temperatures in the binodal region. Hence, a narrower region, a so-called spinodal one, will be formed (dashed black curve in Figure 7). The binodal and spinodal then meet at the critical point.

If a solid solution with the composition X_0' is homogenized in the single-phase region α at the temperature T_1, and is then quenched to the lower temperature T_2, which lies in the spinodal region, its free energy will be G_0. Since G_0 is not the lowest free-energy of the system, the solid solution will immediately be rendered unstable. Thus, it will tend to produce the phases with the lowest G value at T_2, *i.e.* alloys with the compositions X_1 and X_2. There is no barrier to form the alloy of composition X_1, while the composition X_2 can be reached by overcoming the point with the maximum G value. Since G_0 is located on the section, where $\frac{d^2G}{dX^2}$ is negative, *i.e.* within the inflection points ($\frac{d^2G}{dX^2} = 0$), there is no significant difference between G_0 and G_{max}; hence the maxima can be easily overcome, and composition X_2 will be formed.

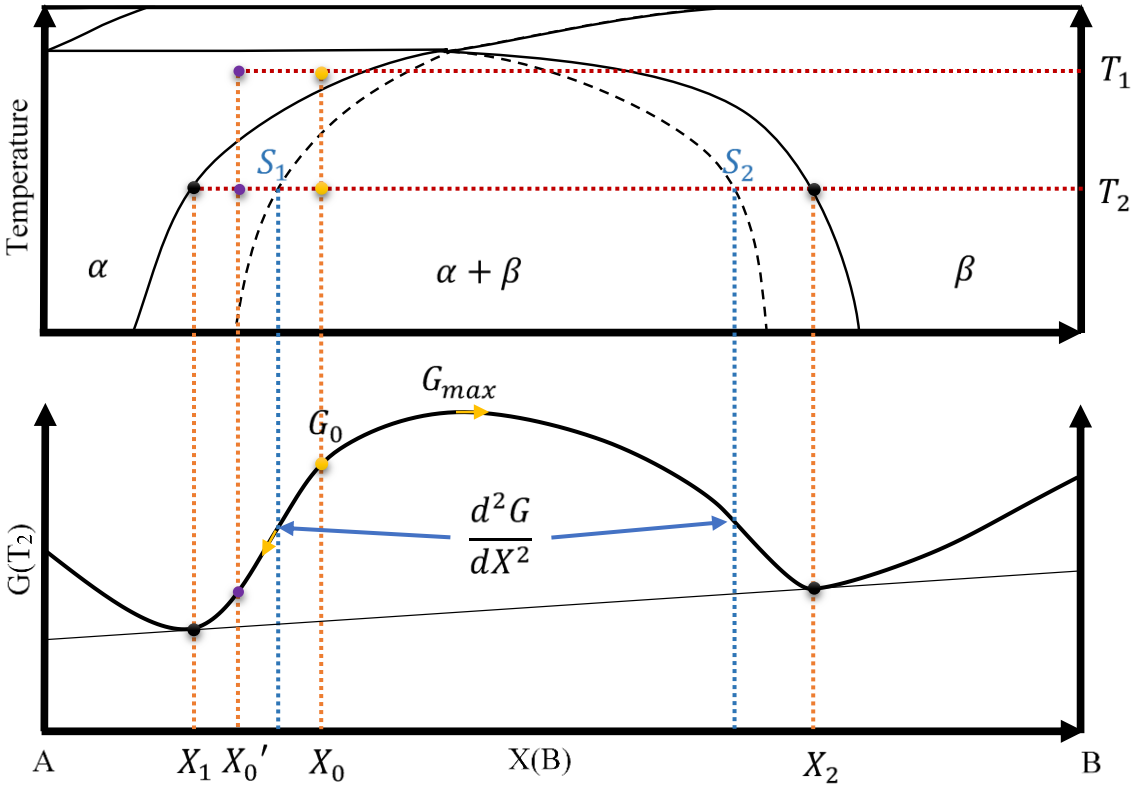

Figure 7. A cut of the phase diagram in Figure 5 and corresponding free-energy curve at the temperature T_2.

In comparison, if the solid solution of the composition X_0 will be homogenized at T_1 and quenched to T_2, it will be located outside the spinodal region in the metastable region. The free energy of the system can only be reduced by the formation of nuclei of a new phase with a composition very different from the matrix. Therefore, outside the spinodal the transformation must proceed by the mechanism of nucleation and growth. To reach the spinodal region of the phase diagram, a transition must take the material through the binodal region. Often, phase separation will occur via nucleation and growth during this transition, and spinodal decomposition will not be observed. To observe spinodal decomposition, a very fast transition (quenching) is required in order to move from the stable to the spinodally unstable region of the phase diagram [19].

2.3.3 Panascopic approach

The panascopic approach [10] is based on hierarchical microstructuring, which consists of architecting the material constitution on mutiple length scales. For thermoelectric materials, such an approach allows one to decrease the lattice component of thermal conductivity significantly without a corresponding loss of electrical conductivity, which in turn leads to an enhancement of the thermoelectric figure-of-merit ZT. The reduction

of thermal conductivity occurs due to the presence of "obstacles" of different sizes, in which heat-carrying phonons of a broad range of frequencies are scattered. These "obstacles" or sources of scattering cover the length from atomic-scale lattice disorder and nanoscale endotaxial precipitates to mesoscale grain boundaries (Figure 8) [10].

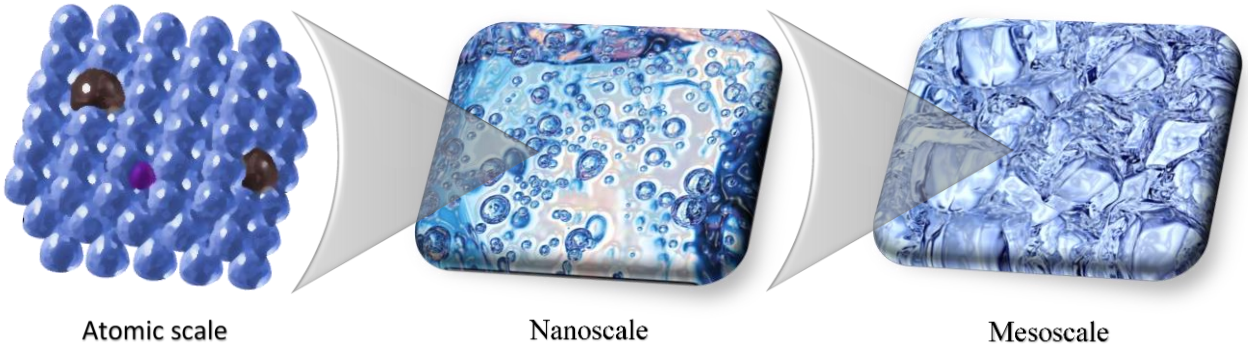

Figure 8. Illustration of the panascopic approach with a hierarchical architecture.

Atomic doping is commonly applicable to thermoelectric materials as a way to tune the charge carriers' concentration. Moreover, atoms of other elements, which substitute the matrix atoms or are "squeezed" into interstitial sites, distort the crystal lattice, so that the high-frequency phonons are restricted to propagate through such disorder [10].

Increasing the length scale of disorder screens the phonons of lower frequency. Thus, a presence of another phase in the matrix material is able to reduce the lattice thermal conductivity even further. The foreign phase can be embedded in a bulk matrix mechanically or be produced in-situ during phase separation. To avoid the reduction of electron mobility, this phase should be arranged as endotaxial, *i.e.* the crystallographic planes of the matrix and precipitates should be nearly mutually aligned. The border between the phases, which possess dislocations formed due to the mismatch of the crystal parameters, will also scatter phonons [10].

A higher density of dislocations can be found in the grain boundaries. The disorder simply accrues from the definition of the grains in a polycrystalline material. Although grains are normally homogeneous, *i.e.* have the same composition and arrangement of phases, they are oriented differently in space so that their crystallographic planes are misaligned. In addition, the size of the grains could be comparable to the mean free path of low frequency phonons leading to the further reduction of lattice thermal conductivity. The grain size can be controlled via compaction of a milled and sieved powder utilizing the spark plasma sintering technique [10].

2.4 Spark plasma sintering for powder compaction

Powder compaction occurs at higher temperatures below the melting point when atoms become sufficiently mobile and tend to fill voids between powder particles. Alongside with densification, other undesirable processes take place, such as recrystallization or phase separation. Unlike other methods of compaction, *e.g.* hot pressing, which are time-consuming, Spark Plasma Sintering (SPS) allows rapid compaction, which suppresses the grain growth and other transformations of the microstructure in question [43]. SPS is a low voltage, direct current (DC), pulsed-current activated, pressure-assisted sintering and synthesis technique [44-46]. It consists of a mechanical loading system, which acts at the same time as high-power electrical circuit, placed in a controlled atmosphere (Figure 9).

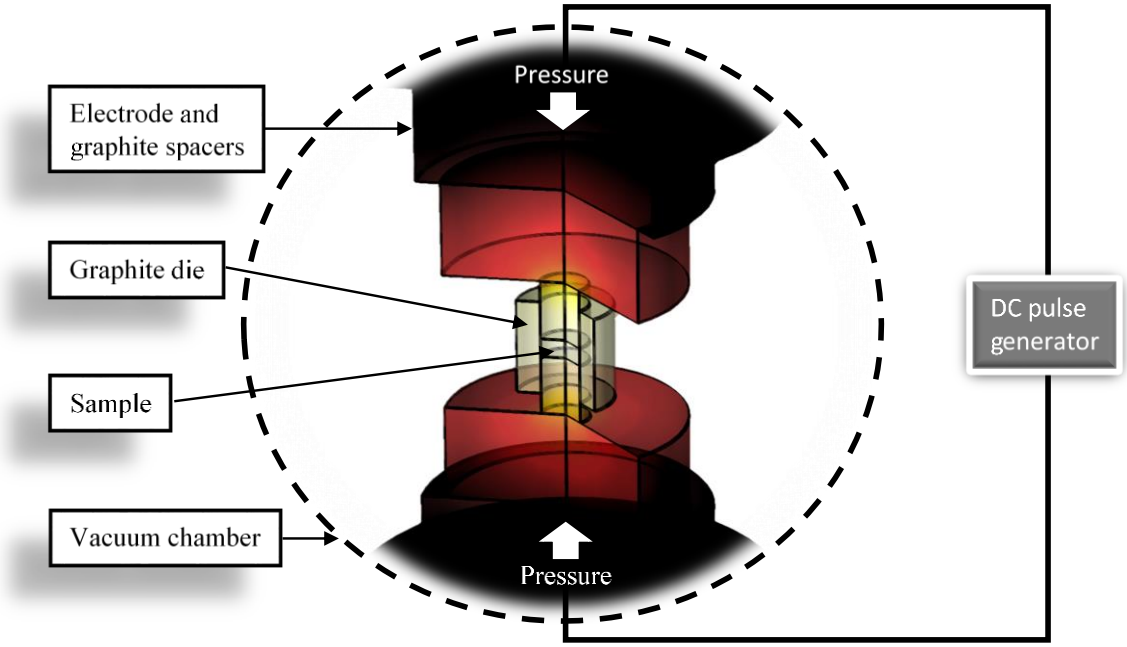

Figure 9. Cross section of a spark plasma sintering setup for powder compaction.

Before sintering, the sample (powder) is placed between graphite punches in a graphite die and is surrounded by graphite paper or insulation, *e.g.* BN. Then, the die is placed between graphite spacers, which are in contact with upper and lower electrodes of the SPS apparatus. When next uniaxial mechanical pressure is applied to the punches and the chamber is evacuated, the sintering can begin. The temperature profile is programmed and is controlled via the duration and magnitude of the current pulses supplied from the affiliated DC pulse generator. Readings of the sample temperature are performed by a thermocouple or pyrometer. High current (typically from 1 to 10 kA), which flows through both the die and electrically conducting sample, and low voltage

(typically below 10 V) induce efficient Joule heating, thus, achieving up to a 1000 °C/min heating rate. Standard cooling rates are up to 150 °C/min, which makes it possible to quench samples. The simultaneous application of pressure and electrical current enhances densification. A mechanism of the current-activated sintering is presented in Figure 10.

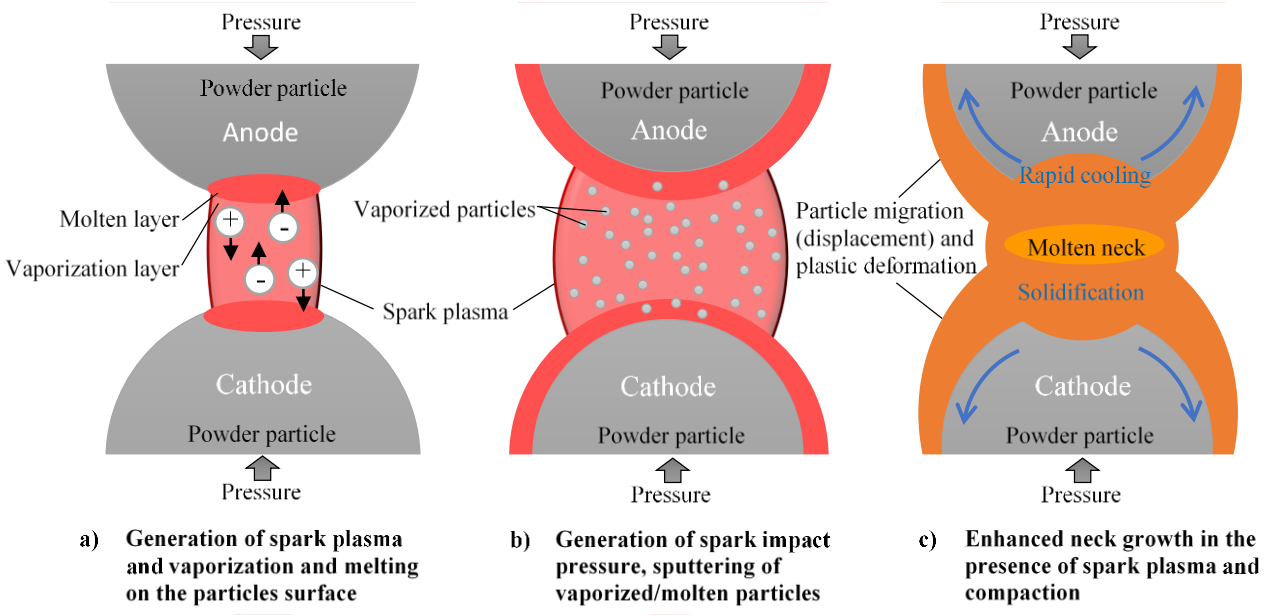

Figure 10. Mechanism of current-activated sintering during operation of SPS equipment.

When a spark discharge appears in a gap or at the contact point between powder particles, a local high temperature-state (discharge column) of several to ten thousands of degrees centigrade is generated momentarily (Figure 10a). This causes evaporation and melting on the surface of the particles, and "necks" are formed around the area of contact between them. The high temperature sputtering phenomenon generated by the spark plasma, as well as spark impact pressure, eliminates adsorptive gas and impurities existing on the surface of the powder particles (Figure 10b). The action of the electrical field causes high-speed diffusion due to the high-speed migration of ions to voids, which increases the “neck” diameter. A growth of the “neck” reduces the local current density, and therefore the local temperature decreases below the melting point (Figure 10c). At the same time, the applied uniaxial pressure deforms the particles, packing them tighter. The later stages include sliding and annihilation of defects, such as vacancies, dislocations, etc. [47]. The microstructure of the synthesized or sintered samples can be characterized by different techniques, *e.g.* XRD, SEM/EDS, TEM, etc.

2.5 Structural characterization by X-ray diffraction

X-Ray Diffraction (XRD) is a technique that allows for the determination of the atomic and molecular structure of a crystal. It is based on the utilization of an X-ray beam, which is elastically scattered by the electron cloud of the atoms and is diffracted in specific directions. The reflections of X-rays are observed at certain angles between the incident beam and the sample surface, when the X-rays undergo constructive interference (Figure 11) [48].

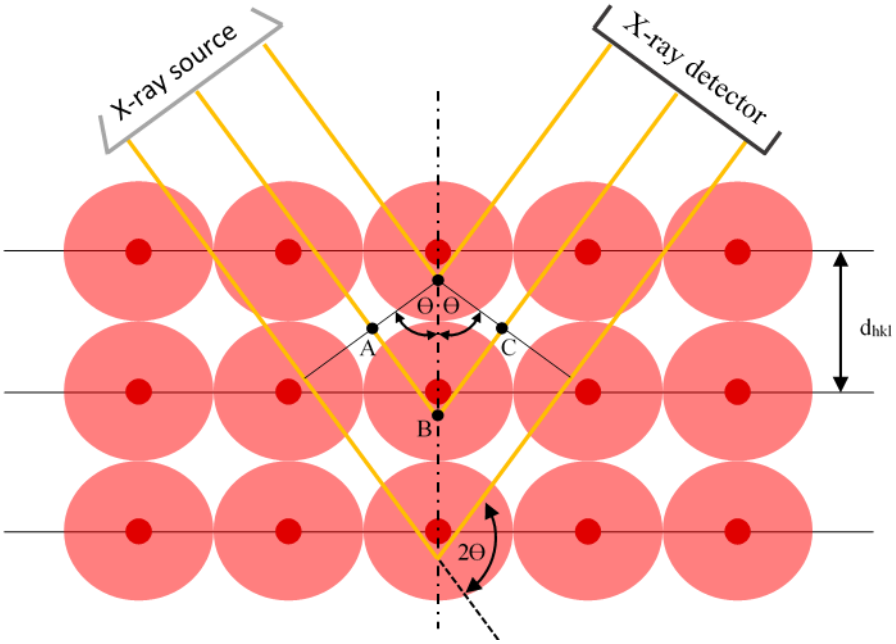

Figure 11. Illustration of the X-ray diffraction technique in which Bragg reflections from a set of crystal planes with a spacing d_{hkl} are collected and analyzed. This to provide information of atomic positions and composition of the material, allowing for structural determination and identification.

Let us consider an incoming parallel beam of X-rays, which hits a set of crystallographic planes with Miller indices (hkl) at a certain angle (θ), and scatters at the same angle towards the detector. Geometrically, since these two angles are equal, the line segments AB and BC are also equal, and their sum represents the difference in the X-rays' path length. The light will constructively interfere (or will be in-phase) if the difference in the path will be proportional to its wavelength by an integer number (n) of the X-ray wavelength (λ), *i.e.* $AB + BC = n\lambda$. In addition, since the interplanar distance d_{hkl} is a hypotenuse, the following is true $AB = BC = d_{hkl} \sin\theta$. Combining the last two sentences, Bragg's law can be derived as follows:

$$n\lambda = 2d_{hkl}\sin\theta \qquad \text{(Eq.21)}$$

Equation 21 relates the spacing between the crystal planes (d_{hkl}) to the particular Bragg angle (θ). Thus, by measuring θ and intensity of X-rays and knowing their wavelength, it is possible to calculate the dimensions of a unit cell, taking into account the type of applicable crystal lattice. The intensity of a reflection measured by the detector (I_{hkl}) is proportional to a square of the so-called structural factor (F_{hkl}), which is dependent on both the position of each atom (x, y, z) and its scattering factor (f):

$$F(hkl) = \sum_j f_j e^{hx_j + ky_j + lz_j} \qquad \text{(Eq.22)}$$

Most often, a real material proves polycrystalline, *i.e.* it consists of a large number of tiny crystals or grains, which are randomly oriented. If such a sample is placed in a path of a monochromatic X-ray beam, diffraction will occur from the crystallographic planes in those crystallites, which happen to be oriented at the correct angle to fulfil the Bragg condition (Equation 21). In this case, the reflections of X-rays will lie on the surface of cones, whose semiapex angles are equal to the deflection angle 2θ [49]. This also allows for testing composite materials consisting of different phases, and also for performing quantitative analysis alongside with a qualitative one. A drawback here is that the reflections which corresponded to different phases can overlap. However, this problem can be solved utilizing curve fitting software, which is based on a model of the crystal structure, using for example, Rietveld refinement [50].

The Rietveld refinement is a technique that was developed for refining crystal structures from powder diffraction data. The method assumes that each diffraction peak has *e.g.* a Gaussian or Lorentzian shape, and these peaks can overlap. The main idea is to fit the calculated pattern to the measured one. This, however, requires a certain knowledge about the structure, *e.g.* type of crystal lattice. The comparison of the patterns is then carried out via the least square fit:

$$R = \sum_i w_i \left(y_i^{obs} - y_i^{calc}\right)^2 = minimum \qquad \text{(Eq.23)}$$

Where w_i is a weight of each observation, and y_i^{obs} and y_i^{calc} are the observed and calculated intensities, respectively. A requisite software performs iteration of parameters, such as unit cell dimensions, background, temperature factor, etc., until R

takes a minimal value. By comparing the intensities, it is then also possible to calculate a weight ratio of the constituent phases. Moreover, the Rietveld refinement is able to provide information about the crystallite size, lattice strain, composition of phases, etc. [51].

Chapter 3

$Mg_2Si_{1-x}Sn_x$ alloys

3.1 Advantages and disadvantages of using $Mg_2Si_{1-x}Sn_x$ alloys

Well-performing thermoelectric materials normally consist of noble, rare, toxic and/or expensive elements. Moreover, certain efficient composites can be produced only in small quantities, *e.g.* multilayered devices, which limits their ubiquitous usage.

By contrast, magnesium silicide-stannide alloys are unique materials for thermoelectric applications, since they are composed of inexpensive, abundant, environmentally-friendly elements that can be produced in large quantities. The alloys themselves possess good mechanical properties, low density and are also oxygen resistant up to 350-400 °C [52]. They evince fairly high dimensionless figure-of-merit zT, which could be as high as 1.4 [7, 53-55]. And there is the possibility of further improvements of these alloys utilizing, *e.g.* microstructuring methods.

Moreover, simple direct solid-state reaction synthesis allows for large-scale production of $Mg_2Si_{1-x}Sn_x$ (as done in Paper III). The material could also be produced by other methods, *e.g.* by homogenization of precursors Mg_2Si and Mg_2Sn (as shown in Paper II) or yet again by mechanical alloying, or via the liquid phase process, etc. Hence, there is some flexibility in the ways of controlling the microstructure of the alloys.

Because the material reacts with water, forming an explosive silane gas, it must be stored and utilized under dry conditions or be covered with a protective coating. However, the resistance against reacting with water can be improved by increasing the Sn content [29]. Due to the presence of a miscibility gap suggested by existing phase diagrams [11-15] and as observed in Papers II and III, the solid solutions tend to change their microstructure, which limits the operational temperature of the hot side. Moreover, there is a large uncertainty between the available phase diagrams [11-15], which complicates the prediction of the final microstructure and physical properties. Ternary or even more complex phase diagrams could be required to understand the system better, because, *e.g.* Mg and doping content influence the behaviour of the system as discussed in Paper III. Nevertheless, this general finding could be utilized to create more complex and more beneficial microstructures for thermoelectric applications.

It should be observed that an undesirable inclusion of MgO commonly occurs on the grain boundaries and reduces the thermoelectric performance [56]. Hence, a more sophisticated method should be employed in the material preparation, *e.g.* the usage of inert atmosphere and sintering machines that offer a better degasification. Furthermore, one should note that highly atomically and microstructurally distorted single-solid solutions are brittle, which typically leads to cracking of the sintered tablets. This also elucidates the importance of careful material preparation.

3.2 Crystal structure and structural characterization of $Mg_2Si_{1-x}Sn_x$

Magnesium silicide-stannide alloys have a cubic anti-fluorite crystal structure and the space group $Fm\bar{3}m$ (Figure 12a). The same is true for their precursors, Mg_2Si (Figure 12b) and Mg_2Sn (Figure 12c), which have different lattice parameters of 6.3552 and 6.7654 Å, respectively. Varying the ratio between Sn/Si, the crystal lattice parameter of the final product should change proportionally [57].

The typically used n-type dopants, Bi and Sb, have a certain solubility level in $Mg_2Si_{1-x}Sn_x$ alloys and substitute the crystal site shared by Si and Sn. It is suggested in the literature that Bi accumulates equally in the Si-rich and Sn-rich phases [58]. However, Polymeris et al. [59] argue that Bi prefers to substitute Sn atoms due to their similar radii.

The bonding nature of the material is a mixture of covalent and ionic, but it has been shown that the ionic character dominates [60]. Both magnesium silicide and magnesium stannide are semiconductors, with band gaps around 2.27 and 0.23 eV, respectively [61].

a) b) c)

Figure 12. Crystal structure of magnesium silicide-stannide alloys (a): yellow atoms – Mg, purple atoms – Si or Sn; Freshly synthesized Mg_2Si (b) and Mg_2Sn (c).

3.2.1 X-ray diffraction and Rietveld refinement

Multiphase systems can be successfully studied via XRD. Utilizing the Rietveld method, it is normally possible to identify all present phases as well as to acquire their quantities. However, the refinement can sometimes fail, *e.g.* due to the following reasons.

For phases with a similar composition, X-ray reflections appear close to each other (*cf.* Figure 13), which complicates the peak fitting procedure. This can be resolved by switching to synchrotron facilities or by manual guidance of the refinement. Synchrotron sources provide radiation of a very high intensity, which allows for collecting an XRD pattern including high 2θ values, where the spacing between the peaks is greater. Without access to synchrotrons, careful monitoring of the peak-fitting procedure on patterns acquired by typical diffractometers often yields reasonable results. Thus, the peak shape as well as the crystal parameters have to be provided as input to a reasonable structural model, in order to direct the software algorithm towards a realistic solution. The Topas® software by Bruker offers a decent control of the entire data fitting process. Therefore, this software was utilized for studying $Mg_2Si_{1-x}Sn_x$ alloys (*cf.* Paper II and Paper III), especially, when spinodal decomposition occurs as it leads to the formation of a set of solid solutions with similar compositions.

Another risk of failure with the Rietveld method occurs when studying a compound consisting of elements with very different atomic masses. This problem originates from the inherent properties of X-rays. Heavy atoms, such as tin, reflect X-rays more efficiently than light atoms, like silicon. Such mismatch of scattering parameters may cause unreasonable values, when refining occupancy factors of Si ($occ(Si)$) and Sn ($occ(Sn)$) for phases of a type $Mg_2Si_{1-x}Sn_x$. The software often tends to overestimate the amount of Sn atoms on the lattice sites shared with Si (Figure 12a). When performing a refinement, the occupancy factor of Sn often approaches a value 1 or even exceeds it, thus violating the law $occ(Si) + occ(Sn) = 1$ (where X is a molar fraction of the corresponding atom occupying main sites of the fcc cell). Therefore, the refinement of $Mg_2Si_{1-x}Sn_x$ structures in Paper II was based on the following assumptions. The occupancy factor of Si was set to be $occ(Si) = 1 - occ(Sn)$, whereas $occ(Sn)$ was calculated utilizing Vegard's law [57], which assumes a linear dependency of the lattice parameter (lp) and $occ(Sn)$ of a $Mg_2Si_{1-x}Sn_x$ solid solution, produced from the precursors with the same type of crystal lattice:

$$occ(Sn) = \frac{lp(Mg_2Si_{1-x}Sn_x) - lp(Mg_2Si)}{lp(Mg_2Sn) - lp(Mg_2Si)} \qquad \text{(Eq.24)}$$

Equation 24 is an approximation of the actual system behavior, which allows us to obtain the composition of the constituent phases fairly accurately. This can be verified by comparing the calculated and nominal compositions of the compounds (Tables 1 and 2 in Paper II). However, when analyzing strained structures, the total quantity of Sn in $Mg_2Si_{1-x}Sn_x$ can easily be underestimated or overestimated, and it is not clear whether the error comes from this approximation or from the utilized Rietveld refinement fitting method, or other factors that also may play a role.

When fitting the reflections of a Bi-doped compound, it was assumed that Bi shares the same site with Si and Sn, and its occupancy factor ($occ(Bi)$) is constant (Paper III). The calculation of the occupancy factor for Si was modified to $occ(Si) = 1 - occ(Sn) - occ(Bi)$.

In Paper III, a number of phases of type Mg_2X (where X stands for Si, Sn or Bi) were chosen for the refinement based on visual examination of the shapes of overlapping XRD reflections. Before each refinement, the cell parameter, the peak shape parameters, and the scaling factor of each phase were adjusted manually to ensure a reasonable final fit. In addition, every iteration step of the refinement was observed visually. The following

parameters were refined in a single initial step for every sample: cell parameters, zero error, background, scale factors, peak shape parameters, and parameter of the utilized simple axial models. After that, the temperature factors on each site were also refined. Such approach allowed to achieve good fitting with R_{wp} around 3.5 (Figure 13).

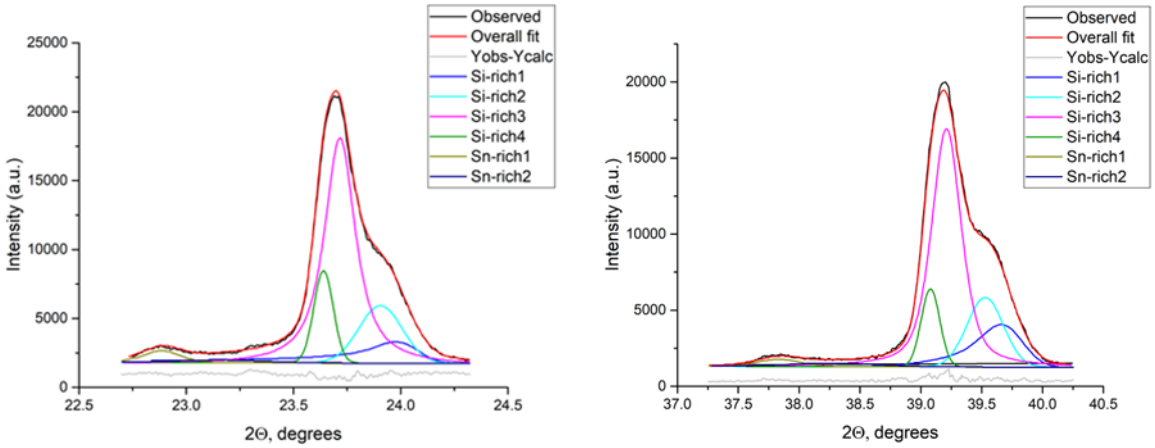

Figure 13. Rietveld refinement fit for $Mg_2[(Si_{0.6}Sn_{0.4})_{0.975}]Bi_{0.025}$ treated for 640 min: a) reflection (111); b) reflection (220).

3.2.2 Other structural characterization methods

Neutron diffraction could be considered for studying the crystal structure of $Mg_2Si_{1-x}Sn_x$ alloys, because the neutrons interact with nuclei, not with the electron cloud as in the case of X-rays. However, neutron scattering cross sections of elements do not depend linearly on the element number and in fact also vary between different isotopes of the same element, which needs to be taken into account when deciding on its usefulness for solving a given structural problem. Also, access to neutron sources is even more limited than synchrotron sources.

Additional techniques, such as Scanning Electron Microscopy (SEM) and Energy-Dispersive X-ray spectroscopy (EDX), can also be utilized to study the morphology and elemental composition of $Mg_2Si_{1-x}Sn_x$. However, it is difficult to acquire data on precise composition of the phases, *e.g.* by EDXS, due to a poorly defined interaction volume of electrons in the sample material. Moreover, the resolution of both SEM and EDXS does not allow to distinguish spinodally-decomposed phases, since the period of their alternation is at nanoscale and their compositions could be similar.

Lamellae-like or strained structures can be characterized also by Transmission Electron Microscopy (TEM) and Small-Angle X-ray Scattering (SAXS), which methods are able to track nanoscale electron density variation. While TEM is focused on the local structures, SAXS is a bulk technique, so that the acquired results represent the entire sample. On the other hand, if the alternating lamellae-like phases are either distributed or spaced unevenly, SAXS will not be able to yield informative results. Finally, atomic mass spectroscopy could be utilized to reveal spinodal microstructure. However, this technique operates with small material quantities (couple of hundreds nanometers) and hence allows one to observe merely a tiny fraction of the material, which notably does not represent the microstructure of the entire sample. Thus, in sum, X-ray diffraction techniques are favorable to use when studying phase separation in the system Mg_2Si–Mg_2Sn.

3.3 Preparation of $Mg_2Si_{1-x}Sn_x$

3.3.1 Synthesis and homogenization

$Mg_2Si_{1-x}Sn_x$ can be prepared via liquid- or solid-state reactions from Mg_2Si and Mg_2Sn, from Mg–Si–Sn metals directly, or from other precursors. From a practical point of view and to avoid liquid phase, magnesium silicide-stannide in Paper II was synthesized from Mg_2Si and Mg_2Sn, which compounds in turn were made from pure metals. To accelerate the reaction, the constituents were ball-milled before the synthesis. It is convenient to carry out the reaction in alumina crucibles in an air-tight tubular furnace. This allows for the production of large quantities of material in a desired atmosphere. Since magnesium silicide-stannide alloys are reactive with air at elevated temperatures, inert gas such as Ar should be utilized. An additive of 10 vol% of H_2 is recommended to remove oxygen, which is normally adsorbed by the surface of powder particles.

The synthesis scheme to produce Mg_2Si and Mg_2Sn includes two stages. In the first stage, the corresponding metals (Mg and Si or Sn) are ball-milled separately and then together, and are treated in the furnace at 600 °C for 16 hours in the Ar atmosphere with 10 vol% of H_2. An excess of Mg around 7.5 mol% should be added to compensate for evaporation losses. The second stage serves to achieve homogeneity. The semi-finished powders are ball-milled again and treated for 10 hours at 600 °C in the atmosphere of Ar with 10 vol% of H_2.

When carrying out the synthesis of $Mg_2Si_{1-x}Sn_x$, the treatment time and temperature used will differ and depend on the phase diagram Mg_2Si–Mg_2Sn. Magnesium silicide and magnesium stannide merge into a single-solid solution, if the choice of temperature vs. composition lies inside the single-phase region of the phase diagram. Due to the uncertainty in the available phase diagrams [11-15] (Figure 14a), the shape of the single-phase regions and the miscibility gap are not reliably available. Hence, in Paper II a set of experiments with different parameters were performed in order to obtain suitable conditions for the synthesis of $Mg_2Si_{1-x}Sn_x$ in the Si-rich region. For instance, it is possible to see the presence of the single-phase region by XRD, when treating the composition $Mg_2Si_{0.87}Sn_{0.13}$ at 700 °C (Figure 14b). Since both Mg_2Si and Mg_2Sn have the same structure, but different crystal parameters, they have the same set of X-ray reflections (Figure 14b, black curve), which appear at slightly different Bragg angles (reflections for Mg_2Sn comes at lower 2θ values due to a bigger lattice volume compared to Mg_2Si). Observing the black, red and blue patterns in Figure 14b, it is clear that increasing the treatment time a set of reflections corresponding to Mg_2Sn phase moving towards higher 2θ values. This proves the substitution of Sn by Si in the Mg_2Sn lattice. At the same time, the substituted Sn accumulates in the Mg_2Si lattice causing the increase in the lattice parameter of Mg_2Si. Thus, with increasing dwelling time, the reflections of Si-rich and Sn-rich intermediate phases move towards each other and eventually merge into a single solid solution with composition $Mg_2Si_{0.87}Sn_{0.13}$.

To achieve better homogeneity and speed up the reaction, the treatment temperature can be increased. Synthesizing $Mg_2Si_{1-x}Sn_x$ with the composition approaching X(Sn)~0.40, the increase of the treatment temperature is also of interest, since the single-phase region narrows down according to some sources [11,14]. At the same time, the treatment temperature cannot exceed the values defined by solidus in order to avoid the formation of a liquid phase, which is especially important when sintering a sample in SPS. To illustrate, increasing synthesis temperature to 780 °C speeds up the reaction and allows the formation of almost pure single solid solution $Mg_2Si_{0.87}Sn_{0.13}$, as can be observed in Figure 14b (note the purple and green patterns). A small amount of the Sn-rich phase, besides the major Si-rich phase in these patterns, remains present regardless of the treatment time, which suggests that it is formed upon cooling (the effect of cooling is discussed in Section 3.4.3).

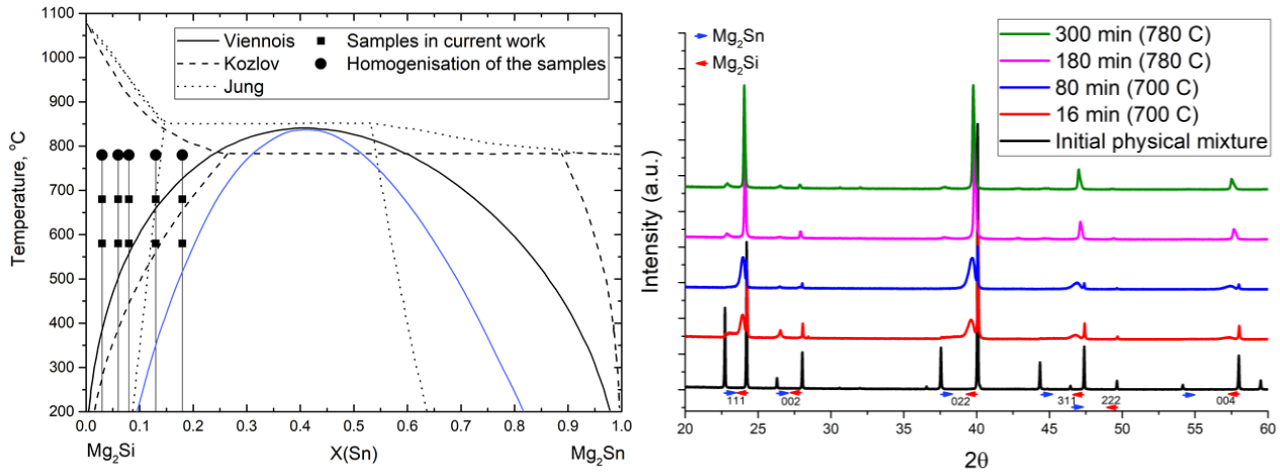

a) b)

Figure 14. Existing quasi-binary phase diagrams of Mg_2Si–Mg_2Sn [11-14] highlighting experiments done in Paper II (blue solid curve shows an approx. shape of the spinodal region according to Viennois et al. [14]) (a) and ex-situ XRD analysis of the $Mg_2Si_{0.87}Sn_{0.13}$ solid solution formation (b).

Homogenization experiments of Bi-doped $Mg_2Si_{0.82}Sn_{0.18}$ (Sn18) and $Mg_2Si_{0.60}Sn_{0.40}$ (Sn40) were also performed in Paper III. According to the literature, a successful homogenization of both compositions is achieved above 600 °C [15, 62-64]. However, as for the Sn40 composition, most of phase diagrams suggest that there is no single-phase region up to the solidus temperature. And only a recently-published phase diagram accounts for the existence of such a region [15]. In Paper III, a homogenization temperature of 720 °C was used. An analysis of the XRD data confirms that this temperature is suitable for homogenization purposes.

Similar to the undoped compound, the amounts of Sn-rich phases decrease with increasing dwelling time for the Sn18 and Sn40 samples (Figures 15 and 16). Tiny amounts of Sn-rich phases could still be observed in the Sn40 sample regardless of treatment time (from 160 to 640 mins) like the undoped $Mg_2Si_{0.87}Sn_{0.13}$. However, in the Sn18 sample, it was only possible to reduce the amount of Sn-rich phases to a minimum (1.6 mol%) after 320 min treatment. The increase in dwelling time resulted in growth of the Sn-rich phases. It was proposed in Paper III that this occurs due to the enhanced phase separation of a single solid solution upon cooling (*cf.* Section 3.4.3). In addition, the formed microstructure is much more complex than in the case of the undoped samples, as it consists of multiple phases. This is further discussed in Section 3.4.2.2.

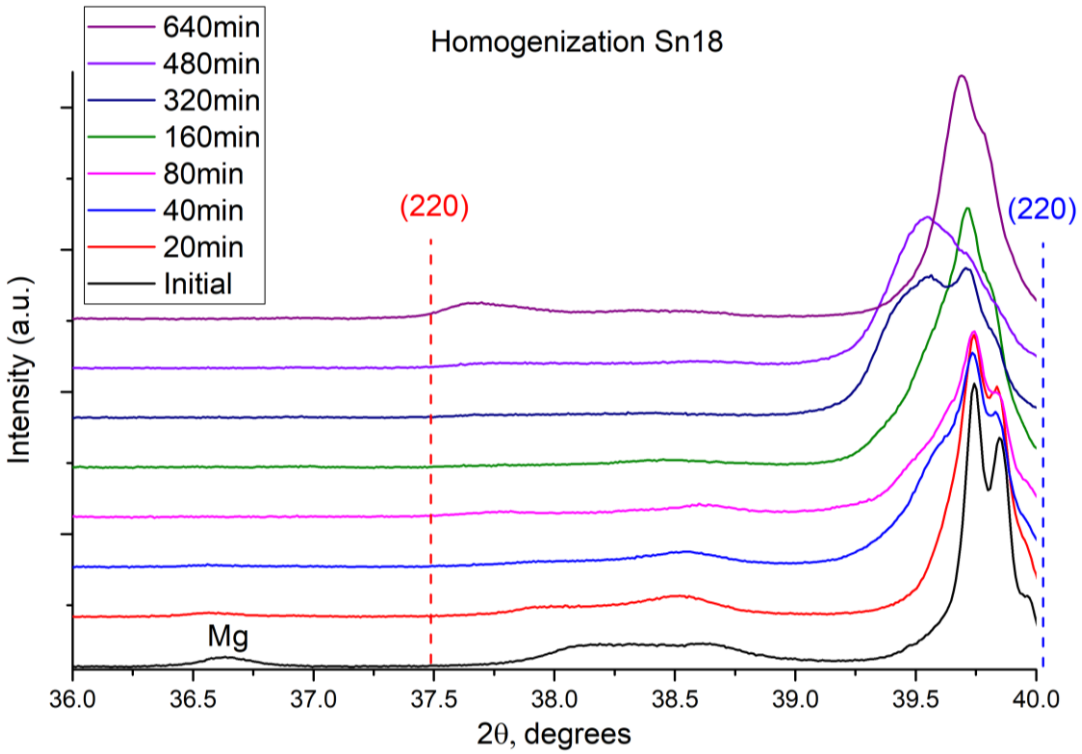

Figure 15. Homogenization of Bi-doped $Mg_2Si_{0.82}Sn_{0.18}$. XRD patterns of samples after SPS sintering at 720 during different dwelling duration. Dashed vertical lines in red and blue are reflections of pure Mg_2Sn and Mg_2Si, respectively.

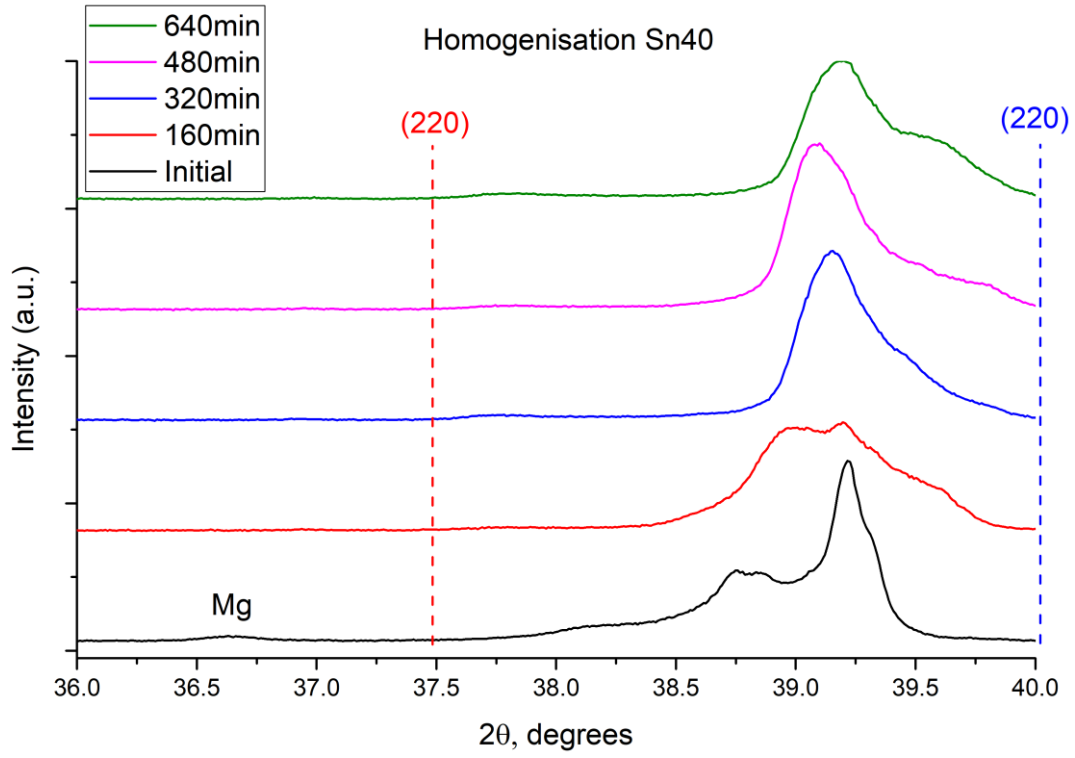

Figure 16. Homogenization of Bi-doped $Mg_2Si_{0.60}Sn_{0.40}$. XRD patterns of samples after SPS sintering at 720 during different dwelling duration. Dashed vertical lines in red and blue indicates reflections of pure Mg_2Sn and Mg_2Si, respectively.

3.3.2 Sintering

In order to employ thermoelectric materials in applications, the synthesized powders have to be sintered into a bulk form (Figure 17a). This can be achieved utilizing *e.g.,* SPS. The technique allows one to keep or create a microstructure of interest when compacting powders due to rapid heating/cooling at high pressure. Hence, the current-accelerated sintering by SPS has several benefits for the fabrication of thermoelectric devices.

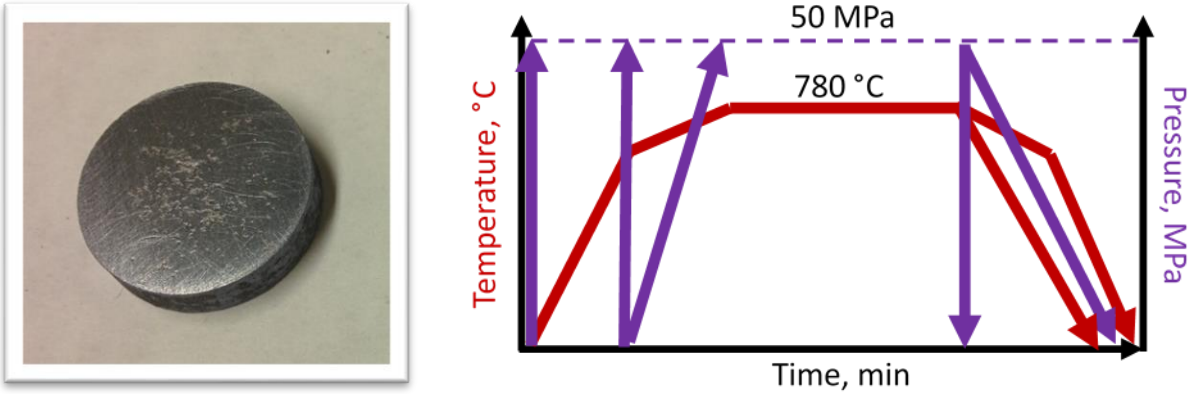

a) b)

Figure 17. The sintered pellet of a nearly single solid solution $Mg_2Si_{0.87}Sn_{0.13}$ (a) and possible SPS parameters for sintering $Mg_2Si_{1-x}Sn_x$ (b). Purple and red arrows show different strategies of rising/dropping pressure and temperature, respectively, during the SPS process.

The main SPS parameters which have to be set for sintering are: applied pressure, temperature and time, and heating/cooling rates (Figure 17b) [47]. As in the case of the synthesis described above, the choice of SPS parameters must be made taking the phase diagram into account. For instance, if the goal is to acquire a single solid solution, the dwelling temperature should lie inside the single-phase region of the phase diagram. Moreover, heating and cooling regimes have to be designed in accordance with the location of the solidus and miscibility gap, in order to avoid undesirable transformations. On the one hand, sintering temperature should be set high enough to activate the migration of atoms/molecules and voids, while on the other hand it should be as low as possible to avoid recrystallization, which could destroy the microstructure of interest. Recrystallization can also be suppressed by restricting the sintering time. Of additional concern is the applied pressure, which may at worst facilitate densification rather than recrystallization. The applied pressure may impact the strength of the final

device. Also, cracking can be avoided by precisely controlling the applied pressure. The increased thickness of sintered tablets sometimes helps to avoid cracking. However, some solid solutions are so brittle that a more careful consideration of thickness, composition as well as pressure and cooling profiles is required.

Thus, a careful selection of sintering parameters is often required to achieve the desired outcome. For instance, to sinter a single solid solution of $Mg_2Si_{0.87}Sn_{0.13}$, the temperature profile consists of rapid heating from RT to 700 °C for 6 min, dwelling for 16 min followed by rapid cooling at the maximal possible rate; the pressure, in turn, should gradually increase to 50 MPa during heating and then released to approx. 10 MPa before cooling. If the cooling rate is insufficient, $Mg_2Si_{0.87}Sn_{0.13}$ could phase-separate, since this composition enters the miscibility gap of the phase diagram at the temperature where kinetics of the system is still high. This results in phase separation either according to the mechanism of nucleation and growth, or via spinodal decomposition. Phase separation, as mentioned before, could be utilized for creating microstructures that may enhance the materials thermoelectric properties. This will be discussed in detail for $Mg_2Si_{1-x}Sn_x$ in Section 3.5.

If the $Mg_2Si_{1-x}Sn_x$ starting material consists of multiple phases, the dwelling time could be increased to ensure homogenization. In Paper III, the dwelling time was increased to 320 min for Bi-doped samples. In addition, the maximum possible cooling speed (approx. 140 °C/min during the initial stage) was proved sufficient to "freeze" the metastable single-solid solutions. So, the samples underwent phase separation. Hence, ways of increasing the cooling speed should be developed.

Synthesis of a compound directly in a SPS apparatus could be complicated for various reasons. For instance, since some materials, such as $Mg_2Si_{1-x}Sn_x$, require long time for homogenization in a single-phase region, grains could grow significantly, which is undesirable for thermoelectric performance according to the panascopic approach [10]. Nevertheless, interesting intermediate microstructures could be achieved if the homogenization is aborted before it is fully accomplished. Different diffusion rates of Si into Mg_2Sn and Sn into Mg_2Si could also be utilized for specific microstructuring.

3.4 Analysis of microstructure

3.4.1 Validation of the phase diagram Mg_2Si-Mg_2Sn

Phase diagrams play a crucial role in the synthesis as well as sintering of compounds, they open up a possibility to manipulate compositions of phases, their amounts and arrangements. Usually, a phase diagram is drawn based on calorimetry experiments. However, such an approach is not useful for the solid-state region of the Mg_2Si-Mg_2Sn phase diagram, since the transition from a single-phase region to a miscibility gap is not accompanied with a measurable change in enthalpy [16]. For this reason, the binodal lines of the system Mg_2Si-Mg_2Sn were assessed utilizing the following method (*cf.* Paper II).

A series of experiments were designed to cover possible positions of the single-phase region and miscibility gap. The approach consisted of homogenizing mixtures of Mg_2Si and Mg_2Sn in different molar proportions in the single-phase region (black circles in Figure 14a), allowing them to come into thermodynamic equilibrium at lower temperatures (black squares in Figure 14a) and comparing the difference in compositions of acquired phases. For instance, if the acquired phases display the same compositions after annealing at different temperatures, then the samples with the same nominal composition were treated in a single-phase region. Moreover, when samples are treated in the miscibility gap, compositions of the constituent phases should correspond to the compositions defined by binodal lines. Here, quenching would be preferred in order to obtain a more detailed shape of the binodal lines (the effect of cooling rates is demonstrated in Section 3.4.3). However, if diffusion kinetics of the system is relatively low at some temperatures, slower cooling could also be utilized to determine the binodal lines.

After the treatment of $Mg_2Si_{1-x}Sn_x$ with x = 0.03, 0.06, 0.08, 0.13 and 0.18 in a tubular furnace, the samples were characterized with XRD and analyzed utilizing the Rietveld method. The compositions of the constituent phases of each sample are presented in Tables 1 and 2 of Paper II. As it can be seen from the tables, the sample with the nominal composition x = 0.03 (in the compound $Mg_2Si_{1-x}Sn_x$) possesses two Si-rich phases with compositions, which do not change after the treatment after 680 and 580 °C, respectively. The same statement is valid for the sample with x = 0.06. Since no difference in the composition of phases is observed after treating the compounds at different temperatures, and furthermore since no Sn-rich phases appear, one can

suggest that the samples with x = 0.03 and x = 0.06 were treated in the single-phase region. The formation of two Si-rich phases is a result of spinodal decomposition, which will be discussed in detail in Section 3.4.4. Increasing x to 0.08, the samples decompose differently, depending on the treatment temperature. The sample treated at 680 °C still forms two Si-rich phases similarly to the samples with $x \leq 0.06$ (the second Si-rich is barely visible and could not be accounted for utilizing Rietveld refinement). Hence, the sample with x = 0.08 at 680 °C must also have been treated in the single-phase region. When reducing the treatment temperature to 580 °C, an Sn-rich phase can be found, showing that the sample was treated in the miscibility gap. This means that the binodal line of the Si-rich region of the phase diagram Mg_2Si-Mg_2Sn passes between 580 and 680 °C at X(Sn) = 0.08.

Unlike the samples discussed above, the samples with higher Sn content, *i.e.* $Mg_2Si_{0.87}Sn_{0.13}$ and $Mg_2Si_{0.82}Sn_{0.18}$, decompose at both 680 and 580 °C. The samples with the overall composition $Mg_2Si_{1-x}Sn_x$ with x [0.08:0.18] treated at 580 °C have the same composition of Sn-rich phase, *i.e.* approximately $Mg_2Si_{0.33}Sn_{0.67}$, and its amount increases with increasing x. Such behavior is characteristic to the alloys treated in a miscibility gap and strengthen the hypothesis that the binodal line is above 580 °C for x [0.08:0.18]. The samples with the nominal compositions x = 0.13 and x = 0.18 treated at 680 °C form Sn-rich phases with different compositions, which allows us to suggest that the sample with x = 0.13 was treated in the single-phase region and the sample with x = 0.18 in the miscibility gap. Regardless the fact that the sample with x = 0.13 was treated in the single-phase region, it forms an Sn-rich phase due to the utilized slow cooling rate and comparably high temperature at the transition point to the miscibility gap. Hence, the atoms are mobile during a sufficient period, so that they can diffuse and form nuclei of an Sn-rich phase. Thus, the binodal curve passes the temperature 680 °C between X(Sn) = 0.13 and X(Sn) = 0.18.

The phases that were formed in the samples treated in the miscibility gap were plotted above the available phase diagrams in Figure 18. As can be seen from the figure, the experimental results of the current work are in agreement with the binodal line in the Si-rich region, which was theoretically calculated by Viennois et al. [14]. However, the results do not follow any of the suggested binodal lines in the Sn-rich region [11-15]. Moreover, the compositions of the Sn-rich phases formed in the samples treated in the miscibility gap at 580 and 680 °C, respectively, violate the expectation of the increase of the solubility limit of Si in the Sn-rich phase. This abnormal behavior could be the result of a pinning effect provided by particle and grain boundaries. This effect could

hinder the phase separation at lower temperatures, where the mobility of atoms is not sufficient to overcome the energetic barrier.

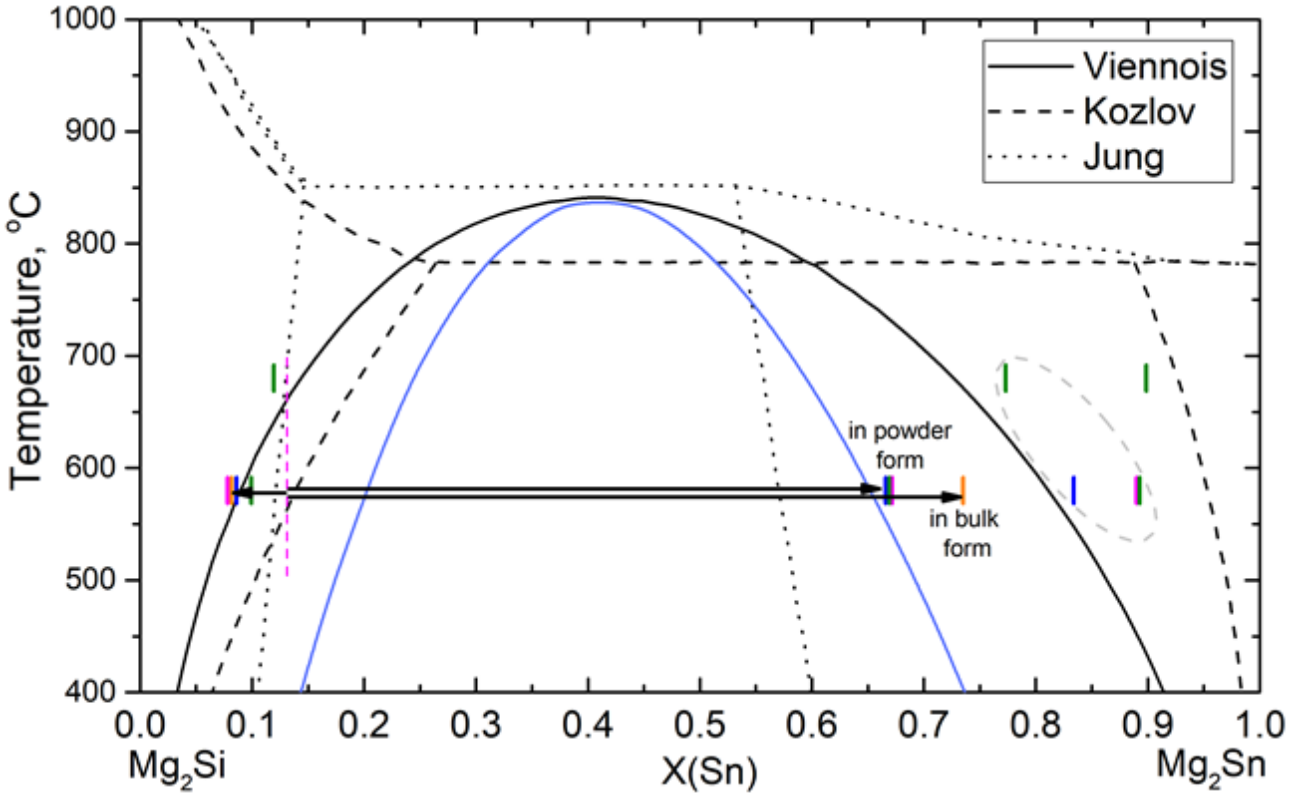

Figure 18. Available phase diagrams [11-14] of Mg_2Si-Mg_2Sn and formed phases in the samples of the current work, which were treated inside the miscibility gap: $Mg_2Si_{0.92}Sn_{0.08}$ (blue), $Mg_2Si_{0.87}Sn_{0.13}$ (magenta), $Mg_2Si_{0.82}Sn_{0.18}$ (green); the bulk sample $Mg_2Si_{0.87}Sn_{0.13}$ is shown in orange. Blue solid curve shows approximate shape of the spinodal region according to Viennois et al. [14]. Grey dashed oval encloses secondary Sn-rich phases of a minor quantity. Magenta dashed vertical line represents starting point for two samples of composition $Mg_2Si_{0.87}Sn_{0.13}$ in bulk and powder state, which formed Si-rich phases of same compositions, but Sn-rich phases of different compositions.

Another inconsistency was also found when performing phase separation of the nearly single solid solution $Mg_2Si_{0.87}Sn_{0.13}$ sintered in SPS. This sample, in bulk form, treated in the same way as the powder sample (tubular furnace, homogenization at 780 °C + annealing at 580 °C), also decomposed into Si- and Sn-rich phases, however the Sn-rich phase contained less silicon by approximately 7 at% than the Sn-rich phase formed in the powder sample (Figure 18). This result still disagrees with the suggested binodal lines in the Sn-rich region [11-15]. Pinning effect could also explain this deviation, since

the density of boundaries is less in the bulk sample, therefore this effect has a lower influence in the bulk sample.

Nevertheless, an approximate position of the binodal curve in the Si-rich region was determined, which opens up the possibility of manipulating the microstructure of Si-rich $Mg_2Si_{1-x}Sn_x$ alloys. In addition, more experiments with Sn-rich samples are required in order to determine the position of the binodal line in the Sn-rich region.

3.4.2 When phase diagrams fail

Phase diagrams show equilibrium state compounds. However, there are other factors which influence the final microstructure of materials, and hence their physical properties. One of these factors is the pinning effect of grain boundaries, which was discussed in the previous section. It was demonstrated [62] that some doping elements are able to stabilize or destabilize $Mg_2Si_{1-x}Sn_x$ solid solutions. A suppression of the miscibility gap is possible due to the strain effect, which appears after long mechanical milling of compounds [65]. Moreover, an excess or deficiency of Mg from the stoichiometric amount changes the final microstructure. Thus, more complex phase diagrams are required in order to predict results. In addition, the strain between grains of the formed phases could affect their composition. And instead of phases with composition described by the binodal line, the so-called intermediate phases are formed. Some of these factors are described in this section in more detail.

3.4.2.1 Effect of Mg on the microstructure

As reported by Yasseri et al. [15] and Orenstein et al. [66], a liquid phase Mg-Sn should exist above 600 °C in the $Mg_2Si_{1-x}Sn_x$ with Mg excess. This liquid phase infiltrates grains and provides fast delivery of Mg and Sn atoms to Mg_2X phases. It is important to account for this phase, as it influences the final microstructure. To better understand the phase behavior of $Mg_2Si_{1-x}Sn_x$, a ternary phase diagram can be utilized (Figure 19b).

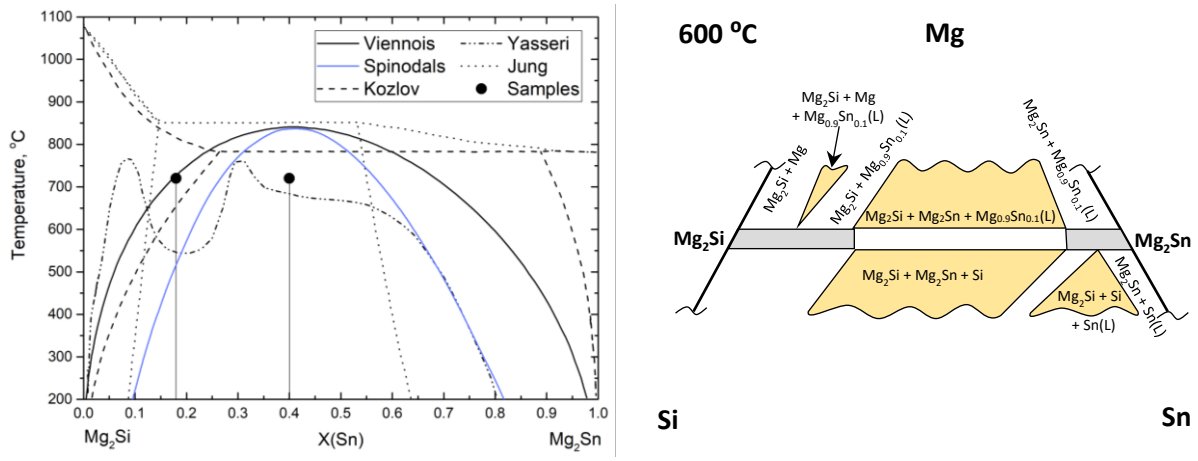

a) b)

Figure 19. Existing phase diagrams and position of sample compositions and treatment temperature for study in Paper III: a) pseudo-binary phase diagrams [11-15]; b) a part of ternary phase diagram Mg–Si–Sn at 600 °C [66].

When the Mg content is in excess of the stoichiometric amount (area above the pseudo-binary cut Mg_2Si-Mg_2Sn in Figure 19), the liquid $Mg_{0.9}Sn_{0.1}$ phase coexists with Si-rich and Sn-rich phases above 565 °C. With the increase in dwelling time, researchers [63,67] suggest that Mg evaporates, and only free Sn remains.

Alternatively, the presence of free Sn was reported by Goyal et al. [63], who argue that liquid Sn appears in $Mg_2Si_{0.3}Sn_{0.7}$ due to decomposition of liquid Sn-rich phase, which exists above 900 K. They suggest that such decomposition provides extra Mg, which compensates for the Mg loss, thus acting as a self-healing mechanism. In Paper II and Paper III, the free Sn phase was also observed on the XRD diffraction patterns.

In Paper III, both compositions Sn18 and Sn40 formed the free Sn phase after certain amount of time at 720 °C. It was found that 0.5 % of the Sn phase was traceable in the Sn18 sample after 640 min. The phase was formed much earlier than observed by Yasseri et al. [15]. However, this is consistent with the experiments by Goyal et al. [63], which observed this phase after 600 min at 700 °C. Free Sn was found in the Sn40 sample even after shorter treatment – 320 °C. Its amount varied with the further increase in dwelling time: 0.2 mol% after 320 min, almost zero mol% after 480 min and 0.3 mol% after 640 min. This finding is not consistent with the logic that the amount of Sn should increase with the increase in dwelling time since the amount of Mg reduces. This unless the free Sn phase or Mg-Sn liquid phase, or Sn-rich liquid phase – depending on the interpretation – is driven out from the sample during treatment.

After sintering, small droplets appeared on the SPS dies. The EDX analysis of Sn18 and Sn40 samples revealed that the droplets contained a significant amount of Mg and O in every droplet with an atomic proportion approx. 1:2. There was also 1 at% of Bi, 0.2 at% of Si. The amount of Sn in the droplets from the Sn40 sample was greater than in the Sn18 sample, *i.e.* 5.5 at% and 3.1 at%. This was also confirmed by the Sn balance of the phases present in the Sn40 samples – this set of samples lost Sn with the increase in dwelling time (41 at% in the initial samples; 32, 31 and 28 at% in the samples treated for 320, 480 and 640 min, respectively). The proportion of Sn to Mg in the Sn18 samples was close to 1:9, which is in line with the proposed liquid $Mg_{0.9}Sn_{0.1}$ phase by Orenstein et al.[66] Assuming that the Sn40 sample should also contain this liquid phase, a greater concentration of Sn in the Sn40 sample suggests that either the sample loses pure Sn or a compound similar to Mg_2Sn.

When the amount of Mg in Mg_2X is below the stoichiometric amount, free Si phase should appear according to Figure 19b. While there was no free Si phase in the samples of Paper III, suggesting that the amount of Mg stayed above stoichiometric in all of the samples, the samples in Paper II contained a significant amount of free Si – up to 9.2 mol%. The presence of the free Si phase implies that a long treatment of samples – homogenization at 780 ºC for 600 min and, secondly, annealing either at 680 ºC for 1200 min or at 580 ºC for 2400 min – leads to a Mg deficiency situation. Free Sn phase was also observed in the samples in Paper II, which could appear due to the presence of extra Mg, which was added in the beginning to compensate for the Mg loss during treatment. However, interestingly, the Sn phase was present in the majority of the samples, but not in all of them. The experiments were carried out in crucibles, and Sn could not leak out from there as occurred in an SPS die.

3.4.2.2 Effect of Bi on the microstructure

The main purpose of applying dopants in thermoelectric materials is to shift the concentration of charge carriers and adjust the band structure. Elements with a higher valence than Si or Sn, such as Sb and Bi, provide extra valence electrons enhancing N-type semiconductor properties of magnesium silicide-stannide alloys. Conversely, the elements of lower valence like Ga and In create holes at some energetic levels, turning the system into a P-type semiconductor. Since both the Seebeck coefficient and electrical conductivity depend on the charge carrier concentration, the amount of the utilized dopant has to be optimized. Moreover, when choosing a dopant, the solubility limit of the dopant in the matrix material has to be taken into consideration to ensure

homogeneity. According to literature, up to 3 mol% of Bi could be utilized in $Mg_2Si_{1-x}Sn_x$ [54]. In Paper III, 2.5 mol% of Bi was added for optimization of charge carrier concentration.

In addition, dopant atoms distort the matrix lattice, which provides conditions for scattering of high frequency phonons. This in turn reduces lattice thermal conductivity, which is beneficial for improving the thermoelectric performance.

Some dopants improve the stability of single solid solutions, while others enhance the phase separation [62]. It has been reported that Bi is responsible for the decomposition of $Mg_2Si_{1-x}Sn_x$ on cooling [59, 62, 68]. It was also found in Paper III that Bi-doped Sn18 and Sn40 samples formed complex microstructures on cooling. Multiple Si-rich and Sn-rich phases were found utilizing XRD (Figure 20). These samples were naturally cooled in the SPS apparatus with the initial cooling rate of ~140 °C/min. In order to produce a single solid solution, if necessary, higher cooling rates should therefore be applied. Alternatively, other dopants could be utilized.

Although Bi enhances phase separation, the microstructure of samples Sn18 and Sn40 appears to become more complex than expected according to the existing phase diagrams present in the literature.

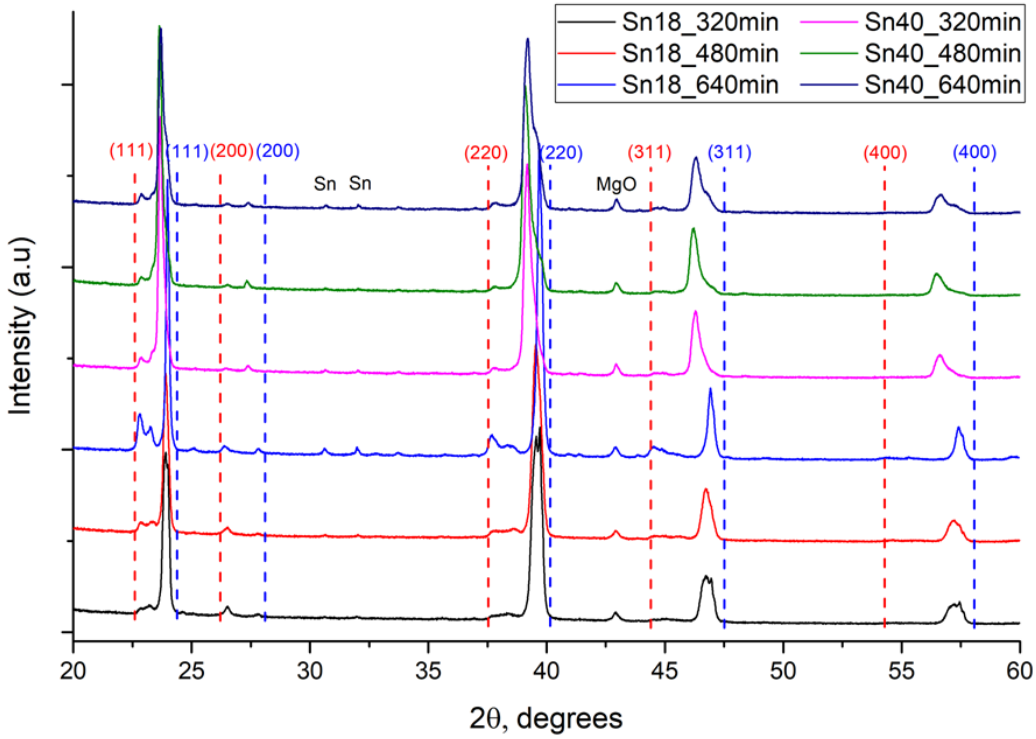

Figure 20. XRD patterns of $Mg_2(Si_{0.82}Sn_{0.18})_{0.975}Bi_{0.025}$ and $Mg_2(Si_{0.6}Sn_{0.4})_{0.975}Bi_{0.025}$ after SPS sintering at 720 °C during different dwelling time.

3.4.2.3 Intermediate phases in Bi-doped $Mg_2Si_{1-x}Sn_x$

The current phase diagrams [11-15] suggest that $Mg_2Si_{1-x}Sn_x$ should be split into two separate phases in the miscibility gap: that is Sn-rich- and Si-rich phases respectively, with compositions defined by the binodal lines. Alternatively, a spinodal decomposition could occur resulting in the formation of two phases with similar compositions. In Paper II and Paper III, it was observed that both mechanisms are involved in creating the microstructure of the samples. As for Paper II, the experiments here follow the suggested phase diagram by Viennois et al. [14], with some fine distinctions for the Sn-rich region. Using XRD, it was possible to see either two or three phases of same type Mg_2X. The appearance of a second Sn-rich phase could be explained by additional phase separation on cooling of the samples treated in the miscibility gap. However, the microstructure of the samples in Paper III is much more complex than could be predicted utilizing the available phase diagrams. Thus, up to seven phases of the anti-fluorite type Mg_2X were refined (Figure 21).

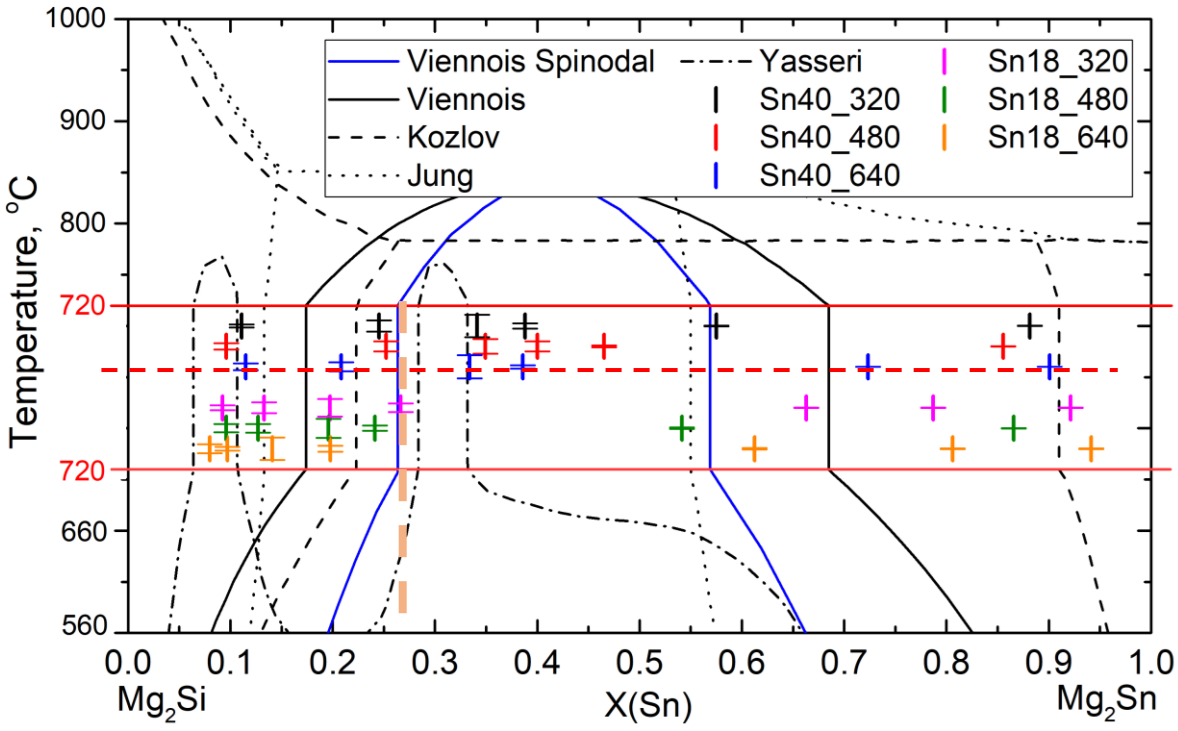

Figure 21. $Mg_2(Si_{1-x}Sn_x)_{0.975}Bi_{0.025}$ phases in the $Mg_2(Si_{0.82}Sn_{0.18})_{0.975}Bi_{0.025}$ and $Mg_{2.2}(Si_{0.6}Sn_{0.4})_{0.975}Bi_{0.025}$ samples after homogenization at 720 °C in SPS.

Physical metallurgy suggests an explanation of such a complex behavior. Though the chemical potential drives the phases toward equilibrium, strain energy between phases can hinder it. Another aspect, which may influence an outcome, is limited diffusion kinetics of Si and Sn atoms. Moreover, the diffusion kinetics of Si and Sn is different,

which also plays a role in the final microstructure. All these factors potentially create conditions for the formation of intermediate phases [69-71]. The strain energy can be minimized when phases with lower interfacial mismatch are formed. Such nearly endotaxial interfaces can be formed if the phases are of the same type (or possess mutually matching crystal lattices) and the difference of the lattice parameters is small. Hence, a set of solid solutions with similar composition can be formed. And this is the case in the samples Sn18 and Sn40, where a set of Si-rich and Sn-rich phases was observed. In addition, a certain shape of the phases may also minimize the energy, *e.g.* spherical, etc. This scenario leads to the formation of a phase with a composition different from the expected one.

During homogenization, Sn-rich phases in the Sn18 samples almost disappear after 320 min treatment at 720 ºC. However, they grow after longer treatment. Such behavior was not observed in the Sn40 samples. Instead, the amount of Sn-rich phases stays almost constant from 160 to 640 min of homogenization and in minor quantities. In addition, the Sn40 samples consist of a set of Si-rich phases with a wide distribution in their compositions – x (0.1 – 0.6) in $Mg_2Si_{1-x}Sn_x$. In contrast, the distribution of Si-rich phases in the Sn18 samples typically varies around x (0.1 – 0.25) in $Mg_2Si_{1-x}Sn_x$. Thus, as for the Sn40 samples, the formation of Si-rich phases with a high concentration of Si and the minor quantities of Sn-rich phases is not expected following the behavior of solid solutions cooled through the miscibility gap. And the theory regarding the intermediate phases could be one of the factors involved, which yields in such microstructure. Arguably, less energy is required for such a transition. This is the first attempt, to the author's knowledge, to couple the theory of intermediate phases with the Mg_2Si-Mg_2Sn system.

3.4.3 Ways to achieve fine microstructure

According to the panascopic approach [10], the thermoelectric efficiency can be improved via doping, presence of foreign phases as well as via grain size control.

Dopant atoms distort the matrix lattice, which provide conditions for scattering high frequency phonons. Here, it is important to ensure that dopant atoms are fully incorporated into the material matrix. This can be achieved via comminution of constituents, as well as by increasing the homogenization time. For instance, in Paper III, the XRD patterns showed that some of the Bi-dopped samples contained a small amount of Mg_3Bi_2, which signified the need of further homogenization.

Foreign phases can either be embedded into the compound or be formed during the phase separation. In the later case, endotaxial precipitations are favorable, since they are characterized with nearly-coherent interphases, which do not significantly hinder the ability of electrons to transfer from one phase or grain to another. Magnesium silicide-stannide alloys are able to decompose into two or more phases of the same type, *i.e.* $Mg_2Si_{1-x}Sn_x$, due to the presence of a miscibility gap [11-15] and as demonstrated in Paper II and Paper III. The same crystal lattice, with slightly different lattice parameters of the phases, creates conditions for the formation of nearly-coherent interphases, since the relative strain between the Si- and Sn-rich phases is less than 6%. Such matching of the lattices normally leaves electron transport almost unaffected, while the phonons are scattered due to fluctuation of atomic masses (alternation of Si and Sn). The electron transport can be assessed via the charge carriers' mobility parameter, which could be either measured utilizing Hall effect [72] or be calculated from the Seebeck coefficient and electrical conductivity. The weighted electron mobility was calculated for the samples in Paper III (Figure 22). The Sn18 samples treated for 480 minutes exhibit the best mobility among other samples. However, all Sn18 samples prove to lose in terms of thermal conductivity and Seebeck coefficient as compared to the samples with composition Sn40 (*cf.* Section 3.5). But the sample Sn40_320 turned out to be the best-performing among the Sn40 samples due to the higher weighted mobility parameter.

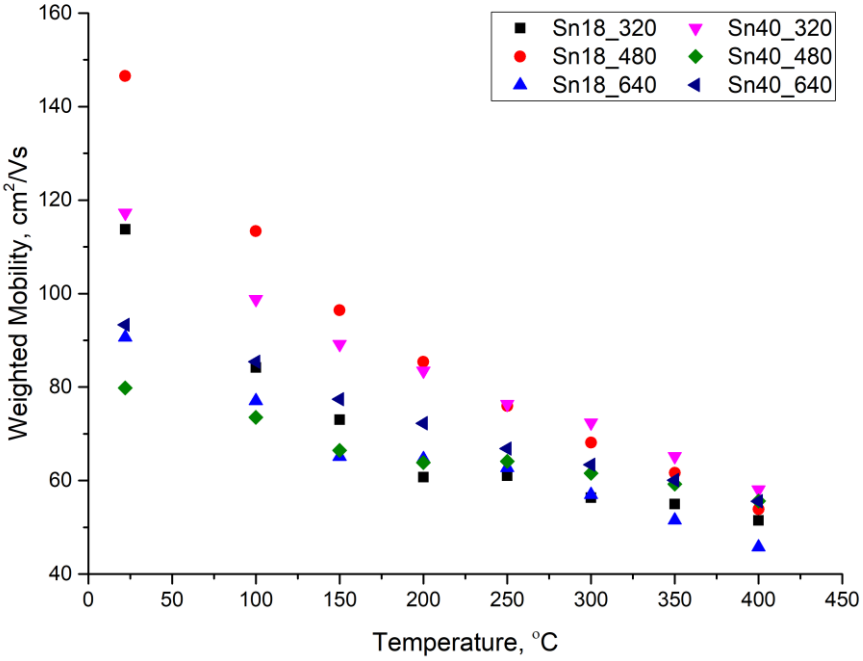

Figure 22. Weighted mobility of Sn18 and Sn40 in Paper III according to Snyder et al. [73].

The precipitations can be formed when treating a solid solution in a miscibility gap. For example, a nearly single solid solution of $Mg_2Si_{0.87}Sn_{0.13}$ homogenized in the single-phase region decomposes into Si- and Sn-rich phases during treatment at 580 °C (Figure 23a). In Figure 23a, one can observe the appeared reflections of the Sn-rich phase, which do not grow after 1200 min – meaning that equilibrium was achieved. By varying the annealing time and temperature, it is possible to control the microstructure, *e.g.* to form the nuclei of an Sn-rich phase with different compositions and to grow these precipitations to a certain diameter. The suggested temperature for annealing accrues from the determined binodal line of the Si-rich region (Section 3.4.1) and ranges around 400–700 °C depending on the Sn/Si ratio, on the dopants as well as on utilized phase diagrams. The treatment time will depend on the annealing temperature, composition and the desired outcome.

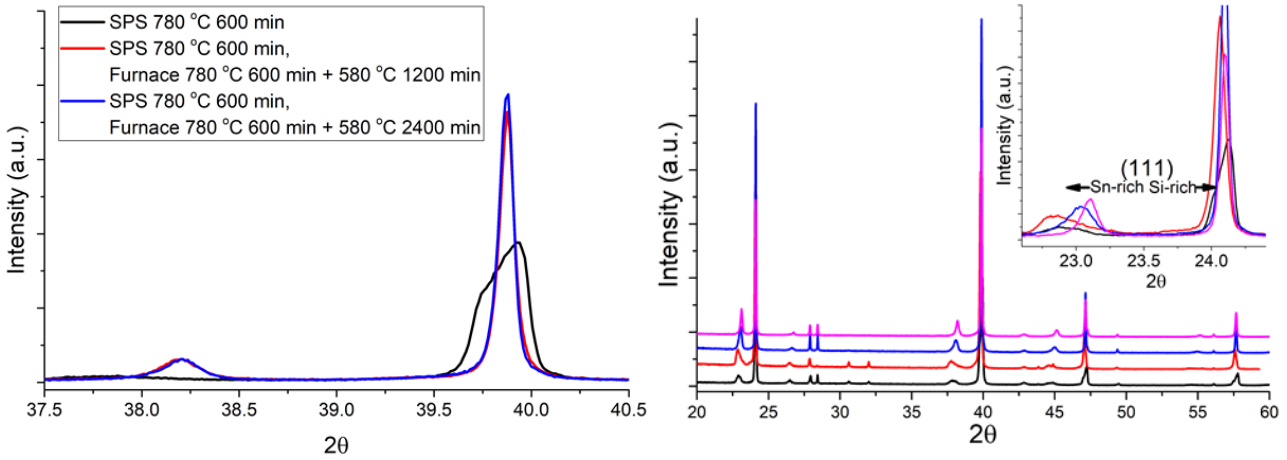

Figure 23. XRD patterns for $Mg_2Si_{0.87}Sn_{0.13}$: a) phase separation during treatment at 580 °C (reflection 220); (b) experiencing different cooling rates: quick cooling (black), slow linear cooling to 400 °C (red), slow exponential to RT (blue) and slow exponential from 580 °C to RT (magenta).

Alternatively, microstructure control can be performed via different cooling regimes. In Figure 23b one can observe that the reflections corresponding to the Sn-rich phase display different shapes, heights and positions depending on the type of cooling chosen. Hence, the composition, size of precipitations as well as their arrangement will differ. The most beneficial microstructure for thermoelectric application should be investigated by measuring thermoelectric properties (Section 3.5).

An interesting combination of endotaxial phases can be obtained, for instance, via partial homogenization of the mixture of Mg_2Si and Mg_2Sn (blue pattern in Figure 14b).

In this case, the formed junctions from Mg_2Si to Mg_2Sn phases could create conditions for enhanced phonon scattering. Different diffusion rates of Si into Mg_2Sn and of Sn into Mg_2Si lattices could also contribute positively. The gradient concentration materials, as another example, could furthermore be a promising way of maintaining the best thermoelectric performance throughout the entire length of a thermoelectric leg. Thus, the thermoelectric leg composition could start with Si-rich phases, which have a significantly negative Seebeck coefficient, and gradually change to the Sn-rich phases with a reduced Seebeck coefficient. This outcome can be achieved either by SPS while sintering the thin layers of $Mg_2Si_{1-x}Sn_x$ with x changing from approximately 0 to 1 with a step of approximately 0.1. Alternatively, the synthesis of the gradient compound can be carried out in a gradient solidification vertical furnace. While SPS sintering is performed in solid state, the last implies melting of the magnesium silicide-stannide alloy and its further treatment in the region between the solidus and liquidus lines. In the presence of a temperature gradient, which slowly shifts towards lower temperatures, Si-rich solid solutions will start crystallizing first, while Sn-rich phase will remains in the liquid form. Continuing decreasing the temperature, materials with a gradient concentration of Sn-Si will be produced.

In addition, a very complex and unusual microstructure was achieved in the context of Paper III. The homogenized solid solutions decomposed into up to seven phases of the same type Mg_2X on cooling. Both signs of spinodal phase separation and of phase separation via nucleation and growth were present in the samples. The reasons of such a complex phase separation are discussed in Paper III and throughout Section 3.4.

The last concept of the panascopic approach involves a grain boundary control. Since the grain boundaries are characterized by a high density of dislocations, high frequency phonons tend to scatter upon encountering such imperfections. Moreover, if a size of grains is small enough, *e.g.* below approximately 100 nm, the grains themselves will screen low frequency phonons (similar to the precipitations). To approach such small grain size, the compound should be milled finely or produced within a form of nano-crystals in a solution, or from the precursors during a solid-state reaction while sintering. Another promising way of producing nano-powders, is via rapid solidification of droplets from the melt salts. While sintering nano-powders the sintering temperature and time could be set much lower than when sintering micrometer powders. This could also be beneficial for the enhancement of thermoelectric properties.

3.4.4 Ways to achieve spinodal decomposition

In the presence of a miscibility gap, magnesium silicide-stannide alloys can experience spinodal decomposition. The microstructure formed due to spinodal decomposition is of a particular interest for thermoelectric applications, since it is characterized with constantly alternating endotaxial lamellae-like Si- and Sn-rich phases. The alternation of these phases is at the nano-meter length scale, which in turn is beneficial for effective reduction of the lattice thermal conductivity. There are a couple of ways to achieve such fine microstructure.

A $Mg_2Si_{1-x}Sn_x$ solid solution in a single-phase region has to be rapidly cooled to pass a binodal region (Figure 18) quickly. If the solid solution is cooled to a certain temperature, at which the kinetics of the solid solution is sufficient to allow atoms diffusing over long distances, the solid solution will phase-separate. Since the binodal region is passed (the solid solution is located in the spinodal region), the phase separation will proceed in the spinodal way. Compositions of the formed Si- and Sn-rich phases are defined by the binodal lines. To limit the split of the phases towards the compositions defined by binodal lines, a certain cooling rate should be applied. This will result either in the formation of two phases with similar compositions, or in a partial formation of Si- and Sn-rich phases. Thus, in Figure 23b, it is possible to see that the quickly-cooled $Mg_2Si_{0.87}Sn_{0.13}$ (black curve) has two reflections corresponding to two Si-rich phases with similar compositions ($Mg_2Si_{0.94}Sn_{0.06}$ and $Mg_2Si_{0.89}Sn_{0.11}$). A a minor amount of Sn-rich phase is also formed. Other samples presented in Figure 23b were cooled utilizing lower cooling rates, hence they did not experience the same type of decomposition. Instead, the phase separation followed a route of nucleation and growth.

The grain boundaries or impurities could influence spinodal decomposition. Since the grains grow with time when homogenizing a solid solution, the density of grain boundaries decreases. This, in turn, reduces the pinning effect, so that the spinodal decomposition occurs more rapidly [62]. Such phenomena can be observed when treating $Mg_2Si_{0.87}Sn_{0.13}$ at 780 °C for 180 and 600 min, respectively. The sample treated for 180 min shows a single Bragg peak corresponding to a single Si-rich phase (Figure 24a). This peak splits into two when $Mg_2Si_{0.87}Sn_{0.13}$ is treated for 600 min, so that two Si-rich phases with similar compositions are formed.

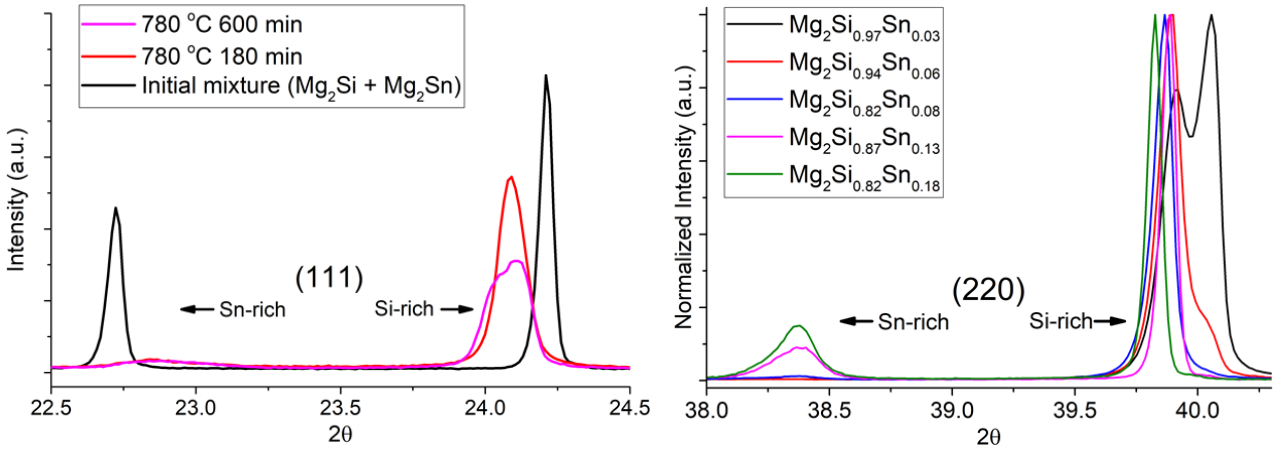

Figure 24. XRD patterns: a) spinodal decomposition in $Mg_2Si_{0.87}Sn_{0.13}$ during homogenization in the single-phase region (reflection 111); b) annealing of $Mg_2Si_{1-x}Sn_x$ with x<0.18 at 580 °C (reflection 220).

Alternatively, if the transition from a single-phase region to a binodal region occurs at a temperature, which is too low for atoms to diffuse long distances to form nuclei of another phase, the phase separation will also proceed in spinodal fashion. This was observed for the slowly cooled samples $Mg_2Si_{1-x}Sn_x$ with $x < 0.08$. In Figure 24b, one may note that that after the treatment of the solid solutions at 580 °C only the samples with $x < 0.08$ have two reflections corresponding to two Si-rich phases with similar compositions. According to the phase diagram in Figure 18, the transition to the binodal region for these samples occurs at lower temperatures than for the samples with higher Sn-content.

3.5 Microstructure and thermoelectric properties

In order to determine the dimensionless figure of merit, zT (*cf.* Equation 2 and Figure 26d), the thermal conductivity (Section 2.2.3, 2.2.4 and Figure 26a), electrical resistivity (Section 2.2.2 and Figure 26b) as well as Seebeck coefficient (Section 2.2.1 and Figure 26c) have first to be measured. For this, the sintered samples Sn18 and Sn40 in Paper III were cut into rods (4x4x7 mm^3). The thermoelectric properties were then obtained along the rod length. The upper temperature limit was restricted to 400 ºC due to the presence of the miscibility gap in the Mg_2Si–Mg_2Sn system, which as noted earlier affects the microstructure of the samples. The electrical conductivity and Seebeck coefficient were measured utilizing a ZEM-3 instrument (Model M10 by Ulvac-Riko, inc.) in 0.15 bar atmosphere of He. The thermal conductivity was calculated from the measured thermal effusivity (Section 2.2.4.4 and Figure 25b) and measured heat

capacity (Section 2.2.4.5 and Figure 25a) with the thermal constants analyser TPS3500 model (manufactured by Hot Disk AB, Sweden) in the atmosphere of N_2.

The measurements revealed that the Sn18 and Sn40 samples treated at 720 ºC during different periods of time possess different thermoelectric properties. The variations can be explained by the discrete microstructures formed during the treatment as confirmed by the X-ray diffraction (Section 3.4.2.2) and Rietveld refinement (Section 3.4.2.3).

The Sn40 samples exhibit the lowest thermal conductivity values compared to the Sn18 samples. Reduction of thermal conductivity of the samples with the ratio Sn/Si close to 1 is expected due to the alloying effect. Perhaps a specific microstructure also affects the thermal conductivity, since reduction of Sn in the Sn40 samples with the increase in dwelling time has negligible effect on the thermal conductivity. The Sn18_640 sample has the lowest thermal conductivity among the samples of same composition, perhaps due to the presence of Sn-rich clusters. These scatter phonons of certain wavelengths and hinder electron transport, and, hence reduce the thermal conductivity [10, 53].

The Sn40_320 sample shows almost as high weighted mobility (Figure 22) as the Sn18_480 sample, which suggests a low density of point defects, and thus increased electrical conductivity [73, 74]. However, the Sn18_480 sample has a lower Seebeck coefficient compared to the Sn40_320 sample. The advantage as regards the Seebeck coefficient is present for all Sn40 samples compared to the Sn18 samples. Adding to the equation the overall low thermal conductivity of the Sn40 samples results in the higher zT values than Sn18 samples possess.

Among the Sn40 samples, the Sn40_320 sample exhibits the highest zT values over the entire temperature range due to balanced electrical resistivity and Seebeck coefficient. The highest achieved zT value is 0.47 at 300 ºC for the sample Sn40_320. Further increase in temperature reduces zT of this sample much more than for other samples, perhaps due to some simultaneous structural change.

The Sn18_640 sample has the highest zT value among the Sn18 sample at 0.25 due to low thermal conductivity and balanced electrical resistivity and Seebeck coefficient.

A relatively low figure of merit regarding the samples of the current work is due to a high electrical resistivity as compared to other works [53, 75-77]. The likely cause is

large amount of MgO, which is an undesirable inclusion in $Mg_2Si_{1-x}Sn_x$ solid solutions [56].

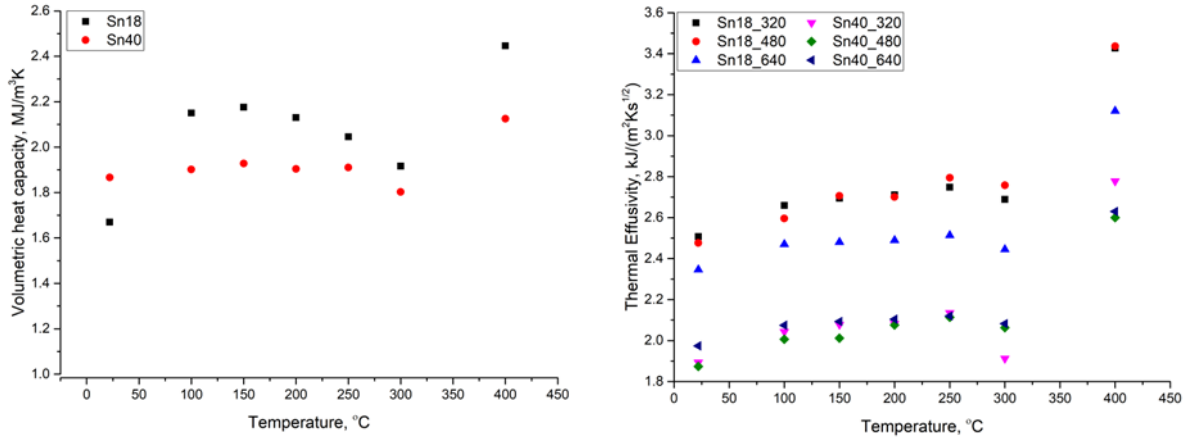

a) b)

Figure 25. Heat capacity per unit volume (a) and thermal effusivity (b) obtained by Hot Disk methods.

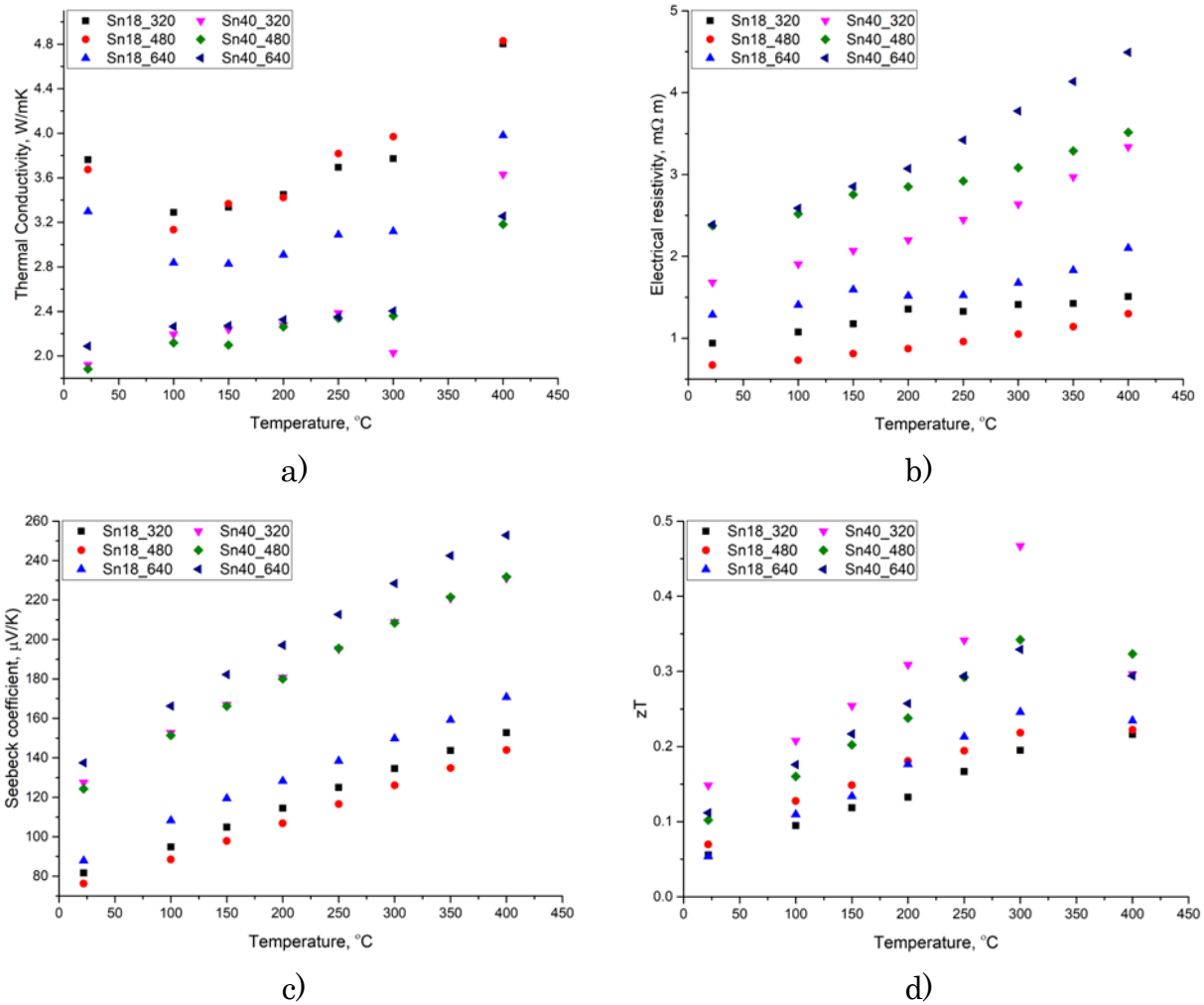

a) b)

c) d)

Figure 26. Basic thermoelectric properties: a) thermal conductivity; b) electrical resistivity; c) Seebeck coefficient; d) dimensionless figure of merit zT.

Chapter 4

Inhomogeneous materials testing with the structural probe technique

4.1 Quality control and hot disc

When manufacturing composite materials homogeneity often plays a crucial role, since the properties of materials have to be maintained constant throughout the volume. Unexpected inhomogeneity may cause reduced performance, or even failure, of a produced device. Inhomogeneity in thermoelectric materials is therefore of value and interest to study.

When sintering larger pieces of a material by SPS, a considerable temperature gradient may develop between the center and the periphery of the sample. This in turn may lead not only to a microstructural variation in the sample, but also to variations in chemical composition throughout the sample [16]. It was found by XRD and SEM studies that the magnesium silicide-stannide single solid solution decomposes during sintering into four distinct phases of type $Mg_2Si_{1-x}Sn_x$. Simulation of the sintering process showed that there exists a temperature difference of 25 K within a sample with a diameter of 20 mm and a height of 5.5 mm. Since the sintering was carried out in the miscibility gap, the temperature gradient resulted in the formation of a set of different alloys following the binodal curve of Si-rich and Sn-rich regions in the binary phase diagram. Moreover,

investigating different parts of the sample, the amounts and compositions of the constituent phases varied. Thus, to achieve viable results it is important to utilize non-destructive Quality Control (QC) testing in order to keep track of undesired material transformations.

A material property, which is able to indicate the quality of a device, is the thermal conductivity. In this study, the hot disc method is considered as a QC tool, since it offers high sensitivity and reproducibility in estimations of thermal conductivity. In addition, the technique offers direct control of the thermal depth of probing, *i.e.* allowing precise control of the region of material being tested.

The original hot disc technique estimates a single value of thermal conductivity from an experiment. By using the original hot disc technique, the inhomogeneity problem can be tackled in several ways. For instance, the experiments are performed with the hot disc probe positioned at different spatial positions on the device surface [78]. Alternatively, the probe is kept in the same position, but the thermal depth of probing is varied with measurement time. In both cases, the recorded mean thermal conductivity values will be different if the material is inhomogeneous. But, since the thermal probing depth can be controlled via the measurement time, would it be possible to employ the existing technology to receive a function of the thermal conductivity vs. depth from a single experiment? This would render often crucial information on possible inhomogeneity. Also, this could be a valuable tool for assessing materials with built-in structural gradients, *e.g.* devices with a gradient concentration.

Thus, this chapter summarizes the recent development of the so-called Structural Probe (SP) technique, a modification of the standard hot disc methodology for this specific purpose. In addition, the method's main assumptions, performance range, sensitivity and drawbacks are reviewed in brief.

4.2 Thermal conductivity versus depth for isotropic materials

4.2.1 Assumptions and sensitivity

It is fairly straightforward to calculate the transient temperature increase over time for a hot disc experiment of a composite multilayered device, provided the thickness of the relevant layers as well as their thermal properties are known. However, the inverse problem is mathematically impossible to solve, since different material combinations of

thermal conductivity and thermal diffusivity can give the same temperature response (defined by thermal effusivity, Section 2.2.4.4) in a hot disc experiment (Paper I). The most simple example is 1-dimentional heat propagation through two different materials, which are joined in series. While these materials differ in thermal conductivity and thermal diffusivity, their thermal effusivity (Eff) is the same, since $Eff = \frac{\lambda_1}{\sqrt{\alpha_1}} = \frac{\lambda_2}{\sqrt{\alpha_2}}$ $(\lambda_1 \neq \lambda_2)$. On the other hand, by introducing an assumption of $\rho c_p = constant$, and by analyzing a short-moving time window of data points, a unique estimation of thermal conductivity is possible, which connects it with the depth position (via the time position of the short time window). Although this estimation of thermal conductivity does not truly represent an inversion of the original problem, the estimated thermal conductivity variation with depth correlate with the true inhomogeneity in the sample. In short: A goal is to be able to obtain accurate depth-positioning recordings, in order to be able to detect the position of a defect. However, local thermal conductivity estimations (*i.e.* thermal conductivity of this specific defect) are significantly suppressed in the inverse analysis. Nevertheless, the inversed analysis applied to a homogeneous sample returns the constant thermal conductivity function versus probing depth.

In order to approach this problem hypothetically, it is necessary to first define the smallest probed volume, at which the thermal properties can be correctly estimated via a standard hot disc measurement. Normally, 200 data points are recorded during a measurement, and reliable thermal properties can be calculated utilizing a minimum of 60 data points. For example, homogeneous stainless steel, which has a thermal diffusivity of around 3.6 mm^2/s measured for 10 sec, 60 measurement data points correspond to a time window of 3 sec. During this time, the heat front travels a distance of approx. 6.5 mm from the sensor into the stainless steel sample, which is a fairly large minimum thermal depth of probing, especially if the technique is intended to be applied in QC. The probing depth naturally decreases with experiment time according to Equation 9, and is lower for materials with lower thermal diffusivity.

In order to allow for the measurement of higher-conducting samples at shallower depths, *i.e.* reduced probing depths according Equation 9, the minimum time position must be reduced. The overall reduction in minimum probing depth can be carried out via an increase in the sampling rate, *i.e.* in the density of measurement points. It also depends on hardware capability, and furthermore on the reduction of the number of measurement data points for data analysis. It can be shown that by inserting volumetric heat capacity to the data fitting procedure, the thermal conductivity estimation is greatly stabilized. Thus, merely 20 measurement points are enough to acquire

reproducible thermal conductivity data for homogeneous stainless steel (Table 4.1). By comparison, the average thermal conductivity based on data points 14-200 is estimated at 13.55 W/mK (standard deviation 0.055%). Moreover, the insertion of volumetric heat capacity allows one to overcome the restriction in the time interval $0.3\Theta - \Theta$. This is preferential for the simultaneous determination of thermal conductivity and thermal diffusivity, and results in an extended range of probing depth as recorded by a single sensor.

Table 4.1. Stability of thermal conductivity utilizing fixed ρc_p (3.738 MJ/(m^{3}K)) during shape function fitting.

Data point window	10-30	30-50	50-70	70-90	90-110	110-130	130-150
λ, W/(mK)	13.589	13.516	13.628	13.666	13.555	13.553	13.615
Std. dev., %	0.18	0.75	1.29	0.96	0.88	0.76	0.75

In the case of a multilayer device, the usage of fixed volumetric heat capacity is complicated, since its variation is not defined. Nevertheless, for dense inert materials the volumetric heat capacity is generally known to range between 1–4 MJ/m^{3}K at room temperature [79]. Some materials maintain almost constant volumetric heat capacity while possessing inhomogeneity in thermal conductivity. These involve biological matters, or materials with inclusions or defects, for instance a specimen which experiences fatigue. Accumulation of dislocations reduces the average thermal conductivity of a specimen at reversal load conditions (Figure 27). The defects created are not accompanied with any significant change in volumetric heat capacity. However, the defects directly affect the phonon propagation, and, hence, influence the thermal conductivity. Thus, QC can be performed whereby the device is taken out just before a failure, *i.e.* when it's thermal conductivity reaches the critical minimum value (red line in Figure 27). In such case, the function of thermal conductivity throughout probing depth would help to investigate which part of the device deteriorates the more rapidly.

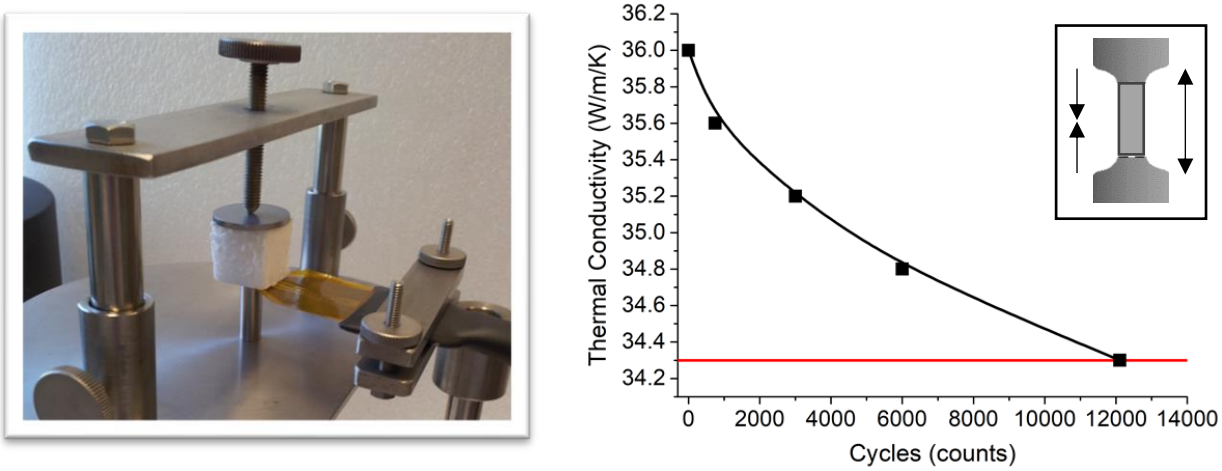

a) b)

Figure 27. Testing a specimen under reversal load: a) measurement setup; b) graph of the thermal conductivity reduction due to defects accumulation (red line represents the critical minimal thermal conductivity) (*c.f.* Andrey Sizov's master thesis report).

An advantage with the insertion of volumetric heat capacity for SP technique is that an error in volumetric heat capacity does not result in the same error ensuing in the calculated thermal conductivity; it is less since the thermal conductivity is a component of the slope (Equation 11), which does not change much with varying ρc_p parameter.

4.2.2 Mathematical procedure

By introducing certain assumptions, it is possible to compute an approximate function of the thermal conductivity versus probing depth. One way to increase the resolution of a thermal conductivity versus depth analysis, is to increase the sampling rate. An increased sampling rate, will, in turn, allow for the estimation of thermal conductivity at shallower depths. With the available hardware today, it is possible to increase the sampling rate from nominally 200 to 2000 measurement points. The acquired transient curve should then be analyzed in short time windows (with a size of N points). The time window moves from the beginning of the transient (points [0, N]) to its end (points [2000-N, 2000] with a step of 1 point (Figure 28).

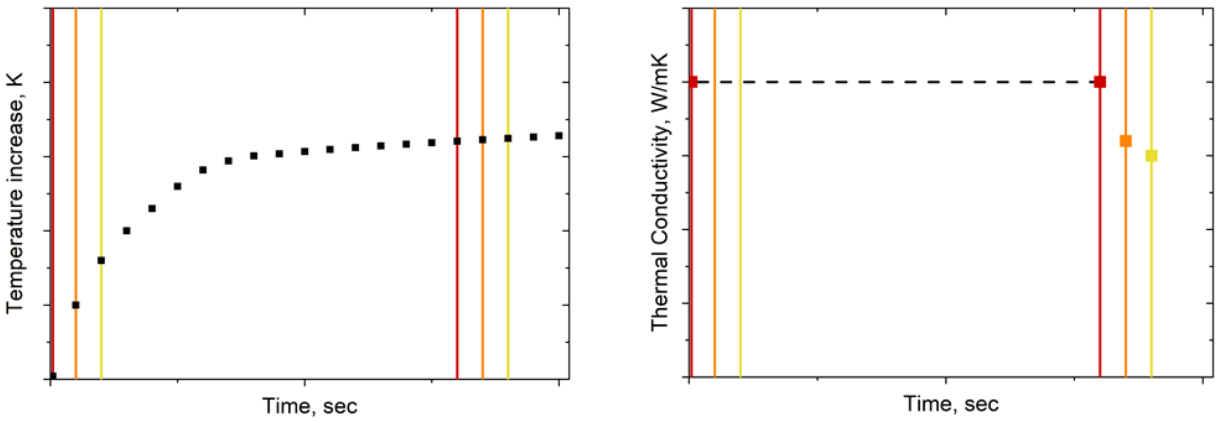

a) b)

Figure 28. Thermal conductivity estimation from moving small time window: a) recorded transient profile; b) estimated thermal conductivity vs. time.

The thermal conductivity is estimated locally in every such time window utilizing the original standard mathematical model presented by Equation 11. The estimated thermal conductivity is assumed valid for a given time position, *i.e.* the location of this short time window. When the function of thermal conductivity vs. time position is obtained, it is of interest to connect the local time position with the local depth position. This is done according to the modified Equation 9:

$$x_n(t,\lambda) = 2 * \sqrt{\frac{\bar{\lambda}_n(x) t_n}{\rho c_p}} \qquad \text{(Eq.25)}$$

where $x_n(t,\lambda)$ is the local probing depth, and $\bar{\lambda}_n(x)$ is the weighted average thermal conductivity, which is defined as:

$$\bar{\lambda}_n(x) = \frac{1}{x_n}\int_0^{x_n} \lambda(x)dx \cong \frac{\sum_{i=1}^{n}\left\{\frac{(\lambda_i + \lambda_{i-1})}{2}\cdot f_i\right\}}{\sum_{i=1}^{n} f_i} \qquad \text{(Eq.26)}$$

where $f_i = (x_i - x_{i-1})$ is the weighted factor. The easiest way to solve Equation 25 is to numerically iterate x_n. For the first iteration cycle, x_1 is set to 1 mm, and this converges already after 2-3 cycles. Every next x_n for the first iteration cycle is obtained as $x_n = 2x_{n-1} - x_{n-2}$. Since the thermal conductivity cannot be estimated at depths shallower than the minimum probing depth, it is assumed that $\lambda_0 = \lambda_1$.

4.3 Thermal conductivity versus depth for anisotropic materials

4.3.1 Testing materials in the normal direction to the sensor plane

Most materials possess anisotropy to a certain extent. Even commonly used metals that are normally believed to be isotropic – stainless steel, brass, etc. – at times display a deviation in thermal properties up to 10% depending on the direction of heat propagation.

In some applications, it is important to test materials/devices in the axial (through-plane or normal to the sensor plane) direction. For instance, the through-plane thermal conductivity matters for textiles, and their thermal conductivity in-plane (radial) is different. The variation of the thermal conductivity in the normal direction versus probing depth is also of interest for production purposes, and towards understanding the overall performance of textiles in operational conditions. It is also of interest to study the change of structure and constitution of human skin, *e.g.* when a moisturizing substance is applied. This change can be assessed by way of thermal conductivity tracking. The function of the thermal conductivity vs. depth profile through-plane can be used to obtain the penetration depth of a lotion into a skin. Testing a skin utilizing the Transient Plane Source method is possible due to its inherent ability to probe non-destructively as well as in a single-sided manner. Moreover, the method accommodates a safe and modest temperature increase on the skin surface of around 1–2 K, while the high sensitivity and reproducibility of the method allows to track slight variations in the thermal conductivity of skin. Potentially, the technique can also be used the medical applications, *e.g.* in aiding skin cancer identification.

One of the techniques that can be used to measure the thermal conductivity in the normal direction is the existing Anisotropic Hot Disk method described in Section 2.2.4.3. However, this method requires the in-plane depth of probing during transient recording to be greater than the sensor radius, and furthermore to not exceed the sensor diameter (following $0.33 < \frac{t_{max}}{\theta} < 1$). In addition, a comparatively large amount of measurement points has to be included in the analysis of the thermal properties in order to arrive at stable and correct values. All these factors limit the sensitivity, quality of data and possible range of probing depths.

Alternatively, a concept of the thermal effusivity described in Section 2.2.4.4 can be utilized to acquire thermal properties in the normal direction. With prior knowledge of the volumetric heat capacity value, the Equation 16 could immediately be applied in order to obtain the thermal conductivity in the normal direction. At the same time, such a method can be combined with the suggested computational procedure described in Chapter 4.2.2 (also *cf.* Paper 1) to estimate the variation of the thermal conductivity vs. depth profile in the normal direction.

One option to measure thermal effusivity is by applying the Hot Disk One–Dimensional method [40] to rod-like samples with the thermal conductivity above 1 W/mK. In this case, only the thermal properties along a rod can be obtained. The sensor diameter should be chosen to be slightly smaller than the diameter of the rod.

If the thermal conductivity of samples in question is below 1 W/mK, the method could be applied only to bulk or layered structures under specific conditions: the total measurement time of a transient recording (t_{max}) also has to be selected to be significantly shorter than the characteristic time defined by $\theta = \frac{r^2}{\alpha_{in-plane}}$, where r is the sensor radius and $\alpha_{in-plane}$ is the thermal diffusivity in-plane. Thus, *e.g.* when $t_{max} < 0.1\theta$, the transient curve of the 3D samples is similar to the output from the rod-like "one-dimensional" samples. Since the probing depth and total measurement time are coupled via Equation 9, this inequality is fulfilled when the heat propagation occurs just barely at shallow depths. The results obtained from such a small interaction volume may differ from the results when a significant sample volume is probed through. With this method, the probing depth can only be increased by way of increasing the sensor radius in order to increase the characteristic time (according to the equation above). Due to the limitation of the minimal possible measurement time during a transient recording (hardware limitation), this approach cannot be applied to materials with relatively high $\alpha_{in-plane}$, because heat would then propagate on unacceptably far from the sensor, and the 1-dimensional analysis on a 3D sample would return highly distorted results.

This thermal effusivity approach and its limitations are demonstrated on an example of printing paper stack testing. The sample was premeasured with the Anisotropic Hot Disk method in order to obtain the thermal conductivity in axial and radial directions, which are 0.091 and 0.470 W/mK, respectively. The volumetric heat capacity of the paper stack (used to separate the thermal properties into radial and axial components)

was calculated from the density of the stack sample and tabular specific heat per unit mass for printing paper – 0.945 MJ/m^{3}K. The Hot Disk sensor with the radius 29.5 mm was sandwiched between two identical stacks with dimensions 110x110x4.5 mm^3 each. A weight of 2.5 kg was applied in order to control the contact thermal resistance on the interfaces between paper sheets. The results were obtained using the time window with omitted 0.7 sec in the beginning of the transient curve (in order to avoid the effect of initial contact resistances and unestablished transient heat flow at shallow depths). They are presented in Table 4.2.

Table 4.2. The thermal properties of a paper stack utilizing the Hot Disk One–Dimensional method.

Measurement time, sec	**2**	**5**	**10**	**20**
Thermal Effusivity through-plane, kJ/(m^{2}Ks$^{1/2}$)	0.293	0.298	0.300	0.304
Thermal conductivity through-plane, W/mK	0.091	0.094	0.095	0.098
Probing depth through-plane, mm	0.9	1.4	2.0	2.9

The presented values are an average of 3 consecutive measurements with the standard deviation below 1%.

The best fit of the 3D setup into the 1D model was obtained for the 2 sec measurement time. This result matches well with the result provided using the Anisotropic Hot Disk test. According to the Table 4.2, the longer the measurement time is, the more thermal conductivity deviates from the original value. After 20 sec, the thermal conductivity value is overestimated by around 8%; however, the error is smaller for the obtained thermal effusivity value, which is 4%. This error could be reduced by taking into account the gradually increasing cross section area of the plane heat source. This result is also in line with the analysis of the residual plot – the deviation of the 3D experimental data from the theoretical 1D model increases with duration of measurement time. Due firstly to the error in the thermal conductivity estimation, in turn depending on the (measurement time)/(probing depth); furthermore due to limitations in the thermal diffusivity in radial directions; and finally due to the necessity accruing from a larger sensor radius, a new method was developed for the structural evaluation of anisotropic materials in the normal direction to the sensor plane.

4.3.2 Computational procedure

The original Structural Probe method (Paper I) is in this work modified to an extent to provide a function of the thermal conductivity vs. probing depth in the axial direction, when measuring anisotropic inhomogeneous materials (Paper IV). This new approach requires knowledge of the true volumetric heat capacity $(\rho c_p)_{\text{true}}$ as well as false

volumetric heat capacity $(\rho c_p)_{\text{false}}$ values. The true volumetric heat capacity is a real physical property of the sample under study, and is also used for separation of the thermal properties in different directions when using the Hot Disk Anisotropic method. It is calculated from the density of an anisotropic sample and the tabular heat capacity per unit mass, which normally does not deviate much in materials. Alternatively, it could be measured with the Hot Disk Specific Heat method if certain conditions are fulfilled (*cf.* Section 2.2.4.5). The false volumetric heat capacity is obtained via the Hot Disk Standard (Isotropic) method from the measured geometrical average thermal conductivity ($\sqrt{\lambda_{\text{in-plane}}\lambda_{\text{through-plane}}}$) and the thermal diffusivity in-plane ($\alpha_{in-plane}$) according to:

$$(\rho c_p)_{\text{false}} = \frac{\sqrt{\lambda_{\text{in-plane}}\lambda_{\text{through-plane}}}}{\alpha_{in-plane}} \quad \text{(Eq.27)}$$

The false volumetric heat capacity is for its part obtained when testing under measurement times within $0.33 < \frac{t_{max}}{\theta} < 1$, where both sensitivity coefficients – for estimation of geometrical average thermal conductivity and in-plane thermal diffusivity – are the highest [38].

The true and false volumetric heat capacity values are also used to determine the Anisotropic Ratio (AR), which represents the ratio of thermal conductivity values in-plane and through-plane ($\text{AR} = \frac{\lambda_{\text{in-plane}}}{\lambda_{\text{through-plane}}}$):

$$(\rho c_p)_{\text{false}} = (\rho c_p)_{\text{true}} \cdot \frac{1}{\sqrt{AR}} \quad \text{(Eq.28)}$$

When measuring anisotropic samples, the iterative computations described in Paper I are carried out with the insertion of the false volumetric heat capacity instead of the true volumetric heat capacity, as in the case of isotropic samples. This approach results in the function of $\sqrt{\lambda_{\text{in-plane}}\lambda_{\text{through-plane}}}$ versus $d_{p,radial}$ (thermal depth of probing from the sensor lateral boundary into the radial direction). In order to obtain the function of the through-plane thermal conductivity versus through-plain probing depth ($d_{p,axial}$), the following transformations are applied:

$$d_{p,axial} = \frac{1}{\sqrt{AR}} \cdot d_{p,radial} \quad \text{(Eq.29)}$$

$$\lambda_{\text{through-plane}} = \frac{1}{\sqrt{AR}} \cdot \sqrt{\lambda_{\text{in-plane}} \lambda_{\text{through-plane}}} \quad \text{(Eq.30)}$$

If the function of the in-plane thermal conductivity versus probing depth in radial direction is of interest, the $\lambda_{\text{in-plane}}$ can be computed as:

$$\lambda_{\text{in-plane}} = \sqrt{AR} \cdot \sqrt{\lambda_{\text{in-plane}} \lambda_{\text{through-plane}}} \quad \text{(Eq.31)}$$

The result of the suggested computational procedure applied to paper and Mica stacks with defects is presented in Section 4.5.2.

4.4 Structural probe testing

4.4.1 Homogeneous materials

The structural probe technique was also tested on homogeneous materials, in order to ensure its operational ability. Balance between accuracy and sensitivity can be achieved by varying the size of the short time window consisting of N points, which is used to calculate the "local" thermal conductivity. For instance, if N equals 20 points, the noise in thermal conductivity is higher than if N is 60 or 90 data points (Figure 29a). Hence, the time window should be chosen depending on application purposes. In the following, the time window is set to 60 points.

In Figure 29b, it can be observed that the results acquired by the SP technique, when performing two different measurements of the same stainless steel sample, are reproducible (red and green curves). The yellow curve in Figure 29b represents the experiment, when one side of the sensor is covered with the stainless steel sample and another with insulating Styrofoam, *i.e.* a single-sided setup, which is the most practicable for QC applications. This curve repeats the shape of those acquired by the double-sided setup; however it shows slightly lower thermal conductivity due to heat losses into the backing Styrofoam. Also, the effect of insulation material and the single-sided setup can be seen in the beginning of the curve, displaying an initially lower thermal conductivity.

In sum, the SP technique appears to be more sensitive when applied to dense materials with lower thermal diffusivity. A significantly reduced fluctuation in the thermal

conductivity value is observed for the low-conductive soft rubber (Figure 29c), as compared to the fluctuation for the highly-conductive copper rods (Figure 29d).

The thermal conductivity vs. probing depth is constant for homogeneous materials. The sharp deviations observed in Figures 29 (a–d) at the far ends of the curves occur when the local probing depths reach the lateral boundaries of the sample. The closest distance from the hot disc sensor to the sample edges was: 20 mm for stainless steel, 4.5 mm for soft rubber and 50 mm for copper rods. The sharp deviations that occur at approximately these depths, for the respective cases, show that the probing depth calculations with Equation 9 and 25 are fairly accurate. However the empirical coefficient 2 before the square root could be chosen with a slightly higher value.

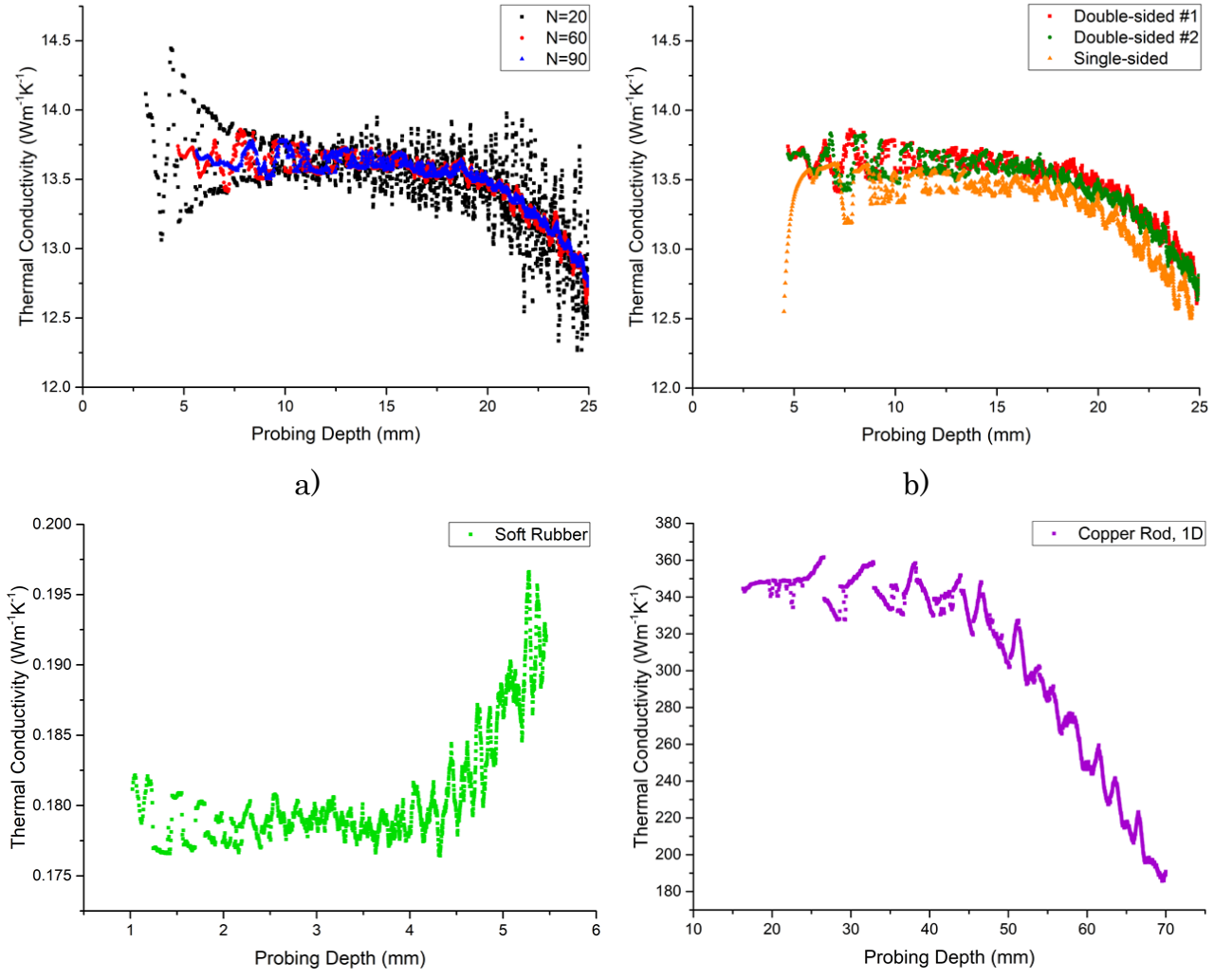

Figure 29. Application of the SP technique to stainless steel (a–b), soft rubber stack (c) and copper rods (d).

4.4.2 Inhomogeneous materials

In Figure 30, the thermal conductivity vs. probing depth is demonstrated for Gypsum and Styrofoam samples. An inhomogeneity in Styrofoam is recorded by the SP technique at shallower depths. Perhaps these variations are due to the melted zone on the surface from contact with a thermal saw. This resulted in the annihilation of pores, hence rendering higher thermal conductivity values in the near-surface zone. The thermal conductivity value stabilizes at greater depths, where the material appears to be homogeneous. The thermal conductivity vs. probing depth of Gypsum also indicates inhomogeneity. Visibly, a cross section of the Gypsum board clearly shows that the porosity varies spatially. Other examples of inhomogeneous materials can be found in Paper II.

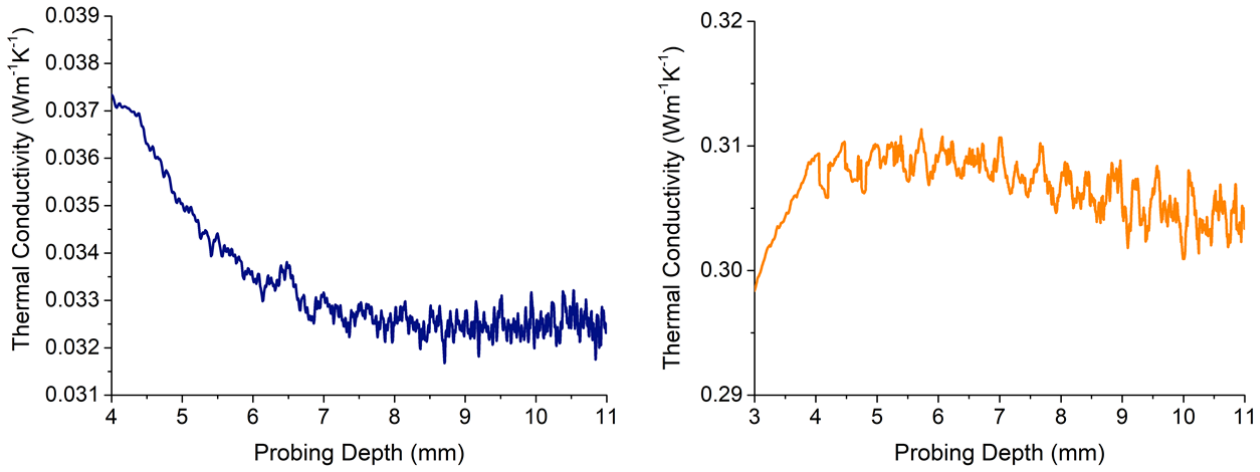

a) b)

Figure 30. The SP technique data for inhomogeneous Styrofoam (a) and Gypsum (b).

In accordance with the model assumptions, for inverting the temperature vs. time signal into the thermal conductivity vs. depth, the thermal conductivity estimation does not represent the real thermal conductivity variation in the material under study.

In general, the ability of the SP technique to detect the variation of thermal conductivity could be utilized for assessing thermal conductivity trends of gradient materials, or could serve as an indicator of certain structural changes in the material. In order to make solid judgments about what precise transformations in the material occur, extra information about the material in question can be required. The trends in thermal conductivity could be connected with the expectations of material change after a certain treatment, or be combined with additional measurement techniques, which in turn

could support with additional data helping to clarify the variation in thermal conductivity.

4.5 Detection of defects

4.5.1 Isotropic materials

The presence of local macrodefects influences the transient temperature profile. Since the transient curve is analyzed via small time windows, it is possible to see at which time the probing depth reaches an "obstacle" and to connect this time window with the depth position of the "obstacle". Hence, the location of such local inhomogeneity can be detected. This was demonstrated for the example of a soft rubber layered stack with internal cavity (Figure 31a) and copper inclusion (Figure 31b) located at a distance of 1.5 and 3.0 mm from the sensor plane. In both cases, the thermal conductivity variation remains constant with depth until the thermal depth of probing reaches the "obstacles", which indicates a homogeneous constitution of the rubber samples. When the probing depth reaches the defect position, the thermal conductivity vs. probing depth starts deviating towards the thermal conductivity values of these defects, which are approx. 0.02 W/mK (air) and 350 W/mK (copper). The deviation of the curves occurs at the probing depth position, which is consistent with the real location of the defects.

An important observation in these tests is that the sensitivity of the SP technique decays with increasing probing depth. It is found that the thermal conductivity variation with depth will give a stronger response to a defect, if the defect is located closer to the sensor. It also implies that smaller defects can be detected at shallower depths. The reduction in sensitivity can be explained by the influence of the shallower depths of the matrix material on the overall transient temperature profile. In addition, if the setup is 3D, the sideway heat propagation may also reduce the sensitivity.

Obviously, larger-size defects should have a bigger influence on the transient experiment. Taking the same sample of a soft rubber stack and creating defects of different volumes, it is possible to see that the deviation slope is proportional to the size of the defect (Figure 31c and 31d). Thus, an increase in the cavity volume, arranged to approx. 4, 32 and 64 mm^3, forces the curve to deviate more quickly towards the thermal conductivity of air. The same trend is observed for the sample with copper inclusions of different volumes, approx. 13, 27, 53 mm^3, at which the curve deviates more rapidly towards the thermal conductivity of copper. Thus, it is possible to find the location of

defects, assess their size and possibly garner some indication of their thermal conductivity.

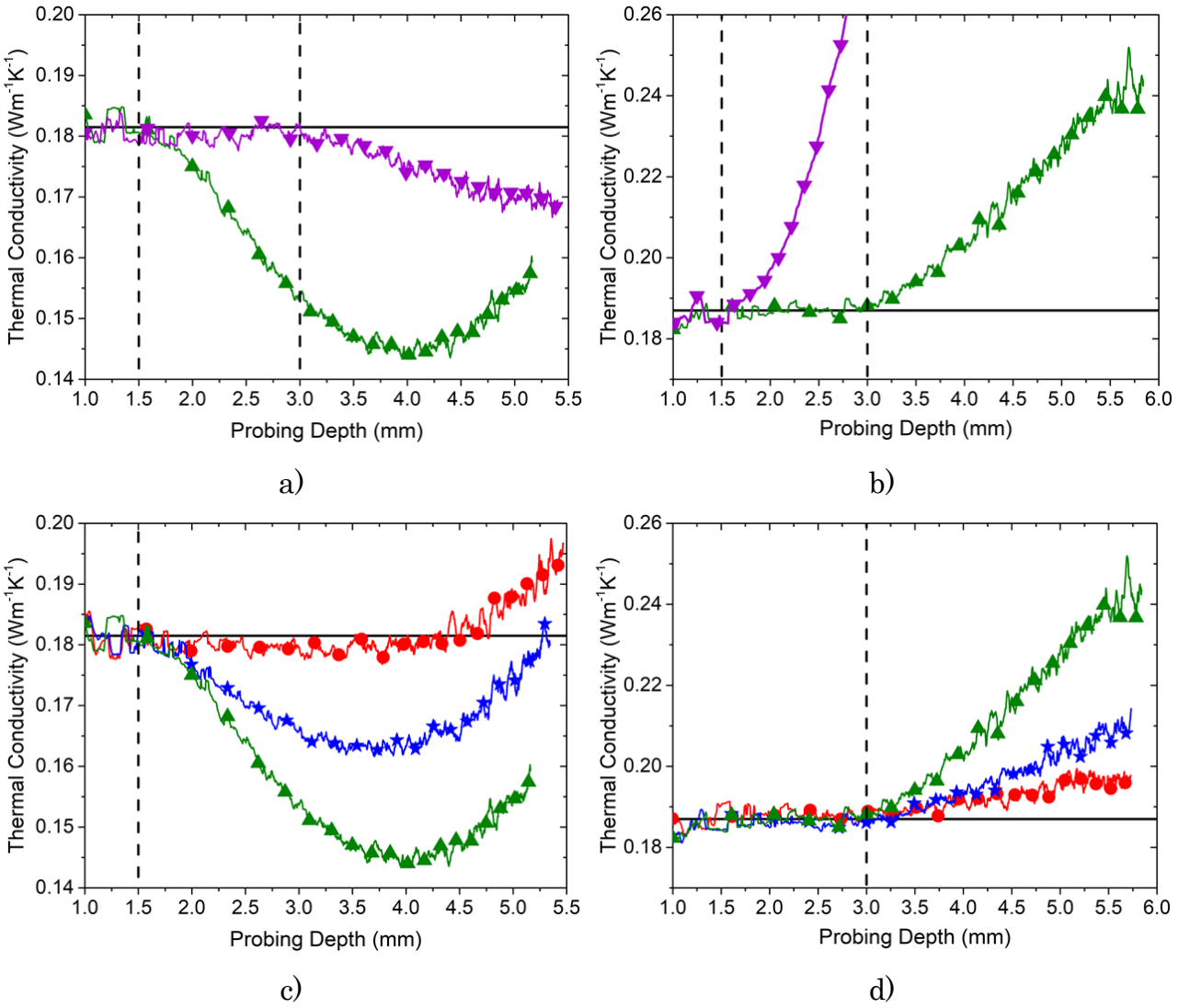

Figure 31. Thermal conductivity vs. probing depth for soft rubber stacks with cavities or copper inclusions. (a) Cavity volume is 64 mm^3; (b) Copper inclusion volume is 53 mm^3; (c) Cavities volume: red curve – 4 mm^3, blue curve – 32 mm^3, green curve – 64 mm^3; (d) Copper inclusions volume: red curve – 13 mm^3, blue curve – 27 mm^3, green curve – 53 mm^3.

This property could be useful in the detection of undesired bubbles, *e.g.* in hardened concrete or polymers, or of unexpected inclusions in casted metals, etc. In addition, it should be possible to detect cracks in construction materials under a stress or in load-sensitive biological structures, such as horse hooves [80]. The existing methods of investigating race horse hooves, *e.g.* X-ray imaging, often fail to detect the presence of cracks or inflammations. Structural probing is a promising technique to locate such

inflammations, since they result in a higher amount of liquid in the inflammation zone. Hence, the thermal conductivity function should deviate upwards in case an inflammation is present. The downwards deviation is expected in the case of cracks in the hoof from the crack position and going deeper into the structure.

4.5.2 Anisotropic materials

The utilization of a computational procedure (Section 4.3.2) allows one to rescale the function of the thermal conductivity versus probing depth (calculated with $(\rho c_p)_{\text{false}}$) obtained by the original Structural Probe method (Section 4.2.2). An example of such rescaling is plotted in Figure 32.

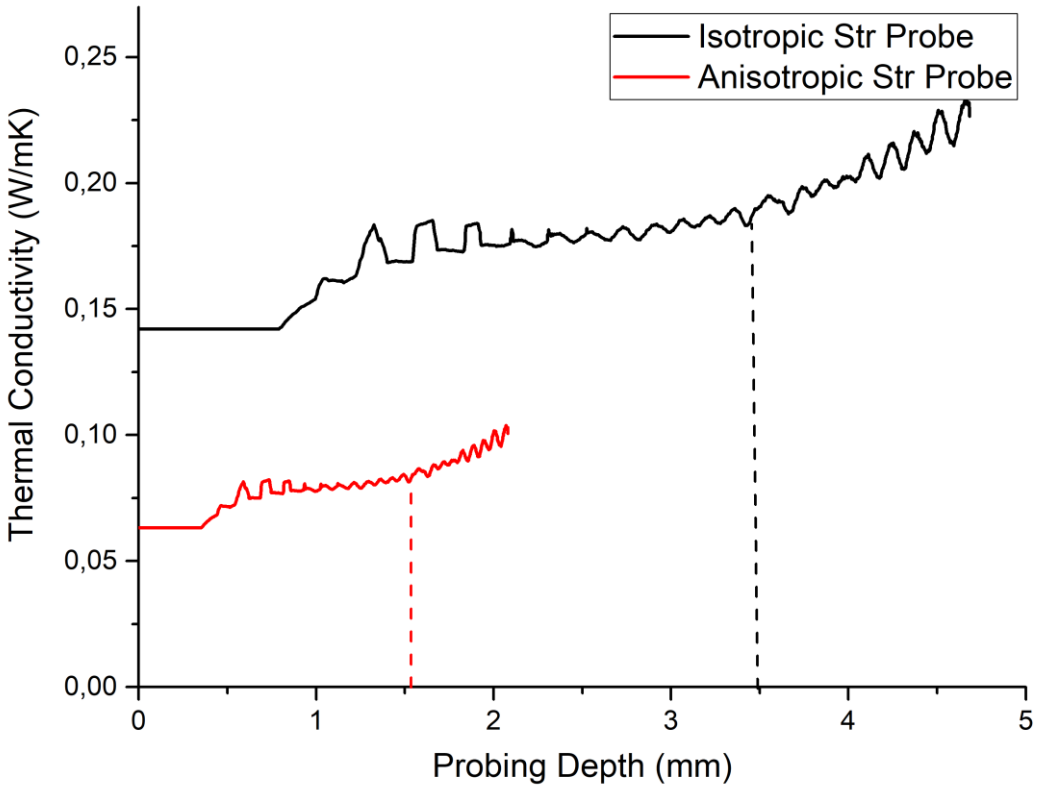

Figure 32. Thermal conductivity versus probing depth, acquired using the original method with $(\rho c_p)_{\text{false}}$ and the new approach on a printing paper stack.

Thus, the thermal conductivity function obtained by the original method with $(\rho c_p)_{\text{false}}$ (black curve in Figure 32) deviates at 3.5 mm, suggesting that the Cu defect is located at this particular depth. However, the real position of the defect is at 1.5 mm. The new approach (red curve in Figure 32) results in a correct estimation of the through-plane thermal conductivity of the stack sample, and yields the real location of the defect.

The schematic measurement setup of stack samples and the positioning of a defect utilized for this example (and for the study in Paper IV) is illustrated in Figure 33. A choice of stack samples to demonstrate the capability of the new method was made based on the relative simplicity of incorporating defects at different depth positions. However, this new approach is not limited to stacks, but can also be applied to bulk samples exhibiting anisotropic thermal properties.

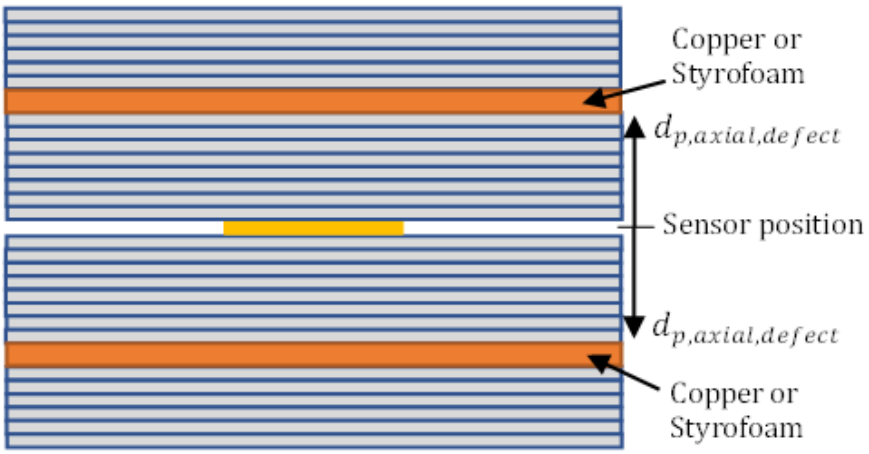

Figure 33. The schematic measurement setup utilized to demonstrate the capability of the Anisotropic Structural Probe method.

The stacks tested in Paper IV were made of either printing paper or Mica sheets (*cf.* Table 4.3) with the corresponding thickness of a single layer – 0.13 and 0.50 mm, respectively. A choice of defects was made based on their thermal conductivity values and the thermal conductivity of the stack samples: the more the thermal conductivity differed from the thermal conductivity of a stack, the greater the thermal conductivity function deviated towards the thermal conductivity of the corresponding defect. This increased the sensitivity of the method. Real positions of defects are given in Table 4.4.

Table 4.3. The parameters of the samples in the current work.

Sample	$\lambda_{through-plane}$, W/mK	$\lambda_{in-plane}$, W/mK	$(\rho c_p)_{true}$, MJ/m³K	$(\rho c_p)_{false}$, MJ/m³K	$\sqrt{AR}$
Paper stack	0.079	0.464	0.945	0.42	2.25
Mica stack	0.129	2.466	1.79	0.41	4.37

Table 4.4. Defects and their depth position in the sample of the current work.

Sample	Defects					
	Cu (λ =400 W/mK)			Styrofoam (λ = 0.035 W/mK)		
Paper stack	at 1 mm	at 1.5 mm	at 2 mm	-	-	-
Mica stack	at 1 mm	at 1.5 mm	at 2 mm	at 1 mm	at 1.5 mm	-

Figures 34 and 35 display the outcomes of using thermal conductivity profiling to investigate defect mapping. To serve as a benchmark for detecting such defects, the Mica and paper stacks, without any defects inserted, underwent analysis using the standard Hot Disk Anisotropy method. The numerical value of this benchmark is indicated by the black constant line in the figures, and is also presented in Table 4.3.

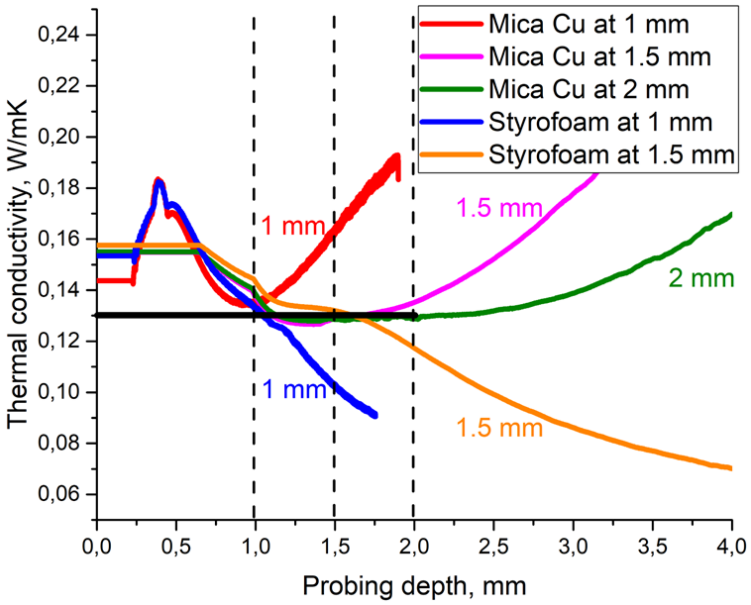

Figure 34. Thermal conductivity in normal direction vs. depth profile of the Mica stack with defects at different locations. The constant black line represents $\lambda_{\text{through-plane}}$ obtained using the anisotropic method [39]

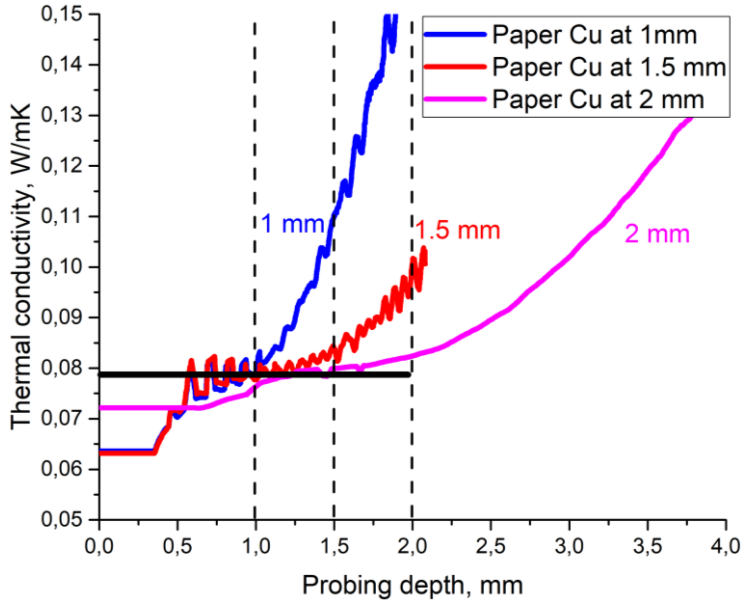

Figure 35. Thermal conductivity in normal direction vs. depth profile of the paper stack with defects at different locations. The constant black line represents $\lambda_{\text{through-plane}}$ obtained using the anisotropic method [39].

As these figures show, the deviation of the thermal conductivity function occurs at probing depths close to the real locations of defects. The point of deviation is somehow slightly underestimated in the case of the paper stack, while overestimated in the case of the Mica stack. Such effects could be caused by distorted thermal conductivity values at depths below 1 mm. This distortion may occur because the transient heat flow requires travel through a couple of periods of alternating layers in order to act as a "continuum". Normally, when using the standard Hot Disk techniques, the first measurement points are omitted in order to avoid the influence of initial thermal resistances and "non-continuum" behavior (in the case of stacks) on the results. In addition, a slight shift of the functions plateau is most likely due to dismounting and reassembling the measurement setup when changing positions of defects, because this process could change the thermal contact resistances between the layers. Moreover, a stack could also be slightly inhomogeneous, and therefore, the plateau of the thermal conductivity functions appears with a slight slope. Alternatively, the density of stacks could change slightly, which could also influence the slope of the function.

Similarly to the original Structural Probe method, the sensitivity of the new method decreases with increasing the probing depth.

Chapter 5

Concluding remarks and future work

The focus of the current work was set on understanding the behavior of the system Mg_2Si-Mg_2Sn. Thus, the uncertainty in the available phase diagrams was clarified in the Si-rich region. However, the Sn-rich region still needs more thorough examination. Hence, one of the directions for future work is to investigate the binodal curve in this region in more detail. Nevertheless, the current experimental results, which showed an agreement of the binodal line in the Si-rich region with Viennois et al. [14], provide important information, which can be utilized for manipulating the undoped $Mg_2Si_{1-x}Sn_x$ microstructure. Thus, the desired fine microstructure, formed due to spinodal decomposition, was achieved in the samples $Mg_2Si_{1-x}Sn_x$ with $x<0.13$, and confirmed by XRD. Further characterization of the spinodal structures could be approached by TEM and SAXS. Moreover, future work should include a design of heat treatment protocols to achieve spinodal decomposition in solid solutions with a higher Sn content. The thermoelectric material with a composition approaching $Mg_2Si_{0.60}Sn_{0.40}$ will be of a particular interest, since this currently exhibits the best thermoelectric performance in the group $Mg_2Si_{1-x}Sn_x$.

The study of Bi-dopped $Mg_2Si_{0.82}Sn_{0.18}$ and $Mg_2Si_{0.60}Sn_{0.40}$ revealed the very complex microstructure of homogenized solid solutions upon cooling in SPS. To the knowledge of the author, such complicated microstructure has not been reported before. Moreover, it was demonstrated that the same microstructure changes with an increase in

homogenization time. It is suggested that Mg excess, the presence of Bi and possible strain energy between the formed phases could cause this change and complexity. Such behavior of the solid solutions is of interest, since it allows the creation of more complex microstructures, which could be more beneficial for thermoelectric energy conversion. However, more research in this direction is needed.

In addition, the TE materials with gradient concentration may be challenging in terms of thermal conductivity measurements. This problem can be approached by the structural probe technique, which should be able to assess the thermal conductivity variation even in the conditions of changing volumetric heat capacity with depth. In the context of the present work, the technique proved its ability to test homogeneous and inhomogeneous materials as well as to detect defects (local inhomogeneities). It is expected that structural probing can become a reliable technique for examination of the structural variation of thermoelectric devices as sintered by SPS. Also, the technique will be further developed, *e.g.* with improved calculations and accuracy, and further application of the technique to materials with various geometries.

Acknowledgements

I gratefully acknowledge project funding from Hot Disk AB and the Swedish Energy Agency (Energimyndigheten, project 38340-1). My project was also supported by the Danish Innovation Foundation funded Center for Thermoelectric Energy Conversion, and by Danish National Research Foundation (DNRF93) through the Center for Materials Crystallography.

Special acknowledgement is given to my main supervisor Dr. Anders Palmqvist, who shared his rich scientific experience with me, and to my supervisor/employer Dr. Mattias Gustavsson, who provided excellent working conditions, guided me well throughout the entire project and helped with analysis and writing papers.

I would furthermore like to thank my secondary supervisor Dr. Paul Erhart for participation in the project as well as Dr. Hazel Reardon for help with XRD measurements and data analysis.

In addition, I appreciate much help with writing papers from Dr. Besira Mihiretie and Dr. Anton Ma. I was happy to receive such a thorough language proofing of my manuscript by Dr. Henrik Otterberg. Assistance from Dr. Silas E. Gustafsson has also been very valuable for me.

The comments from Dr. Martin Andersson and Dr. Nina Kann regarding my thesis were very helpful to me, and I admire their expertise.

And finally, I would like to thank all colleagues in our Applied Chemistry division and Hot Disk AB for indirect support. And, indeed, I send regards to my close people, who believed in me and gave me additional power.

References

1 Brundtland Commission. "Report of the World Commission on Environment and Development". United Nations, 1987.
2 “Sweden in a World of Growing Uncertainties”, https://www.regeringen.se/rapporter/2013/02/framtidskommissionen---underlagsrapport-sweden-in-a-world-of-growing-uncertainties/
3 “Sweden in a World of Growing Uncertainties”, p. 25, https://www.regeringen.se/rapporter/2013/02/framtidskommissionen---underlagsrapport-sweden-in-a-world-of-growing-uncertainties/
4 Article: “NASA’s Voyager Will Do More Science With New Power Strategy”, https://www.jpl.nasa.gov/news/nasas-voyager-will-do-more-science-with-new-power-strategy
5 A Comprehensive Study on the Effect of Inhomogeneous Heat Dissipation on Battery Electrochemical Performance, Yi Xie, Xingyu Mu, Zhongwei Deng, Kaiqing Zhang, Bin Chen and Yining Fan, *Electronics* 2023, 12 (6), 1266; https://doi.org/10.3390/electronics12061266
6 The Transient Plane Source technique (TPS) to measure thermal conductivity and its potential as a tool to detect in-homogeneities in metal foams, M.A. Rodríguez-Pérez, J.A. Reglero, D. Lehmhus, M. Wichmann, J. A. de Saja, A. Fernández, International Conference “Advanced metallic materials”, 5-7 November, 2003, Smolenice, Slovakia
7 A.U. Khan, N. Vlachos, and Th. Kyratsi*, Scripta Materialia*. 2013, 69 (8), 606–609.
8 B. Poudel, Q. Hao, Y. Ma, Y. Lan, A. Minnich, and B. Yu, *Science* (New York, NY), 2008, 320, 634–638.
9 S. H. Lo, J. He, K. Biswas, M. G. Kanatzidis, and V. P. Dravid, *Advanced Functional Materials*, 2012, 22 (24), 5175-5184.
10 K. Biswas, J. He, I. D. Blum, C.-I Wu, T. P. Hogan, D. N. Seidman, V. P. Dravid and M. G. Kanatzidis, *Nature*, 2012, 489, 414-418.
11 A. Kozlov, J. Gröbner, and R. Schmid-Fetzer, *J. Alloy Compd.*, 2011, 509, 3326-3337.
12 I. H. Jung, D.H. Kang, W.J. Park, N.J. Kim, and S.H., *Ahn, Calphad*, 2007, 31, 192.
13 E. N. Nikitin, E. N. Tkalenko, V. K. Zaitsev, A. I. Zaslavskii, and A. K. Kuzentsov, *Inorg. Mater.*, 1968, 4, 1656–1659.
14 R. Viennois, C. Colinet, P. Jund, and J.-C. Tédenac, Intermetallics, 2012, 31, 146.
15 Mohammad Yasseri, Aryan Sankhla, Hasbuna Kamila, Rachel Orenstein, D.Y. Nhi Truong, Nader Farahi, Johannes de Boor, Eckhard Mueller, Solid solution formation in $Mg_2(Si,Sn)$ and shape of the miscibility gap, Acta Materialia, Volume 185, 2020, Pages 80-88, ISSN 1359-6454, https://doi.org/10.1016/j.actamat.2019.11.054

16 Phase transformations in Metals and Alloys, D.A. Porter, K.E. Easterling, p.302
17 J. Androulakis, C.-H. Lin, H.-J. Kong, C. Uher, C.-I. Wu, T. Hogan, B. A. Cook, T. Caillat, K. M. Paraskevopoulos, and M. G. Kanatzidis, *J. Am. Chem. Soc.*, 2007, 129, 9780–9788.
18 M.-S. Kim, W.-J. Lee, K.-H. Cho, J.-P. Ahn, and Y.-M. Sung, *ACS Nano*, 2016, 10, 7197-7207.
19 Phase transformations in Metals and Alloys D.A. Porter, K.E. Easterling, p.290
20 Y. Zhang, Development of simulation tool for synthesis of thermoelectric materials by spark plasma sintering, master thesis, Chalmers University of Technology, 2017.
21 ISO 22007-2:2015, Plastics -- Determination of thermal conductivity and thermal diffusivity -- Part 2: Transient plane heat source (hot disc) method.
22 S. E. Gustafsson, *Rev. Sci. Instrum*. 1991, 62, 797
23 T. J. Seebeck, and Abh. Königl., *Akad. Wiss. Berlin*, 289 (1820-1821).
24 T. J. Seebeck, and Abh. Königl., *Akad. Wiss. Berlin*, 265 (1822-1823).
25 T. J. Seebeck, *Ann. Phys.*, 1826, 83, 203-216.
26 J. C. Peltier, *Ann. Chim. Phys.*, 1834, 56, 371.
27 W. Thomson, Proceedings of the Royal Society of Edinburgh, 1851, 91, 1851.
28 W. Thomson, Account of researches in thermo-electricity. Proceedings of the Royal Society of London, 1854. 7, 49-58.
29 H. J. Goldsmid, in CRC Handbook of Thermoelectrics, edited by D. M. Rowe (CRC Press LLC, 1995), Chapt. 3.
30 D. D. Pollock, in CRC Handbook of Thermoelectrics, edited by D. M. Rowe (CRC Press LLC, 1995), Chapt. 2.
31 G. J. Snyder and E. S. Toberer, *Nat. Mater.*, 2008, 7, 105-114.
32 S. Iwanaga, E. S. Toberer, A. Lalonde, and G. J. Snyder, *Rev. Sci. Instrum.*, 2011, 82 (6), 063905.
33 A. T. Burkov, A. Heinrich, P. P. Konstantinov, T. Nakama, and K. Yasaki, *Measurement Science and Technology*, 2001, 12, 264-272.
34 R. Franz, and G. Wiedemann, *Annalen der Physik.*, 1853, 165 (8), 497–531.
35 D. A. Galson, N. P. Wilson, U. Schärli, and L. Rybach, *Geothermics*, 1987, 16 (3), 215-226.
36 ISO22007-4:2008, Plastics -- Determination of thermal conductivity and thermal diffusivity – Part 4: Laser flash method.
37 S. E. Gustafsson, K. Ahmed, A. J. Hamdani, and A. Maqsood, *J. Appl. Phys.*, 1982, 53, 6064.
38 V. Bohac, M. K. Gustavsson, L. Kubicar and S. E. Gustafsson, *Rev. Sci. Instrum.,* 2000, 71, 2452.

39 M. Gustavsson and S. Gustafsson, “On the use of transient plane source sensors for studying materials with direction dependent properties,” in Thermal Conductivity 26: Thermal Expansion 14: Joint Conferences (Cambridge Massachusetts, USA, 2001) p. 367.
40 ISO 22007-7:2023, Plastics — Determination of thermal conductivity and thermal diffusivity — Part 7: Transient measurement of thermal effusivity using a plane heat source.
41 Gustavsson, M., Saxena, N.S., Karawacki, E, and Gustafsson, S.E., Specific heat measurements with the Hot Disk thermal constants analyser. Thermal Conductivity 23, 56-65 (1996).
42 Phase transformations in Metals and Alloys D.A. Porter, K.E. Easterling, p.1
43 O. Guillon, J. Gonzalez-Julian, B. Dargatz, T. Kessel, G. Schierning, J. Räthel and M. Herrmann, *Advanced Engineering Materials*, 2014, 16 (7), 830-849.
44 Z. A. Munir, U. Anselmi-Tamburini, and M. Ohyanagi, *J. Mater. Sci.*, 2006, 41, 763.
45 Z. A. Munir, D. V. Quach, M. Ohyanagi, *J. Am. Ceram. Soc.*, 2011, 94, 1.
46 J. E. Garay, *Annu. Rev. Mater. Res.*, 2010, 40, 445.
47 M. Tokita, Handbook of Advanced Ceramics, 2013, Chapter 11.2.3. Spark Plasma Sintering, 10.
48 L. E. Smart, Solid State Chemistry: an Introduction, 4th ed., 2012.
49 R. Guinebretière, X-Ray Diffraction by Polycrystalline Materials (ISTE, London, 2007).
50 G. Will, Powder diffraction: The Rietveld Method and the Two-Stage Method (Springer-Verlag Berlin Heidelberg, Berlin, Heidelberg, 2006).
51 R. A. Young (ed.), The Rietveld Method. International Union of Crystallography, Oxford University Press, 1993, p. 298.
52 G. Skomedal, A. Burkov, A. Samunin, R. Haugsrud, and H. Middleton, *Corros. Sci.*, 2016, 111, 325.
53 Liu, W.; Tang, X.; Li, H.; Yin, K.; Sharp, J.; Zhou, X.; Uher, C. Enhanced Thermoelectric Properties of n-type $Mg_{2.16}(Si_{0.4}Sn_{0.6})_{1-y}Sb_y$ due to Nano-Sized Sn-rich Precipitates and an Optimized Electron Concentration. J. Mater. Chem. 2012, 22, 13653–13661, DOI: 10.1039/c2jm31919e
54 Liu, W.; Zhang, Q.; Yin, K.; Chi, H.; Zhou, X.; Tang, X.; Uher, C. High Figure of Merit and Thermoelectric Properties of Bi-Doped $Mg_2Si_{0.4}Sn_{0.6}$ Solid Solutions. J. Solid State Chem. 2013, 203, 333–339, DOI: 10.1016/j.jssc.2013.04.041
55 Farahi, N.; Prabhudev, S.; Botton, G. A.; Salvador, J. R.; Kleinke, H. Nano- and Microstructure Engineering: An Effective Method for Creating High Efficiency Magnesium Silicide Based Thermoelectrics. *ACS Appl. Mater. Interfaces* 2016, 8, 34431–34437, DOI: 10.10.21/acsami.6b12297

56 Johannes de Boor, Titas Dasgupta, Hendrik Kolb, Camille Compere, Klemens Kelm, Echard Mueller, Microstructural effects on thermoelectric efficiency: A case study on magnesium silicide, *Acta Materialia*, Volume 77, 2014, Pages 68-75, ISSN 1359-6454, https://doi.org/10.1016/j.actamat.2014.05.041.
57 L. Vegard, *Zeitschrift für Physik.*, 1921, 5 (1), 17–26.
58 T. Dasgupta et al., Influence of power factor enhancement on the thermoelectric figure of merit in $Mg_2Si_{0.4}Sn_{0.6}$ based materials, *Phys. Status Solidi A*, 2014, 211, 1250—1254
59 Polymeris G S, Vlachos N, Symeou E, Kyratsi T. Thermoelectric Properties of Bi-Doped $Mg_2Si_{0.6}Sn_{0.4}$ Solid Solutions Synthesized by Two-Step Low Temperature Reaction Combined with Hot Pressing. Physica status solidi (a). 2018 Sep; 215(17):1800136.
60 K. Valset, E. Flage-Larsen, P. Stadelmann, and J. Taftø, *Acta Mater.*, 2012, 60, 972-976.
61 O. Madelung, U. Rössler, M. Schulz, Non-Tetrahedrally Bonded Elements and Binary Compounds I, Landolt-Börnstein - Group III Condensed Matter, volume 41C, Springer-Verlag Berlin Heidelberg © 1998.
62 Andersen, H. L.; Zhang, J.; Yin, H.; Iversen, B. B. Structural Stability and Thermoelectric Properties of Cation- and Anion-Doped $Mg_2Si_{0.4}Sn_{0.6}$. *Inorg. Chem. Front.* 2017, *4*, 456– 467, DOI: 10.1039/C6QI00520A
63 Goyal, G.K., Dasgupta, T. Effect of Magnesium Content and Processing Conditions on Phase Formation and Stability in $Mg_{2+\delta}Si_{0.3}Sn_{0.7}$. *J. Electron. Mater.* 47, 2066–2072 (2018). https://doi.org/10.1007/s11664-017-6012-9
64 Large Scale Solid State Synthetic Technique for High Performance Thermoelectric Materials: Magnesium-Silicide-Stannide, Daniel C. Ramirez, Leilane R. Macario, Xiaoyu Cheng, Michael Cino, Daniel Walsh, Yu-Chih Tseng, and Holger Kleinke, ACS *Applied Energy Materials* 2020 3 (3), 2130-2136, DOI: 10.1021/acsaem.9b02146
65 Yi, S. I.; Attari, V.; Jeong, M.; Jian, J.; Xue, S. C.; Wang, H. Y.; Arroyave, R.; Yu, C. Strain-induced suppression of the miscibility gap in nanostructured Mg_2Si-Mg_2Sn solid solutions. *J. Mater. Chem. A* 2018, *6*(36), 17559 – 17570, DOI: 10.1039/C8TA05798B
66 R. Orenstein, J. P. Male, M. Toriyama, S. Anand and G. J. Snyder, Using phase boundary mapping to resolve discrepancies in the Mg_2Si–Mg_2Sn miscibility gap, *J. Mater. Chem. A*, 2021, 9, 7208—7215
67 Control of Mg content and carrier concentration via post annealing under different Mg partial pressures for Sb-doped Mg_2Si thermoelectric material, Daisuke Kato, Kouta Iwasaki, Masahito Yoshino, Tomoaki Yamada, Takanori Nagasaki.

68 G.S. Polymeris, N. Vlachos, A.U. Khan, E. Hatzikraniotis, Ch.B. Lioutas, A. Delimitis, E. Pavlidou, K.M. Paraskevopoulos, Th. Kyratsi, Nanostructure and doping stimulated phase separation in high-ZT $Mg_2Si_{0.55}Sn_{0.4}Ge_{0.05}$ compounds, *Acta Materialia*, Volume 83, 2015, Pages 285-293, ISSN 1359–6454, https://doi.org/10.1016/j.actamat.2014.09.031
69 Porter, D. A.; Easterling, K. E.; Sherif, M. Y. Phase Transformations in Metals and Alloys, 3rd ed.; CRC Press: Boca Raton, FL, 2009, pp. 288–297
70 Lorimer, G., Precipitation Prosses in Solids, K.C. Russel and H.I. Aaronson (Eds.), The Metallurgical Society of AMIE, 1978, p.87.
71 Baur, R; Gerold, V., Zeitschrift fur Metallkunde 52 (1961) 671.
72 Hall, E. H., "On a new action of the magnet on electric currents", American Journal of Mathematics, 2, No. 3, pages 287–292 (1879).
73 G.J. Snyder, A.H. Snyder, M. Wood, R. Gurunathan, B.H. Snyder, C.N. Niu, Weighted mobility, *Adv. Mater.*, 32 (2020), Article 2001537, https://doi.org/10.1002/adma.202001537
74 Zhang Y, Brorsson J, Qiu R and Palmqvist A E C, 2021 Enhanced thermoelectric performance of Ba8Ga16Ge30 clathrate by modulation doping and improved carrier mobility *Adv. Electron. Mater.* 7 2000782
75 SANTOS, Rafael, AMINORROAYA YAMINI, Sima and DOU, Shi Xue (2018). Recent progress in magnesium-based thermoelectric materials. *Journal of Materials Chemistry A*, 6 (8), 3328-3341, https://doi.org/10.1039/C7TA10415D
76 Thermoelectric Properties of Bi-Doped Magnesium Silicide Stannides, Leilane R. Macario, Xiaoyu Cheng, Daniel Ramirez, Takao Mori, and Holger Kleinke, *ACS Applied Materials & Interfaces,* 2018 10 (47), 40585-40591, DOI: 10.1021/acsami.8b15111
77 Highly effective $Mg_2Si_{1-x}Sn_x$ thermoelectrics V. K. Zaitsev, M. I. Fedorov, E. A. Gurieva, I. S. Eremin, P. P. Konstantinov, A. Yu. Samunin, and M. V. Vedernikov, *Physical Review B*, 74, 045207 2006,
78 M. Gustavsson, and S. E. Gustafsson, proceedings of the joint conference Thermal Conductivity 26: Thermal Expansion 14, 2001 (Cambridge, Massachusetts, USA), p. 367
79 M. Gustavsson, and S. E. Gustafsson, *Thermochimica Acta*, 2006, 442, 1.
80 K. Hanstorp, B.M. Mihiretie, M. Karlsteen, A. Rosén, M. Sundin1, D. Cederkrantz, H. Otterberg, Å. Hinton and B. Berg, Numerical Simulation and Experimental Scheme for Monitoring Hoof Wall Structure and Health in Sport Horses, proceedings of the *4th International Congress on Sport Sciences Research and Technology Support*, 171-175 (2016).